SHOCKED MOLECULAR GAS IN THREE SUPERNOVA REMNANTS: W28, W44, 3C391

by

Andreea Font

Submitted in partial fulfillment of the

requirements for the degree of

Master of Science in Astronomy

Department of Astronomy and Physics

Saint Mary's University

Halifax, Nova Scotia

B3H 3C3

Acknowledgements

This research has made use of data obtained from the Canada-France-Hawaii Telescope, which is operated by the NRC of Canada, the CNRS of France, and the University of Hawaii. I would like to thank George Mitchell for his guidance in this project and for giving me the opportunity to participate on an observing run in Hawaii. Also, many thanks to Jean-Pierre Maillard for his help in reducing the near-infrared data and for providing the BEAR software. I am very grateful to the members of the defence committee; David Clarke, Gary Welch, and the external referee, Dale Frail, for very useful suggestion which have improved the outcome of this thesis.

I am especially grateful to Michael West for his permanent enthusiasm and for initiating my interest in cosmology and to Malcolm Butler for sharing with us his clever insight. Many thanks to David Clarke, David Guenther, and Gary Welch for their support and many interesting discussions. I have benefited from useful discussions with Nick Tothill over several aspects of ISM. I wish to thank my fellow colleagues; Rene Tanaja, Kevin Douglas, Juan Ramon Sanchez Velar, Ian McCarthy, Sandro Mendes, and Tricia Close for all their help and for the beautiful memories we share together.

Hamlet: *Do you see yonder cloud that's almost in shape of a camel?*

Polonius: *By th'mass, and 'tis like a camel, indeed.*

Hamlet: *Methinks it is like a weasel.*

Polonius: *It is backed like a weasel.*

Hamlet: *Or like a whale?*

Polonius: *Very like a whale.*

(**Hamlet** . III.2)

Abstract

The three supernova remnants, 3C391, W28 and W44, are known to be interacting with their environmental molecular clouds. Our goal in studying such interactions is to determine whether compression by supernova shocks triggers star formation or whether, on the contrary, the shock destroys the clouds. Another interest in pursuing this research is to distinguish the physical nature of the shocks which occur in these supernova remnants, i.e. either J or C-type shocks.

Observations have been made in both millimeter and near-infrared domains. Molecular observations, which trace the quiescent gas, include the rotational transitions ^{12}CO J=3 $\rightarrow$ 2 and ^{13}CO J=3 $\rightarrow$ 2, and several other molecules in the 218-363 GHz range. For studying the shocked gas, we made use of v=1-0 S(1) H_2 as well as Brγ emission observations on several locations close to the shock front.

We are investigating in detail the morphology of the gas near (1720MHz) OH maser locations, which are known to be sites of shocked gas. The analysis consists also of the estimation of the excitation temperatures and column densities of clumps of gas and the determination of their gravitational stability, in order to test the triggering of star formation hypothesis.

The high resolution, both spatial (0.5″) and in velocity ($\sim$ 12 km/s) of the BEAR instrument on CFHT gives for the first time the possibility to resolve the vibrational line H_2 v=1-0 S(1) in the three remnants. This provides additional information about the local speed of the shocks and their possible physical nature. Also, the absence of Brγ emission puts further constraints on the nature of the shock. We analyse the line intensities of the H_2 v=1-0 S(1) and the upper limit values for Brγ emission and compare the results with the available theoretical models of shocks. Our study supports the hypothesis of a C-type shock, in agreement with the theoretical picture of the (1720 MHz) OH maser originating conditions.

Contents

List of Tables

List of Figures

Chapter 1

Theoretical Framework

1.1 Introduction

All three systems investigated in this study, 3C391, W28 and W44, are believed to be cases of supernova remnant/ molecular cloud (SN/MC) interaction. The association of supernova remnants with molecular clouds has been suggested, based on their observed positional coincidence, for many different cases (Huang and Thaddeus, 1985, 1986). In principle, we would expect those kind of associations to occur frequently in nature, since massive stars, which will end their lives in a supernova explosion, will tend to do so in the proximity of their parental molecular clouds, as suggested also by the close correspondence of OB associations and H II regions in spiral arms (Elmegreen & Lada, 1977). However, only few cases of SN/MC interaction are firmly proved to date.

In several cases, there is convincing evidence of supernova remnants/ molecular

clouds interaction, most of it having been brought about by molecular mapping results. Among the most studied examples of such interactions are: W44, W28, Puppis A, G84.2-0.8, CTB 109 [G109.1-1.0], HB 21, and the favorite target of such studies, the IC443 supernova remnant (Wilner *et al.*, 1998 and the references therein). The signature of shock propagation is often seen by the broadening of molecular emission lines and a maximum of their brightness at the interface between the remnant and the cloud (e.g Wootten, 1977, for CO mapping).

Another approach in studying supernova shocks is by observing directly the hot, shocked gas, seen in the near-infrared domain, mostly from the vibrational transitions of molecular hydrogen. Molecular hydrogen emission provides the primary coolant for interstellar shock waves, produced when molecular clouds collide, or when stellar winds, H II regions, and supernovae encounter molecular clouds. The last process, which is also the one we are interested in, may be responsible for triggering star formation when the compressed gas behind the shock wave collapses (Elmegreeen and Lada, 1977). One principal interest in studying the SN-MC associations is the underlying belief that they can be sites of triggered star formation.

1.2 Star Formation Induced by Shocks

It is customary by now to classify star forming processes broadly into two categories:

i) "Spontaneous" gravitational collapse of a molecular cloud (or a part of it), driven by the loss of internal energy, which originally could have been thermal, magnetic or turbulent. This leak of energy could proceed through radiation, magnetic diffusion or turbulent viscosity. Molecular or grain molecular reactions can also be a

source of spontaneous collapse, if they can change the gas temperature and therefore, alter the balance between heating and cooling in the cloud.

ii) Another way in which star formation is believed to take place is through the so-called "stimulated" collapse. This may occur if some external process can act on the cloud and set it into a state of gravitational instability. The shocks from supernova explosions could then be an attractive candidate for triggering star formation. Moreover, the shocks may also clear away the material around the old stars and direct it towards other locations where, under favorable conditions, it could form new stars (Elmegreen, 1977).

Of course, there should be specific conditions in place for a shock to result in star formation. One basic requirement is that the cloud be massive enough so that a sufficient amount of gas could be compressed in order to form stars. Another requirement is that the physical conditions in the post-shocked material, which are favorable for collapse, must exist long enough, possibly as long as the free-falling time to form a star. If τ is the characteristic time-scale for the shock (i.e. the time during which post-shocked material could have collapsed), its value for supernova shocks is $\tau \sim 10^5$ years. This means that probably only low-mass self-gravitating fragments have time to form in supernova remnants, in contrast with H II regions, for example (for which $\tau \sim 10^6$ years), where then both low and high-mass fragments can form. Of the same importance as the previous two requirements is the orientation of the magnetic field, depending on which the gaseous compression can be enhanced (in the part of the shock perpendicular to $\vec{B}$) or inhibited (in the part of the shock parallel to $\vec{B}$).

1.3 Shocks in Supernova Remnants.

Shock Models. C ("continuous") versus J ("jump") shocks.

The structure of shock waves in molecular clouds is determined by the coupling between the magnetic field and the weakly ionized pre-shock gas. For shock speeds below 40 - 50 km s^{-1} (McKee, Chernoff & Hollenbach, 1984), Lorentz forces within the shock front push the charged particles away through the neutrals, and the resulting collisions accelerate, compress and heat the gas. This process is slow, because the charged particles are rare, so the gas is able to radiate away a significant fraction of the heat while still within the shock front, primarily through the emission of radiation in molecular rotational and vibrational transitions. Shocks of this kind are denoted C-type (Draine, 1980), where the "C" connotes a rather "continuous" variation of the fluid variables across the shock. At higher shock speeds, the molecular coolants are dissociated, cooling can no longer keep pace with the heating, and the gas pressure becomes dynamically significant. A thin, viscous sub-shock forms within the front, and the shock is termed J-type (Draine, 1980), where the "J" connotes a sudden "jump" of the fluid variables across the shock.

For a C-type shock, the cooling length in the shocked gas is short compared to the ion-neutral coupling length. C-type shocks are characterized by fluid velocities which vary smoothly over a length scale larger than the cooling length, in contrast to "jump-" or "J-type" shocks where bulk kinetic energy is converted to random thermal energy within a thin adiabatic layer (Kaufman & Neufeld, 1996a).

In general, the cooling process can proceed through: radiative cooling from rotational and ro-vibrational emissions of H_2O, H_2 and CO; gas-grain cooling resulting from collisions between hot gas molecules and other cooler grains; and dissociative

cooling associated with the destruction of H_2. Depending on temperature, each species has its own cooling efficiency. OI, CO and H_2O can be important high-density coolants for temperatures below 1000 K. At higher temperatures, cooling through collisional excitation and radiative decay of vibrational states of H_2 play the dominant role.

1.4 Shocked H_2

Cooling Through Infrared v=1-0 S(1) Emission of H_2.

In general, in interstellar clouds the temperatures are too low to produce significant column densities of molecules in any but the lowest rotational states. In regions behind strong shock waves, however, a substantial fraction of the molecules may become excited into vibrational or high rotational states. Thus, for kinetic temperatures of several thousands Kelvin, as is the case in shocked regions, vibrational states of H_2 can be collisionally excited.

At kinetic temperatures of $T_{kin} \sim 2000$ K, the relative level populations of hydrogen molecules are approximately in thermal equilibrium. The intensity of an optically thin line of H_2, taking into account the dust absorption effects, can be written as:

$$I_{ij} = \frac{1}{4\pi} A_{ij} E_{ij} N_i e^{-\tau} (\mathrm{ergs^{-1}cm^{-2}sr^{-1}}), \tag{1.1}$$

where A_{ij} is the spontaneous emission rate (s^{-1}), E_{ij} is the transition energy between i and j levels, N_i is the column density (cm^{-2}) of molecules in state i , and τ is the dust optical depth at energy E_{ij}. The dust opacity depends on the column density of intervening dust and several estimates of its value are in the range of $\tau \sim 2$-4

(Shull & Beckwith, 1982 and the references therein). The Einstein coefficient A for radiative de-excitation for v=1-0 S(1) at 2.12 μm is 3.47 (Smith and Mac Low, 1997).

Assuming the molecules to be at the post-shock temperature, the intensity is given by

$$I_{ij} \approx \frac{\mu n_0 V_s^3}{4\pi\gamma_{ij}} \frac{2\gamma}{(\gamma+1)^2}, \tag{1.2}$$

where μ is the mean molecular weight of the post-shock gas (2.33 m_H including 10% He), γ is the adiabatic index (assumed to be 9/7 for three transitional, one vibrational and two rotational modes), γ_{ij} represents the ratio of the total cooling rate to the rate in the line *(ij)*, n_0 is the pre-shock density and V_s is the shock speed (Shull & Beckwith (1982). Thus, the intensity of the H_2 infrared line can determine the product $n_0 V_s^3$, and so, provided that n_0 is known, one can in principle deduce the nature of the shock.

1.5 Shock Chemistry

H_2 is one of the principal coolants within the shock fronts. In certain conditions H_2O can also be an important coolant.

Water formation is very efficient for high density shocks, $n_0 \sim 10^8$ cm^{-3} (Kaufmann and Neufeld, 1996b), once the shock temperature exceeds 400 K, i.e. for shock velocities $\geq$ 10 km s^{-1}. Above this temperature, nearly all the pre-shock oxygen not bound in CO is rapidly incorporated in H_2O, producing large column density of water ($\sim 10^{18}$ cm^{-2}). Once the water is formed, it dominates the cooling throughout the shock-heated region. The efficiency of H_2 cooling is greatly reduced at high

densities by collisional de-excitation, and it is only the high efficiency of non-LTE H_2O cooling that allows the shocked gas to stay cool enough for molecules to survive.

Since the H_2 and H_2O are the principal coolants in the shocked regions, it is reasonable to limit the chemical chain of reactions only to these species. The other molecules have relative abundances to H_2, less than 10^{-4}, so they cannot in principle, affect significantly the final chemical composition of the gas.

One important goal of the shock chemistry is to understand the formation of (1720 MHz) OH masers, since they are not an immediate consequence of the chemical reactions. In J-type shocks, molecules are destroyed within the shock front and recombine behind the shock. In non-dissociative C-shocks (with shock speed exceeding 10 km s^{-1}), OH is only an intermediate in the chain of reactions, because of its rapid conversion to H_2O within the shock front (Kaufman & Neufeld, 1996a):

$$H_2 + O \rightarrow OH + H \tag{1.3}$$

$$H_2 + OH \rightarrow H_2O + H \tag{1.4}$$

The first reaction is endothermic and it occurs only after the temperature exceeds 400 K. As a result, the atomic oxygen is efficiently converted into OH, which is in turn, converted by a less endothermic reaction to water.

At the same time, OH can be produced and destroyed by the following reactions:

$$H_2O + O \rightarrow OH + OH \tag{1.5}$$

$$OH + O \rightarrow O_2 + H \tag{1.6}$$

(Wagner & Graff, 1987)

Thus shock chemistry in itself does not produce a significant amount of OH, and the temperature at which OH exists ($\sim$ 400 K) is too high to explain the origin of (1720 MHz) OH masers.

1.6 Modeling shocks

In modeling the impact of supernova shocks on molecular clouds, a range of factors needs to be taken into account, such as the shock chemistry reactions, shock speed v_s, the cloud mass, the cooling rate and the magnetic field strength.

Different shock models have been invoked to date in order to explain all the infrared emission lines or the species abundances. However, at present, there is no single model able to explain all the observational data. Fast, dissociative J shocks can provide strong Brγ emission, but weak H_2. Slow, partially dissociative J-shocks yield strong H_2 emission, but weak [OI] (because of the chemical conversion of atomic oxygen into H_2O at high temperature). Fast C-type shocks have also strong H_2 emission, but the [OI] emission is weak (because of the chemical destruction of [OI]). Finally, slow non-dissociative C-type shocks do not reach high enough temperatures to excite H_2.

For pre-shock densities of $n_H \geq 10^5$ cm^{-3} and magnetic fields of B $\sim$ 1mG, Wardle (1998) studied the role of dust grains in determining the structure of steady, cold, oblique C-type shocks. The result of simulations shows that the grains are partially decoupled from the magnetic field and the shock structure is significantly thinner than in models which don't take into account the grain-neutral drift.

Smith and Mac Low (1997) have modeled the time-dependent evolution of the

molecular hydrogen emission lines in the infrared. Their results show that if the initial shock is fast, the molecules do not survive, and the emission is very weak. As the ionized precursor develops, the line intensity rises rapidly. As the strength of the shock decreases, molecules can survive and emit with the high excitation characteristic of the jump shock. Later, the jump condition is too weak to excite H_2 and a C-shock forms.

The role of magnetic fields in the development of the interaction.

Numerical simulations carried out without magnetic fields suggest that hydrodynamical instabilities destroy the molecular clouds (Klein, McKee and Colella, 1994). However, the instabilities can be damped once the magnetic fields are included in the models, hence limiting the fragmentation of the cloud and allowing it to survive as a coherent structure (Mac Low *et al.*, 1994).

Cosmic Rays.

Finally, cosmic rays are another ingredient which need to be added to shock models. The thermal radiation from the remnant interior (mainly X-rays), cosmic rays and their secondary gamma rays, and direct impact of the blast wave onto the clumps should visibly perturb the excitation, chemistry and dynamics of the parent molecular cloud for at least the $\sim 10^5$ yr during which the SN blast wave is the most powerful.

The cosmic rays can be generated by multiple reflections of high-energy charged particles within the magnetic field of a SN/MC interaction. Once generated, the cosmic rays can easily permeate the entire region (Chevalier, 1977; Esposito *et al.*, 1996).

It is known that cosmic rays play an important role, by acting as a heating source

for the cloud. If, by some process, the cosmic rays can be removed, the heating of the cloud would be significantly diminished and the internal balance between heating and cooling altered. This could lead to the collapse of the cloud and possibly star formation.

1.7 Examples of SNR/MC interaction. C or J type shocks?

In the case of the IC443 supernova remnant, a combination of J- and C-type shocks with different velocities and pre-shock densities have been invoked to account for the observed line fluxes (Burton *et al.* 1990). A distribution of low-velocity C-shocks may explain the [OI] 63 μm line emission and a distribution of high-velocity C-shocks may explain the H_2 v=1-0 S(1) line. However, this model does not explain the constancy of [0I 63 μm]/[H_2 v=1-0 S(1)] and [H_2 v=1-0 S(1)]/[H_2 v=2-1 S(1)] line ratios in the same field, unless an assumption of constant distribution of shock velocities in the beam is made. Another model, of a partially dissociative J-shock, can also explain the emission lines. But in that case another ad-hoc assumption must be made: that the oxygen chemistry is suppressed, so that H_2O and OH are not formed behind the shock. O'Brien and Drury (1996) argued however that the constancy of line ratios could be explained if the assumption of LTE is abandoned and non-thermal processes are incorporated into magnetized C-shock models.

Present theoretical models of maser emission (Lockett *et al.*, 1999; Wardle *et al.*, 1998) favor the C-type shocks occurring at the site of SN/MC interaction. J-type shocks have been lately ruled out, because they cannot produce the high column

densities necessary for observable maser emission ($N_{H_2} \sim 10^{21}$ cm^{-2}) and the low thermal pressures required by the pumping of the (1720 MHz) OH maser (Lockett *et al.*, 1999). Only C-type shocks seem capable of meeting all the requirements, but even so they cannot generate the optimal conditions for the (1720 MHz) OH maser production. However, this is consistent with the low detection rate of (1720 MHz) OH emission found by Green *et al.* (1997) in SNRs (17 detections in a sample of 160 SNRs, hence $\sim$ 10%).

Other observational supporting evidence for the C-shock hypothesis comes from the detection of high maser polarization in several supernova remnants (Claussen *et al.*, 1997) and the magnetic fields that this implies (B $\sim$ few mG). Numerical simulations showed that J-shocks cannot produce the observed magnetic field strengths. C-shocks are able to create the necessary magnetic field strengths and additionally, can generate magnetic field gradients by shock compression (Lockett *et al.*, 1999). The field curvature created when a maser is located near the edge of an expanding SNR can also create additional magnetic field gradients. The heat efficiency is increased through the ambipolar diffusion process, and so high column densities of H_2 are produced, as required by C-shock models.

Recent observational studies in 3C391, W28 and W44 supernova remnants (Reach and Rho, 1998; Frail and Mitchell, 1998) have found for the ambient gas, temperatures (50–125 K) and densities (n = 10^5 - 10^6 cm^{-3}), in the range predicted by Lockett *et al.* (1999). Frail and Mitchell (1998) suggest that either a partially dissociative J-type shock or a C-shock can explain the determined physical conditions.

Results from studies of infrared emission lines of H_2O and OH in 3C391 (Reach and Rho, 1998, 1999) seem to favor C-type shock models. The same authors found

new evidence for C-shocks from studies of CO line brightness (and other molecules) in the 3C391 maser region (denoted by them as 3C391:mol). The constraints of $10^4 < n_0 < 10^5$ cm^{-3} and $10 < v_s < 50$ km s^{-1} imply the presence of a C-type shock (Reach and Rho, 1998, 1999).

1.8 Motivation for the Present Study

This present study is a combined analysis, performed in both millimeter and near-infrared domains, of three supernova remnants: W28, W44 and 3C391. Frail and Mitchell (1998) have previously shown several spatial coincidences of molecular peaks with the location of (1720 MHz) OH masers towards several regions within these three supernova remnants. The emission lines are broad, which is a clear sign of the shock passage. Motivated by this result, we determine here the physical properties of the gas near the location of these masers in the post-shock regions and study if there is any potential for shocks to trigger star formation or whether, on the contrary, the shocks fragment or destroy the cloud.

The near-infrared observations covered small fields within the CO mapped regions. Our motivation in performing the near-infrared observations (vibrationally excited H_2 emission at 2.12 μm, and Brackett γ emission at 2.16 μm) was to trace the location of hot ($T_{kin} \sim 2000$ K), shocked gas, and to identify the physical nature of the shocks (shock velocity, J- or C-type of shock, *etc.*) occurring in these supernova remnants.

Chapter 2

Observations

2.1 ^{12}CO J=3 → 2 and ^{13}CO J=3 → 2 Observations

The ^{12}CO J=3 → 2 and ^{13}CO J=3 → 2 observations were made by George F. Mitchell and Dale A. Frail.in 1997 over 4 nights in July 1997 and 2 nights in March 1998 using the 15-m James Clerk Maxwell Telescope (JCMT). The technique used was raster scanning, in which the off-source position is observed at the end of each scan row. The observations required the use of the common user B-band receiver, with a beam-width of 13″ and a main beam efficiency of 0.79 (Frail and Mitchell, 1998).

Six maps for ^{12}CO J=3 → 2 transition have been made around different (1720 MHz) OH maser sites, towards the three supernova remnants: W28E, W28F, W44E, W44F and 3C391:mol. The notations for the above regions are the same as those from

Claussen *et al.* (1997) and Reach and Rho (1996). Table 2.1 contains information regarding the offset extension of the ^{12}CO J=3 → 2 emission maps, the systemic velocity of each supernova remnant, and the time of observation.

Table 2.1: Telescope pointing parameters for ^{12}CO J=3 → 2 mapping.

Name	α(1950) (h m s)	δ(1950) (° ′ ″)	α Offsets (″ × ″) from: to:	δ Offsets (″ × ″) from: to:	V_{LSR} (km/s)	Obs. Time
W28F	17 58 49.18	-23 19 00.00	35.00 -35.00	55.00 -55.00	12.0	22/07/1997
W28E	17 58 48.78	-23 18 00.0	35.00 -35.00	35.00 -35.00	12.0	22/07/1997
3C391	18 46 47.68	-01 01 59.98	40.00 -40.00	40.00 -40.00	105.0	22/07/1997
W44E	18 53 56.98	01 25 45.00	35.00 -35.00	60.00 -60.00	45.0	22/07/1997
W44F	18 54 04.68	01 22 35.00	45.00 -25.00	20.00 -55.00	45.0	25/07/1997
W44F	18 54 04.66	01 22 35.00	155.00 -220.00	225.00 -350.00	45.0	26/03/1998

Also, three raster maps of ^{13}CO J=3 → 2 emission have been made, towards W28F, W44F and 3C391:mol regions within the targeted supernova remnants. The pointing parameters of the telescope are given in the Table 2.2.

Table 2.2: Telescope pointing parameters for ^{13}CO J=3 → 2 mapping.

Name	α(1950) (h m s)	δ(1950) (° ′ ″)	α Offsets (″ × ″) from: to:	δ Offsets (″ × ″) from: to:	V_{LSR} (km/s)	Obs. Time
W28F	17 58 49.18	-23 19 00.0	35.00 -35.00	55.00 -55.00	12.0	23/07/1997
3C391	18 46 47.68	-01 01 00.00	35.00 -35.00	45.00 -45.00	105.0	23/07/1997
W44F	18 54 04.66	01 22 35.00	30.00 -50.00	75.00 -50.00	45.0	28/03/1998

2.2 Other Molecules -JCMT Observations

Observations were made in July 1997 and March 1998 by George F. Mitchell and Dale A. Frail, using A and B common user receivers at the JCMT. Several offsets were targeted within W28F, W44F and 3C391:mol regions in the three supernova remnants. Tables 2.3 - 2.5 show the molecular transitions the search was made for, the observed offsets with respect to the center of each region and the times of observation.

W28F region (centered on $\alpha(1950) = 17^h\ 58^m\ 49^s.18$, $\delta(1950) = -23°\ 19'\ 00''.0$).

Table 2.3: Observation parameters for other molecules -W28F region

Molecule	Frequency	Offsets			Time of Observation
	(GHz)	(-5″, 45″)	(15″, -40″)	(-10″, 15″)	
H_2CO	218.2 / 218.4	√	√	√	22/07/1997
CH_3OH	241.8		√		28/03/1998
SiO	347.3			√	22/07/1997
HCN	354.5	√	√	√	22/07/1997
			√		28/03/1998
HCO^+	356.7		√	√	22/07/1997
HNC	362.6		√		28/03/1998

W44F region (centered on $\alpha(1950) = 18^h\ 54^m\ 04^s.6$, $\delta(1950) = 01°\ 22'\ 35''$).

Table 2.4: Observation parameters for other molecules -W44F region

Molecule	Frequency (GHz)	Offset	Time of Observation
CH_3OH	241.8	(20″, -180″)	28/03/1998
HCN	354.5	(20″, -180″)	28/03/1998
HNC	362.6	(20″, -180″)	28/03/1998
		(20″, -180″)	28/03/1998

3C391 region (centered on $\alpha(1950) = 18^h\ 46^m\ 47^s.6$, $\delta(1950) = -01°\ 01'\ 00''$).

Table 2.5: Observation parameters for other molecules -3C391 region

Molecule	Frequency (GHz)	Offsets (-5″, 10″)	(25″, -25″)	Time of Observation
H_2CO	218.4	√		24/07/1997
		√		28/03/1998
CH_3OH	241.8	√		28/03/1998
CS	342.8	√	√	25/07/1997
HCN	354.5	√		22/07/1997
			√	25/07/1997
HCO^+	356.7	√	√	24/07/1997
HNC	362.6	√		28/03/1998

All JCMT data presented in this study have been analyzed with the SPECX program (R. Padman, 1992), a special software package designed for JCMT spectral data reduction.

2.3 Near Infrared Observations

Near Infrared observations were carried out in July 1998, with the BEAR instrument at Canada-France-Hawaii Telescope (CFHT) by George F. Mitchell, Jean-Pierre Maillard and Andreea Font. BEAR combines a Fourier Transform Spectrometer with an infrared Redeye camera to provide a "data cube" with high angular resolution (0.5 ″) and high velocity ($\sim$ 15 km s^{-1}) resolution.

The filters used during the observations are: the K′ filter, with a central wavelength λ_c = 2.12 μm and a bandwidth $\Delta\lambda$ = 0.34 μm, the narrow band H_2 1-0 S(1) filter, centered on λ_c = 2.125 μm and with a bandwidth of $\Delta\lambda$ = 0.024 μm and the Brackett γ filter, centered on λ_c = 2.16 μm and $\Delta\lambda$ = 0.06 μm. The peak transmissions are 95% for the K′ filter and 70% for the narrow band filter.

Several BEAR fields, of 23″ in diameter, have been selected for investigation within the previously CO mapped regions. A search for v=1-0 S(1) H_2 vibrational emission has been done for two fields in W28F region (denoted as 'W28F-1' and 'W28F-2'), two fields in W44F (denoted as 'W44F-1' and 'W44F-4') and one field in 3C391 (denoted as '3C391:mol'). All fields of observation extend 23 ″ in diameter. Details of the observations are given in Table 2.6.

We have detected only the v=1-0 S(1) emission line of H_2. See table C.2. from Appendix C for other transitions that lie within the observed spectral range.

The raw data cube collected with BEAR instrument on CFHT and presented in this study has been analyzed with the BEAR data reduction package, using a special program written in IDL (Interactive Data Language) by François Rigaud and Jean-Pierre Maillard. The observed fluxes required corrections for the heliocentric motion. The corresponding velocity corrections are: $v_{LSR} = v_{obs}$ - 0.96 km s^{-1} (for W28F-1

Table 2.6: Telescope pointing parameters for shocked H_2 and Brγ.

Name	α(1950) (h m s)	δ(1950) (^{o} $'$ $''$)	$\Delta\lambda$ (μm)	Transition of interest	Obs. Time
W28F-1	17 58 49.84	-23 19 25.0	2.090 - 2.147	H_2 v=1-0 S(1)	18/07/1998
W28F-2	17 58 48.52	-23 18 40.0	2.090 - 2.147	H_2 v=1-0 S(1)	19/07/1998
3C391	18 46 47.4	-01 00 50.0	2.090 - 2.147	H_2 v=1-0 S(1)	14/07/1998
3C391	18 46 47.4	-01 01 50.0	2.142 - 2.202	Brγ	16/07/1998
W44F-1	18 54 05.7	01 21 50.0	1.989 - 2.320 (K$\prime$ filter)	H_2 v=1-0 S(1) and Br_γ	13/07/1998
W44F-4	18 54 06.40	01 19 29.0	2.090 - 2.147	H_2 v=1-0 S(1)	20/07/1998

region): $v_{LSR} = v_{obs}$ - 1.42 km s^{-1} (for W28F-2 region); $v_{LSR} = v_{obs}$ + 14.48 km s^{-1} (for W44F-1 region); $v_{LSR} = v_{obs}$ +12.51 km s^{-1} (for 3C391:mol region) (Jean Pierre Maillard, private communication). For the flux calibration procedure, we have divided the source signal by the signal from a standard star, which has a flux: $F_{star}(2.12\mu m) = 1.43 \times 10^{-3} \times F_{Vega}(2.12\mu m)$, where $F_{Vega}(2.12\mu m) = 4.52 \times 10^{-14}$ W cm^{-2} μ m^{-1}.

Chapter 3

The W28 Supernova Remnant

3.1 W28. Introduction

W28 supernova remnant (known also as G6.4-0.1 or G6.6-0.2) is located in the Galactic plane, at $\alpha(1950) = 17^h\ 57^m\ 30^s$, $\delta(1950)$ = -23° 25′ 00″ and extends $\sim$ 42 (arcmin) in angular size.

The distance to the remnant has been estimated by various authors. Using as a distance indicator the relationship between the radio surface brightness and linear diameter of a supernova remnant (Σ - D relation), Goudis (1976) obtains a distance of 1.8 kpc, Clark & Caswell (1976) 2.3 kpc and Milne (1979) 2.4 kpc. Kinematically, a distance of between 2.5 and 4.2 kpc has been obtained by Lozinskaya (1974), through HI absorption measurements. If the distance is near the lower limit, the remnant is most likely associated with the molecular clouds and H II regions in the area (Hartl *et al.* 1983).

An association between W28 and the pulsar PSR B1758-23 ($\alpha(1950) = 17^h\ 58^m\ 17.6^s$, $\delta(1950)$ = -23° 06′ 06″) remains uncertain. The two objects have a close location in sky coordinates and similar ages. However, the extremely large dispersion measure of the pulsar of 1074 ±6 $cm^{-3}pc$, determined by Kaspi *et al.* (1993), implies that it has a distance of 13.5 kpc, placing it well behind the supernova shell. Still, the pulsar's distance could be shorter if there is an intervening H II emission region which would help increasing the dispersion measure (Shull *et al.*, 1989). In support of this idea lies the evidence of a high density ambient medium for W28 remnant (Wooten 1981; Odenwald *et al.* 1984).

Observations in the optical domain are difficult since W28 is located in a heavily obscurated region of the Galactic plane. The optical emission fills most of the region delineated by the radio SNR and is seen to be filamentary in the NE but patchy in the rest of the remnant (Long *et al.*, 1991). The optical filament seen in Hα corresponds with the filament seen in the X-ray. From the optical spectra of the filaments, Lozinskaya (1974) was able to determine an expansion velocity of 45 ± 15 km s^{-1} (and from there, an age of about 6 × 10^4 yr). The numerous knots surrounded by diffuse emission do not support the standard Sedov expansion into a uniform medium, but rather suggest that the remnant encountered several cloudlets which have been subsequently evaporated.

In radio wavelengths, several non-thermal sources have been detected in a ring, with a flat spectrum core. The X-ray emission is centrally concentrated and is seen throughout the region outlined by the radio shell (Long *et al.*, 1991). Matsui and Long (1985) explored two possible mechanisms for the X-ray emission: the synchrotron emission due to an active central pulsar, and the thermal emission from

a thin hot plasma filling the interior of the remnant. By comparing W28 radio and X-ray emission with emission of known Crab-like remnants, the authors suggest that the first mechanism isn't very plausible. On the other hand, the X-ray morphology is similar to one predicted if the supernova exploded in a dense molecular cloud and then evolved rapidly to the radiative stage.

Molecular spectra and infrared observations (Wootten, 1981) reveal a warm dense core near a maximum of non-thermal radio emission of W28. Since no apparent infrared sources could be detected within the cloud, the ambient cloud is believed to be heated by the expanding supernova shock. Evidence for interaction of the supernova remnant with the adjacent molecular cloud comes from the distribution of the molecular material seen (in ^{12}CO and ^{13}CO 1→0 transition) following the eastern edge of the supernova shell (Wootten, 1981). The distribution of the CO gas peaks on the optical filaments. An OH cloud observed by Pastchenko and Slysh (1974) has a similar shape, but is displaced slightly north of the CO cloud, having its peak emission at the position of the W28 OH F maser (see Appendix B for maser identification).

An interesting study regarding the spatial relationship between the shocked and unshocked gas towards the northern part of W28 remnant was done by Arikawa *et al.* (1999). The region was mapped in both ^{12}CO J = 1→0 (which traces the cold, $\sim$ 10 K gas) and ^{12}CO J = 3→2 (which traces the warm, $\sim$ 30 K gas), showing the shocked gas having maximum line-widths of $\sim$ 70 km s^{-1} and the unshocked gas being displaced by 0.4 - 1.0 pc outward from the shocked gas. Moreover, all the OH masers are located at the boundary between the shocked and unshocked gas.

ISO observations have been performed by Reach and Rho (1998), using the Long

Wavelength Spectrometer (LWS) with a beam-size of 80″, reporting a detection of H_2O, OH and CO far-infrared emission in the region centered on an OH maser ($\alpha(1950) = 18^h\ 01^m\ 52^s.3$; $\delta(1950)$ = -23° 19′ 25″).

W28 is known to have numerous OH masers. Frail *et al.* (1994) detected 26 distinct (1720 MHz)OH masers along the interface between the SNR W28 and the adjacent molecular cloud. (1720 MHz)OH masers are known to trace the postshock gas, collisionally excited by H_2 molecules that have been heated by the shock. Theoretically modeling this maser emission, Elitzur (1976) determined the range in which the kinetic temperatures and densities must lie in order to create a strong inversion of the 1720 MHz line: 25 K $\leq T_k \leq$ 200 K and 10^3 cm^{-3} $\leq$ n $\leq$ 10^5 cm^{-3}, respectively. More recently, tighter constraints have been suggested by Lockett *et al* (1999): kinetic temperatures T_k between 50 – 150 K, relatively low molecular densities, n $\sim$ 10^5 cm^{-3} and OH column densities of the order of 10^{16} cm^{-2}.

A search for water masers at 22.235 GHz has been done in the same region by Claussen *et al.* (1999b), motivated by the fact that water masers are good tracers of star-forming regions (being created through shock excitation of ambient gas). However, it is known that different constraints for temperature and density are needed for strong water masers, T_k between 300 – 600 K and H_2 density of 10^9 cm^{-3} (Hollenbach 1997 and references therein). No water masers were found associated with the W28 remnant, in agreement with the temperature and denisty range implied by the presence of (1720 MHz)OH masers.

Measurements of magnetic fields in the maser regions give values of about $\sim$ 2 milliGauss. Thus, the magnetic pressure must be $\sim$ 100 times more than the thermal gas pressure (Claussen *et al.* 1999a), estimated from the hot X-ray interior of the

remnant. These large values of the magnetic field are similar with those predicted in modeling of C-type shocks (Lockett *et al.* 1999 and Draine *et al.* 1983).

3.2 W28 Observing Fields

This section summarizes the observational data present in this study for W28 (see also Chapter 2) and adds information about the location of the (1720 MHz)OH masers. in connection to our fields.

The Figure 3.1 displays the fields observed in this study comprising both W28E and W28F regions. The two CO maps were taken with JCMT, seen in figure as rectangles. W28E CO map is centered on $\alpha(1950) = 17^h\ 58^m\ 48^s.78$, $\delta(1950) = -23°\ 18'00''.00$, with a size of $70'' \times 70''$.

A ridge of (1720 MHz)OH masers, shown as small triangles, can be seen superimposed on the W28E CO map. This line of masers was revealed during the analysis as being in striking correspondence with the morphology of the CO gas. The maser identification has been done by using the interactive SIMBAD database (see appendix B for identification of their location). The virtual "SIMBAD field", shown in figure as a great circle, is centered on W28 33 OH maser ($\alpha(1950) = 17^h\ 58^m\ 49^s.17$; $\delta(1950) = -23°\ 18'\ 09''.6$) and extends a radius of 1 arcmin.

Although no near-IR observations have been done for the W28 E region, the W28E CO map (^{12}CO J=3 $\rightarrow$ 2) encompasses all of the (1720 MHz)OH masers. Coincident with a clump of CO at (-10", 0"), is the OH maser W28 30. Measurements of the line of sight magnetic field (Claussen *et al.*, 1997) give a value of 0.11 $\pm$ 0.03 mG. and therefore a total median magnetic field twice this value. B= 0.22 mG.

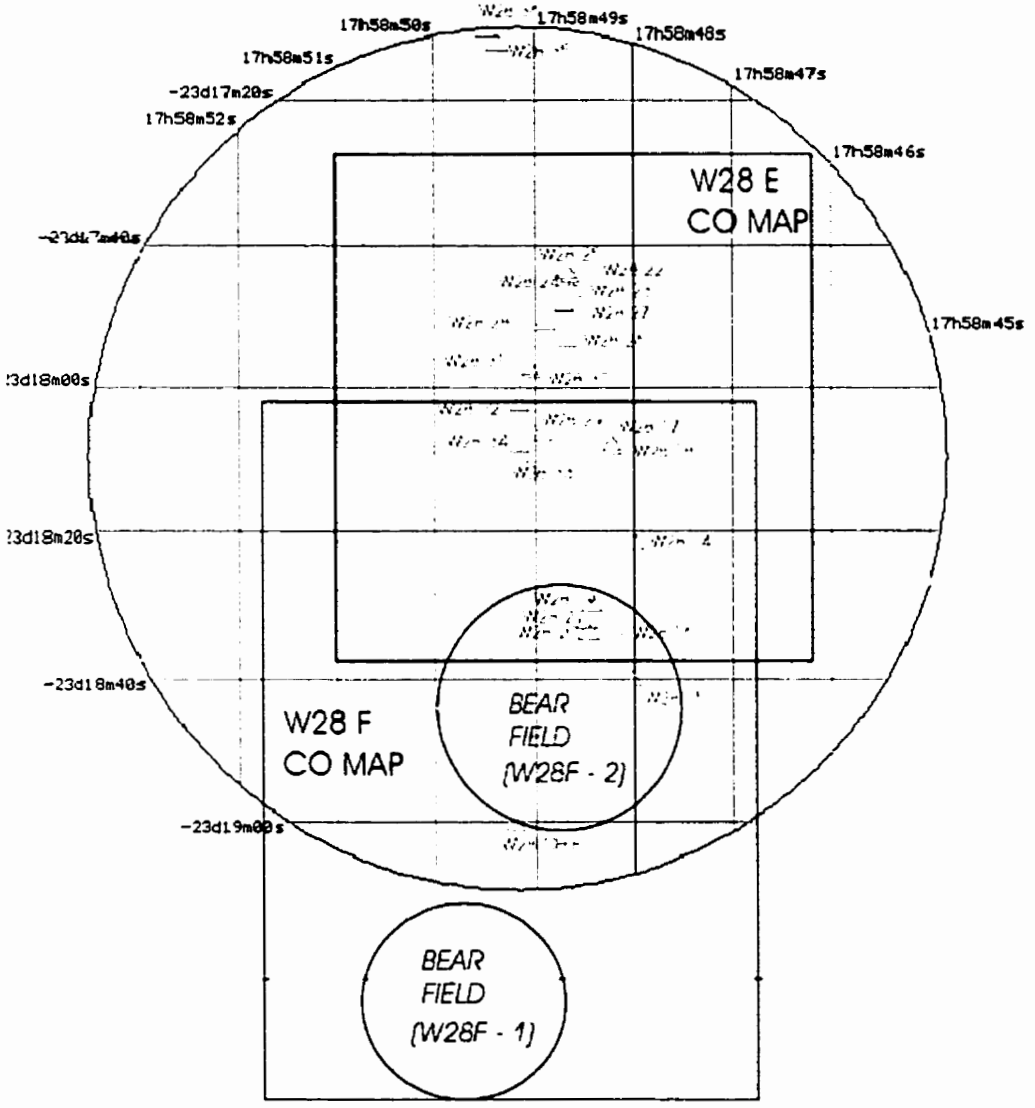

Figure 3.1: Observing fields in W28E and W28F regions.

W28F CO map is located to the south of W28E CO, being centered on $\alpha(1950)$ = 17^h 58^m $49^s.18$, $\delta(1950)$ = -23° 19′ 00″.00, and having a size of 70″ × 110″. A more detailed image of this region can be seen in Fig. 3.2. Superimposed on the W28F CO map, are the two near–IR fields (observed with the BEAR instrument on

CFHT) and shown as small circles with a diameter of 23″. The near-IR field denoted as "W28F-1" is centered on $\alpha(1950)=17^h\ 58^m\ 49^s.84$, $\delta(1950)$ = -23° 19′ 25″.0, and the "W28F-2" field is centered on $\alpha(1950)=17^h\ 58^m\ 48^s.52$, $\delta(1950)$ = -23° 18′ 40″.0. Both fields were chosen in regions with intense maser emission. Again, a ridge of masers can be seen in the W28F-1 field, and as will be seen later in section 3.4, it shows an interesting similarity with the near-IR emission of H_2.

The virtual "SIMBAD field" in Fig. 3.2 is centered on the maser W28 OH F ($\alpha(1950) = 17^h\ 58^m\ 49^s.2$, $\delta(1950)$ = -23° 19′ 00″) and has a radius of 1 arcmin. Details on the location of OH masers can be found in Appendix B).

Measurements of the magnetic fields are available for some of the OH masers from the W28E and W28F regions (Claussen *et al.* 1997): $\vec{B}_{los}$ = 0.11 ± 0.03 mG for **W28 34**, $\vec{B}_{los}$ = 0.11 ± 0.03 mG for **W28 30**, $\vec{B}_{los}$ = 0.10 ± 0.02 mG for **W28 31**, $\vec{B}_{los}$ = 0.45 ± 0.25 mG for **W28 27**, $\vec{B}_{los}$ = 0.18 ± 0.08 mG for **W28 23**, $\vec{B}_{los}$ = 0.25 ± 0.04 mG for **W28 21**, $\vec{B}_{los}$ = 0.31 ± 0.03 mG for **W28 24**, $\vec{B}_{los}$ = 0.34 ± 0.08 mG for **W28 16**, $\vec{B}_{los}$ = 0.09 ± 0.03 mG for **W28 36**.

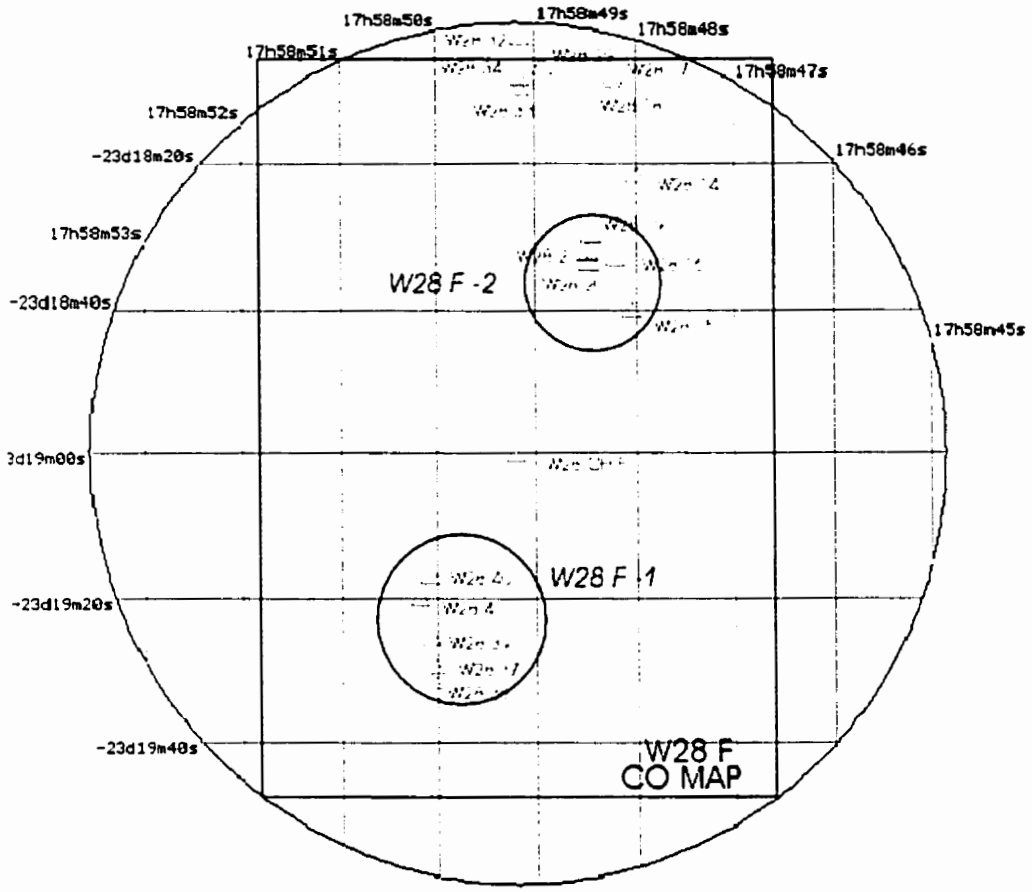

Figure 3.2: Observing fields in W28F region.

3.3 W28 - Results for CO Gas

3.3.1 W28E Region

As mentioned before, the W28E CO map was made with the ^{12}CO J=3 $\rightarrow$ 2 transition and centered on α(1950)= 17^h 58^m $48^s.78$, δ(1950)= -23° 18′00″.00. Figure 3.3 shows a map of integrated intensity, within the velocity range -40 km s^{-1} to 40 km s^{-1}, as well as the corresponding grid spectra. The original map had several bad spectra, at the offsets (-10″, -35″), (10″, -15″), (25″, -20″) and (35″, 25″), which were removed with the SPECX package and are shown as empty squares on the figure.

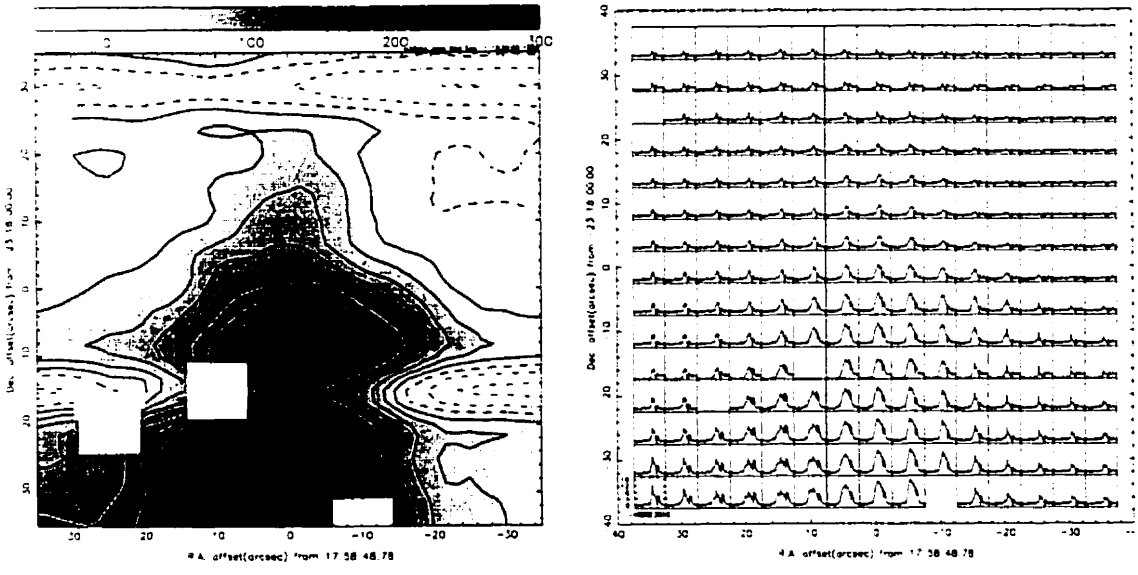

Figure 3.3: W28E region. Map of integrated intensity (left panel) and the corresponding grid spectra(right panel).

A spectrum at the position of the central CO clump, at offset (-10″, 0″) is shown in Fig. 3.4. An absorption feature is present at $\sim$ 18 km s^{-1}, probably due to

an off-source emission. The velocity range is about 35 km s^{-1}, in agreement with the velocity range of $\sim$ 50 km s^{-1} found by Pastchenko and Slysh (1974) from OH spectra and with the expansion velocity of W28 supernova of about $\sim$ 40 - 50 km s^{-1}, determined by Lozinskaya (1973) from optical measurements.

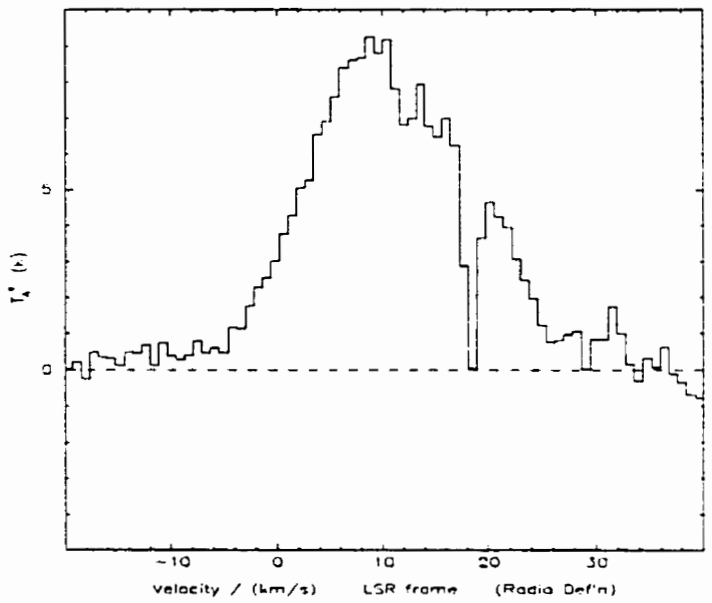

Figure 3.4: ^{12}CO J=3 $\rightarrow$ 2 spectrum at the central clump, at the offset (-10″, 0″) in W28E region.

A set of offsets have been chosen for further analysis, of interest because of their proximity either to the CO clump located at (0″, −10″), either to the (1720 MHz)OH masers (for the location of masers in W28E region, see Fig. 3.1 and Appendix B). The five offsets are shown in Table 3.1 together with their peak antenna temperature, velocity width at FWHM and the corresponding line intensity.

In choosing the offsets, we tried to follow the remarkable line of OH masers detected in this region (Claussen *et al.* 1997) and see if any changes occur in the intensity or the broadness of the emission lines. The intensity has a peak at the CO

Table 3.1: W28E: Line parameters for ^{12}CO J=3 → 2 emission.

Offset (″, ″)	T_A^* (K)	Δv_{FWHM} (km/s)	$\int T\Delta v$ (K km/s)
(0, -10)	12.6	22	253.7
(0, -25)	13.1	23	277.8
(0. 0)	8.9	22	157.5
(0. 10)	6.1	24	85.1
(0. 20)	4.6	24	57.8

clump at (0″. −10″), and it increases towards the south, in the direction of the W28F region. The lines show almost the same width, Δv ∼ 22 - 24 km s^{-1}. The emission is fainter than in W28F CO map. No clear connection could be seen between the CO gas emission and the line of (1720)OH masers, which could be explained by the fact that OH masers are a sign of hot (∼ 200 K) shocked gas, in contrast with ambient CO gas, which is at probably several tens of Kelvin.

3.3.2 W28F Region

Region W28F has been mapped in both ^{12}CO J=3 → 2 and ^{13}CO J=3 → 2 transitions. Both maps are centered on α(1950) = 17^h 58^m $49^s.18$, δ(1950) = -23° 19′ 00″.00, and extend 35″ × -35″ in α offsets and 55″ × -55″ in δ offsets. Fig. 3.5 and 3.6 show channel maps for both transitions, in the velocity range where most of the gas is present: -10 - 20 km s^{-1} for ^{12}CO and 0 - 16 km s^{-1} for ^{13}CO.

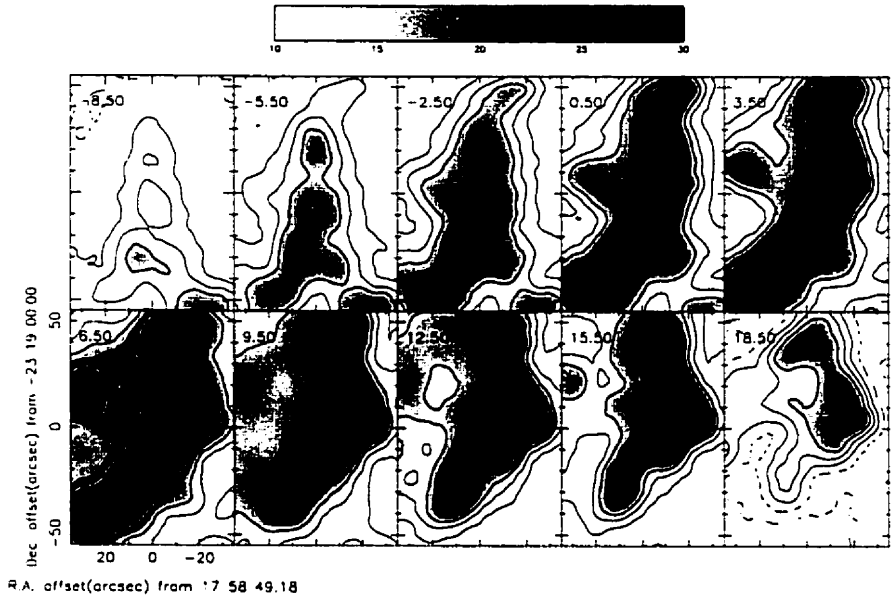

Figure 3.5: W28F. Channel map of integrated intensity in ^{12}CO J=3 → 2 emission.

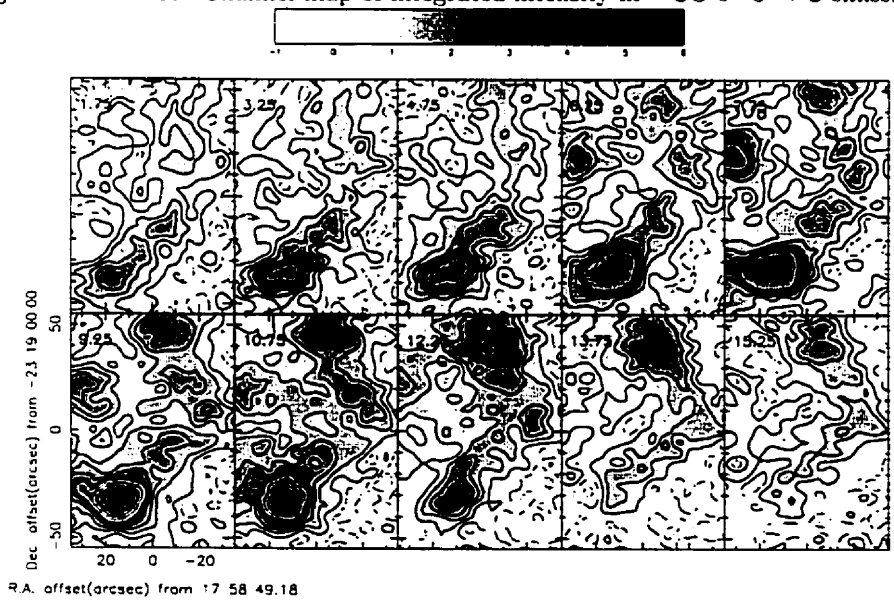

Figure 3.6: W28F. Channel map of integrated intensity in ^{13}CO J=3 → 2 emission.

There have been identified five distinct CO clumps, in both ^{12}CO J=3 → 2 and ^{13}CO J=3 → 2 velocity channel maps. Their locations (in offsets with respect to the map center) are: (-10″, -10″), (15″, -40″), (30″, 15″), (-20″, 5″), (-15″, 15″).

We considered the gas as being optically thick in the region where both ^{12}CO J=3 → 2 and ^{13}CO J=3 → 2 emission lines could be detected. ^{12}CO J=3 → 2 spectral lines were systematically much broader in velocity than the ^{13}CO J=3 → 2 lines.

The line parameters were calculated using the LTE assumption. For the velocity interval where both ^{12}CO and ^{13}CO could be detected (listed in Table 3.2 as "common velocity range"), the radiation temperatures can be calculated from the measured peak antenna temperatures. The optical depth (τ) is determined from the ratio of integrated intensities $^{12}CO/^{13}CO$, which we have calculated with the SPECX program. The optical depth and the radiation temperature allow the determination of the excitation temperature and column densities. With those parameters and estimating the radius of the clump, one can calculate total mass of the gas in the beam (see Appendix A.1 for details). The line parameters are shown in Tables 3.2 -3.4. For simplicity, the clumps were approximated to be spherical. Their real sizes have been calculated from the angular sizes (in arcsec) and assumed a distance of 2.5 kpc to the supernova (see Table 3.4).

A similar absorption feature as one encountered in the W28E region, was seen in W28F as well, in both ^{12}CO J=3 → 2 and ^{13}CO J=3 → 2 spectra, at $\sim$ 20 km s^{-1} (see for example CO spectra in Figures 3.7 - 3.9). Whenever the spectra were affected by the absorption feature, we have estimated what the value without absorption would be by fitting a Gaussian to the line. However, we notice that since this feature is located somewhat at the edge of the spectra and not close to the emission peak, it

does not cause a significant difference in the final result.

Table 3.2: W28F - Offsets. Velocity ranges.

Clump	Offset (″, ″)	^{12}CO Velocity range from: (km/s)	to: (km/s)	^{13}CO Velocity range from: (km/s)	to: (km/s)	Common velocity range Δv (km/s)
1	(-10, -10)	-10	20	-10	18	28
2	(15, -40)	-15	17	-9	17	26
3	(30, 15)	-7	31	1	17	16
4	(-20, 5)	-8	30	0	18	18
5	(-15, 15)	-8	28	-4	18	22

Table 3.3: Peak Antenna Temperatures, Integrated Intensities, ^{13}CO optical depth

Clump	Offset (″, ″)	T_A^* (^{13}CO) (K)	T_A^* (^{12}CO) (K)	I (^{13}CO) (K km/s)	I (^{12}CO) (K km/s)	$\tau_{^{13}CO}$ ($\times 10^{-2}$)
1	(-10, -10)	1.0	14.5	16.81	277.33	6.088
2	(15, -40)	2.8	16.7	31.84	260.92	13.0
3	(30, 15)	2.0	12.0	14.59	121.60	12.7
4	(-20, 5)	1.1	10.2	15.4	208.36	7.6
5	(-15, 15)	1.0	14.6	16.66	253.97	6.657

The values of the excitation temperatures are about $\sim$ 30 K, with slightly higher values for the clumps located in the vicinity of masers (clumps 2 and 5). We mention that a previous study (Frail & Mitchell, 1998) found a kinetic temperature of T_K = 80 $\pm$ 10 K, based on H_2CO data (namely the $[3_{03} - 3_{02}]/[3_{22} - 3_{21}]$ intensity ratio) at the offset (15″, -40″). However, the H_2CO emission is detectable from a much higer density gas than CO emission. Thus, the mean gas density within the beam will be

Table 3.4: Excitation temperatures, column densities, radii and masses of the clumps.

Clump	Offset (″, ″)	T_{ex} (K)	$N_{^{12}CO}$ ($\times 10^{17} cm^{-2}$)	Angular size (″)	Radius ($\times 10^{15} m$	M_{clump} ($M_{\odot}$)
1	(-10, -10)	33.5	6	13.83	5.17	11.9
2	(15, -40)	37.5	20	16.28	6	55
3	(30, 15)	28.9	10	8.14	3.04	7.3
4	(-20, 5)	25.6	5.6	16.28	6	15.3
5	(-15, 15)	33.7	6.7	10.5	3.93	7.6

higher for the H_2CO observations than for CO.

Conditions for Collapse. Energy Balance:

The core is supported against its own gravity by the sum of thermal, turbulent, rotational and magnetic energy. Gravitational collapse is possible only if gravitational energy overcomes all the other competing forms of energy:

$$| E_{grav} | > E_{th} + E_{turb} + E_{rot} + E_{mag} \tag{3.1}$$

E_{grav} is simply the gravitational energy of a sphere of mass M and radius R:

$$E_{grav} = -\frac{3}{5}\frac{GM^2}{R}, \tag{3.2}$$

where R is taken to be the angular size of the clumps (FWHM) as seen on the CO maps (see Table 3.4).

The thermal energy, E_{th}, under the assumption that the gas follows an ideal gas law, can be calculated with the relation:

$$E_{th} = \frac{3}{2}NkT = \frac{3}{2}\frac{M}{\mu m_H}kT, \tag{3.3}$$

where μ is the mean molecular mass per particle, which is 2.4 for a fully molecular cloud with 25% helium mass fraction, and $m_H = 1.67 \times 10^{-24}$ g.

E_{turb} is the turbulent energy and includes the kinetic contributions of internal motions. Its value can be estimated from the half-width of the emission line:

$$E_{turb} = \frac{1}{2} M_{clump} \cdot {v_{turb}}^2 = \frac{1}{2} M_{clump} \cdot {\Delta v_{FHWM}}^2 \tag{3.4}$$

The magnetic energy of the clump, E_{mag}, can be calculated with:

$$E_{mag} = \frac{1}{8\pi} \int B^2 dV = \frac{1}{6} B^2 R^3, \tag{3.5}$$

where B is the magnetic field strength and R is the radius of the clump.

We should mention though that, depending on the orientation of field lines, the magnetic field can prevent collapse of the clump or on the contrary, accelerate it. For the latter case, several studies suggest that if the magnetic field has a preferred direction, the collapse will occur most likely along the field lines. If the magnetic field is randomly orientated, the overall magnetic energy will act against the clump collapse.

The contributions of all the above types of energy have been calculated for all the five clumps. The results are shown in Table 3.5. An important result is that for all clumps, the turbulent motions exceed in magnitude the gravitational attraction ($E_{turb} \sim 10^{46} erg \gg E_{grav} \sim 10^{43} erg$), so the collapse is prevented. The contribution of the magnetic energy towards dissipation/collapse is not so easy to determine as it depends on the orientation of the magnetic field lines.

Magnetic fields in molecular clouds are difficult to measure and poorly known. Based on maser polarization studies (Claussen et al. 1997), the magnetic field strength around a few of the masers in the W28 F region was estimated to be of the order of: $B_{los} \sim 0.2$ mG $= 2 \times 10^{-8}$ T (see Appendix B). For a randomly oriented field, the mean value of the total magnetic field strength is $2B_{los}$, so the post-shock magnetic

Table 3.5: W28F - Energy balance.

Clump	Offset ("," ")	$\mid E_{grav} \mid$ $(\times 10^{43} erg)$	E_{th} $(\times 10^{43} erg)$	E_{turb} $(\times 10^{46} erg)$
1	(-10, -10)	4.32	4.09	2.65
2	(15, -40)	79.6	21.18	22
3	(30, 15)	2.77	2.17	1.65
4	(-20, 5)	6.16	4.02	3.44
5	(-15, 15)	2.32	2.63	1.71

field in W28 will be B_{ps} = 0.4 mG (Frail and Mitchell, 1998). However, there is only one clump ("clump 5") which is coincident with an OH maser (W28 21 maser). For the rest of the clumps, there is no direct connection with OH masers, so we could only imply a magnetic strength from the neighbouring regions. It is possible that the magnetic strength in the regions where there are no masers could be less than at the maser's locations, so the value of B = 0.4 mG should be taken as an upper limit to the magnetic field, meaning that the magnetic energy could be in this way overestimated.

For a clump of 10″ radius and a mean value for the magnetic field of B = 0.4 mG, the magnetic energy is $E_{mag} \sim 10^{46}$ erg, three orders of magnitude greater than than E_{grav}. Of course, if the magnetic field lines in W28F have a preferential orientation, it is possible that the collapse condition could be met for some clumps. However, we no indication that the magnetic field is highly orientated, so most probably the collapse is not occurring.

3.4 W28F - Results for Other Molecules

Several rotational and vibrational emission lines of different molecules were detected in W28F region, within the frequency range of 218.22 - 362.63 GHz. The emission lines are often weak, but broad, therefore bringing more evidence for gas being shocked. The importance of these detections consists in the fact that, unlike CO, those species trace the dense gas ($n_0 \sim 10^6$ cm^{-3}). Therefore, in addition to the low-density gas being shocked, we have now evidence of the dense gas being shocked.

The offsets which we chose for observation were: (15″, -40″), which is coincident with a peak ("clump 2") in the ^{12}CO J=3 → 2 and ^{13}CO J=3 → 2 maps, (-10″, 15″) and (-5″, 45″). As expected, the (15″, -40″) offset displays the strongest emission. However, all offsets show some broad molecular lines, which is a clear sign that the gas is shocked. Broad, but faint emission was detected at (-10″, 15″), for both HCO^+ ($J = 4 \rightarrow 3$) and HCN ($J = 4 \rightarrow 3$). No SiO ($J = 8 \rightarrow 7$) was detected, and H_2CO ($3_{03} - 2_{02}$) had a very faint and narrow emission. For the (-5″, 45″) offset, a good signal of HCN ($J = 4 \rightarrow 3$) was detected, but a faint H_2CO ($3_{03} - 2_{02}$) signal. Both have a broad extent in velocity ($\sim$ 20 km s^{-1}).

The spectra are shown in Figures 3.7 - 3.9 and the relevant line parameters (antenna temperatures and integrated intensities) are shown in Tables 3.6 - 3.8. For comparison, both ^{12}CO J=3 → 2 and ^{13}CO J=3 → 2 spectra were displayed for the same offsets, together with the other molecular transitions. The absorption feature at $\sim$ 20 km s^{-1} is clearly seen in the CO spectra, but it is not so noticeable in the other molecular spectra.

Offset (15″, -40″):

Table 3.6: W28F: Line parameters for other molecules. Offset (15″, -40″).

Molecule	Transition	Frequency (GHz)	T_A^* (K)	Δv (km/s)	$\int T\Delta v$ (K km/s)
CH_3OH	$J = 5 \rightarrow 4$	241.806	0.527	10	3.9
HCO^+	$J = 4 \rightarrow 3$	356.734	1.150	12	11.3
HCN	$J = 4 \rightarrow 3$	354.505	0.859	15	14.7
H_2CO	$3_{03} - 2_{02}$	218.222	0.252	12	2.2
HNC	$J = 4 \rightarrow 3$	362.630	0.371	10	3.1
^{12}CO	$J = 3 \rightarrow 2$	345.795	17.42	20	277.7
^{13}CO	$J = 3 \rightarrow 2$	330.587	3.94	10	28.7

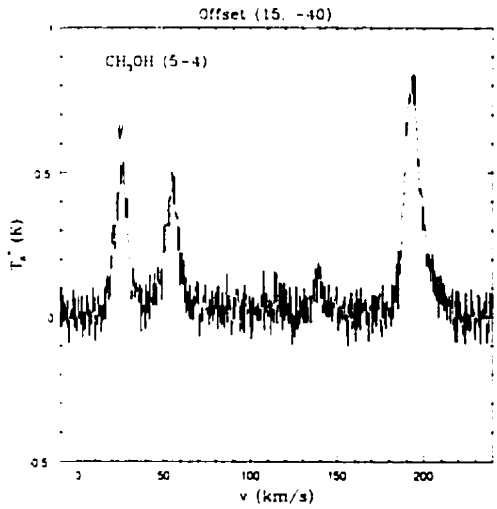

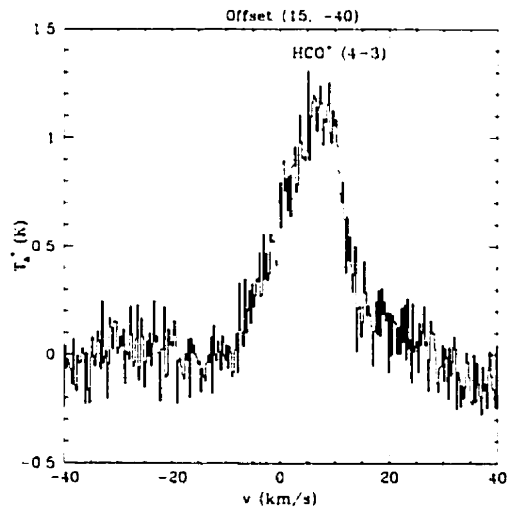

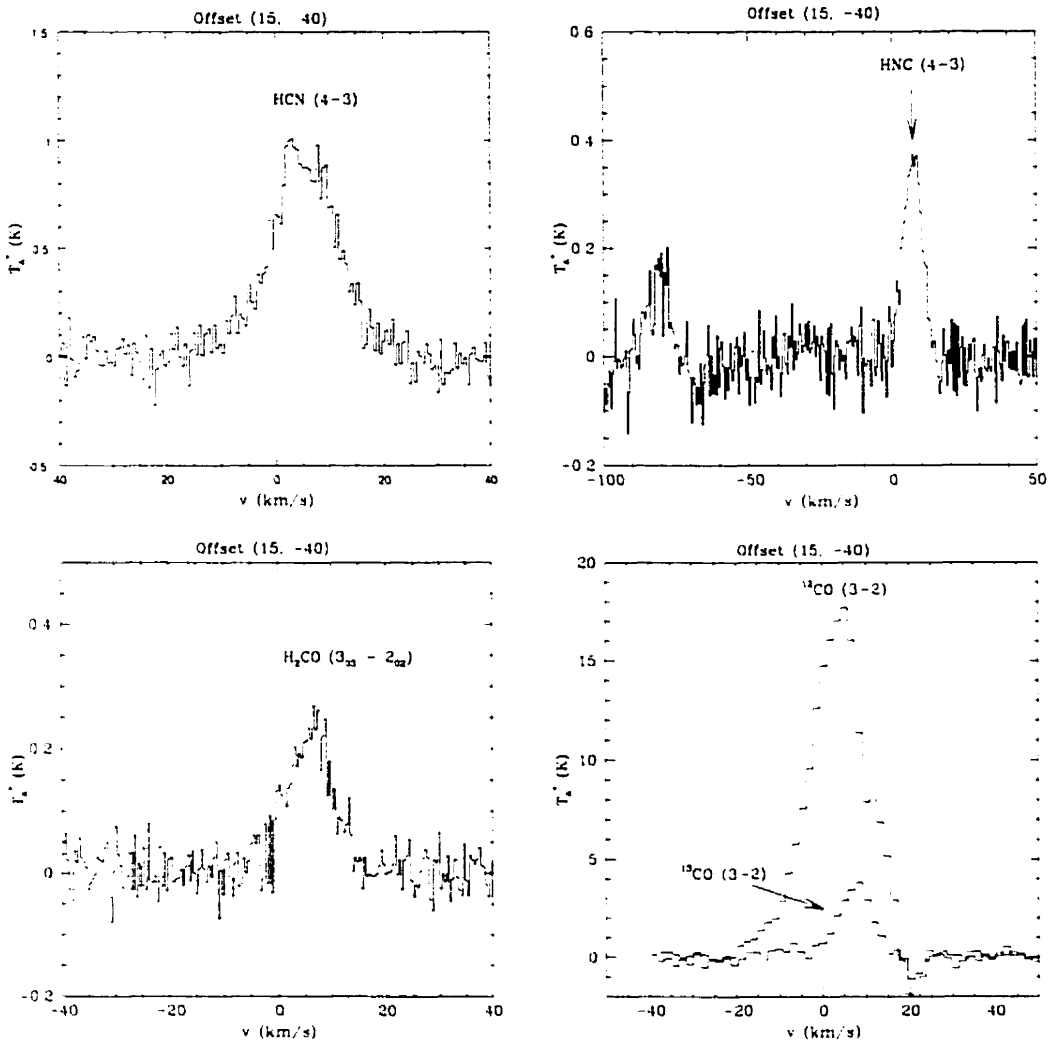

Figure 3.7: W28F. Spectra of several molecules at offset (15″, -40″).

Offset (-10″, 15″):

Table 3.7: W28F: Line parameters for other molecules. Offset (-10″, 15″).

Molecule	Transition	Frequency (GHz)	T_A^* (K)	Δv (km/s)	$\int T\Delta v$ (K km/s)
SiO	$J = 8 \rightarrow 7$	347.033	-	-	-
HCO^+	$J = 4 \rightarrow 3$	356.734	0.278	20	5.3
HCN	$J = 4 \rightarrow 3$	354.505	0.319	20	6.0
H_2CO	$3_{03} - 2_{02}$	218.222	0.135	2	0.1
^{12}CO	$J = 3 \rightarrow 2$	345.795	14.4	25	312.8
^{13}CO	$J = 3 \rightarrow 2$	330.587	1.22	15	15.6

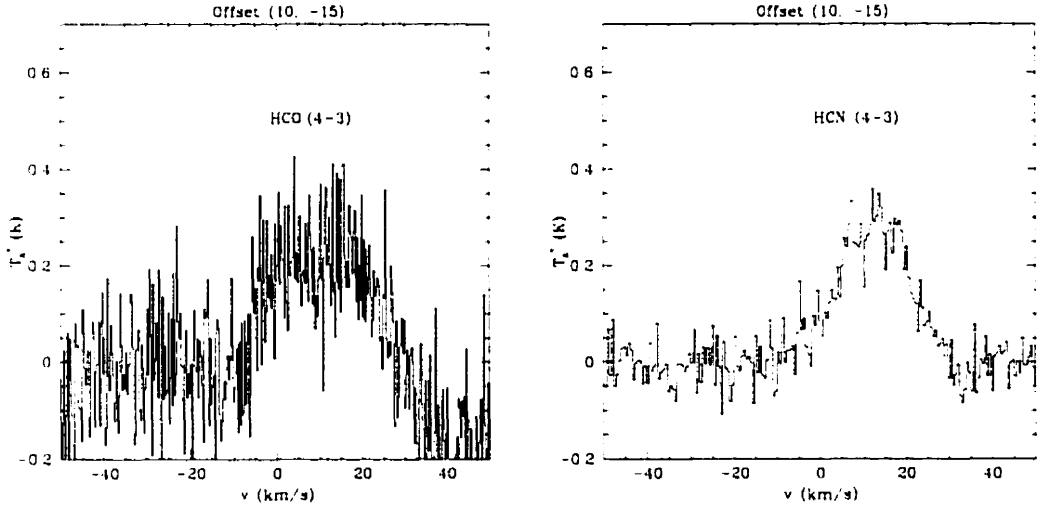

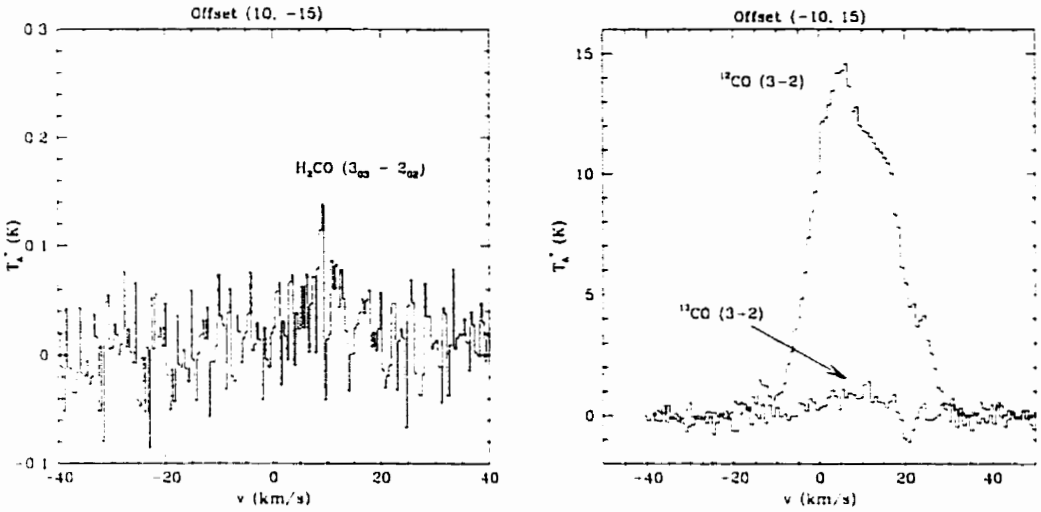

Figure 3.8: W28F. Spectra of several molecules at offset (10″, -15″).

Offset (-5″, 45″):

Table 3.8: W28F: Line parameters for other molecules. Offset (-5″, 45″).

Molecule	Transition	Frequency (GHz)	T_A^* (K)	Δv (km/s)	$\int T \Delta v$ (K km/s)
HCN	$J = 4 \rightarrow 3$	354.505	0.621	20	9.1
H_2CO	$3_{03} - 2_{02}$	218.222	0.08	10	0.7
^{12}CO	$J = 3 \rightarrow 2$	345.795	12.1	25	254.5
^{13}CO	$J = 3 \rightarrow 2$	330.587	1.92	15	21.7

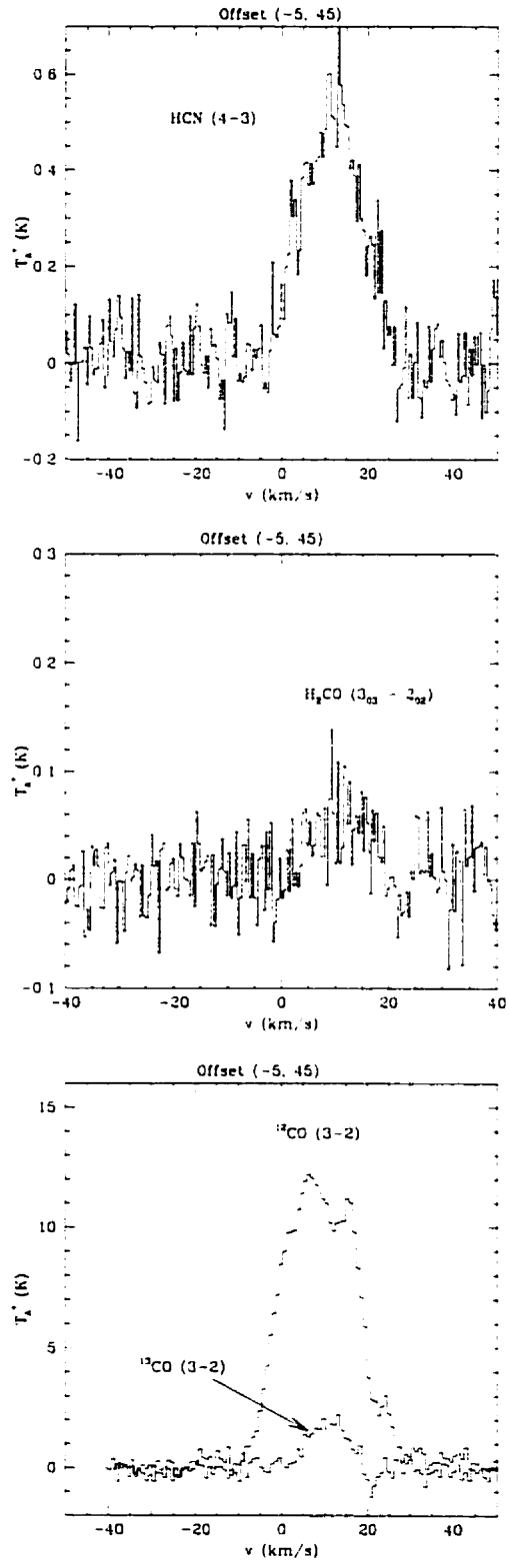

Figure 3.9: W28F. Spectra of several molecules at offset (-5″, 45″).

3.5 W28F - Results for Shocked H_2

Near-infrared observations have been done for two fields within the W28F region, labelled as "W28F-1" and "W28F-2". The BEAR field had a diameter of 23". Figure 3.1 shows the position of BEAR fields within the CO maps in the W28F region. Both observations used the narrow band filter, centered on the v= 1-0 S(1) line of H_2. The range in frequency was: 4657.57 to 4783.45 cm^{-1} (or in wavelength, from 2.09 to 2.14 μm)

W28F-1 Region

W28F-1 region was centered on coordinates: $\alpha(1950) = 17^h\ 58^m\ 49^s.84$, $\delta(1950)$ = -23° 19′ 25″.00, with a radius of 11.5". The H_2 emission in the entire field (23"), shown in Figure 3.10, displays a striking correspondence with the line of masers.

The intensity of the H_2 line for the entire field is shown in Figure 3.11, where it is compared with the CO emission line, identified at the same location [offset (10", -30") in the W28F map of CO]. We can estimate of the shock velocity from the FWHM of the H_2 emission to be $\sim$ 40 km s^{-1}. The CO line is also broad, $\sim$ 20 km s^{-1} (FWHM), which is a clear sign of shocked gas. With the velocity resolution available for the H_2 observations of 12.54 km s^{-1}, the peak of emission it is seen to occur at v_{LSR} (H_2) = 6.5 km s^{-1}. For comparison, for CO observations, v_{LSR} is 12.0 km s^{-1}.

The line intensity in the whole BEAR field, uncorrected for extinction, has a value of 1.6 × 10^{-4} erg s^{-1} cm^{-2} sr^{-1}. We have selected six different regions within the W28F-1 field, denoted in Figure 3.10 as A, B, C, D, E and F. Using the BEAR data reduction package (François Rigaud and Jean-Pierre Maillard), it is possible to visualize spectra within 1" aperture, and results for such individual spectra from the

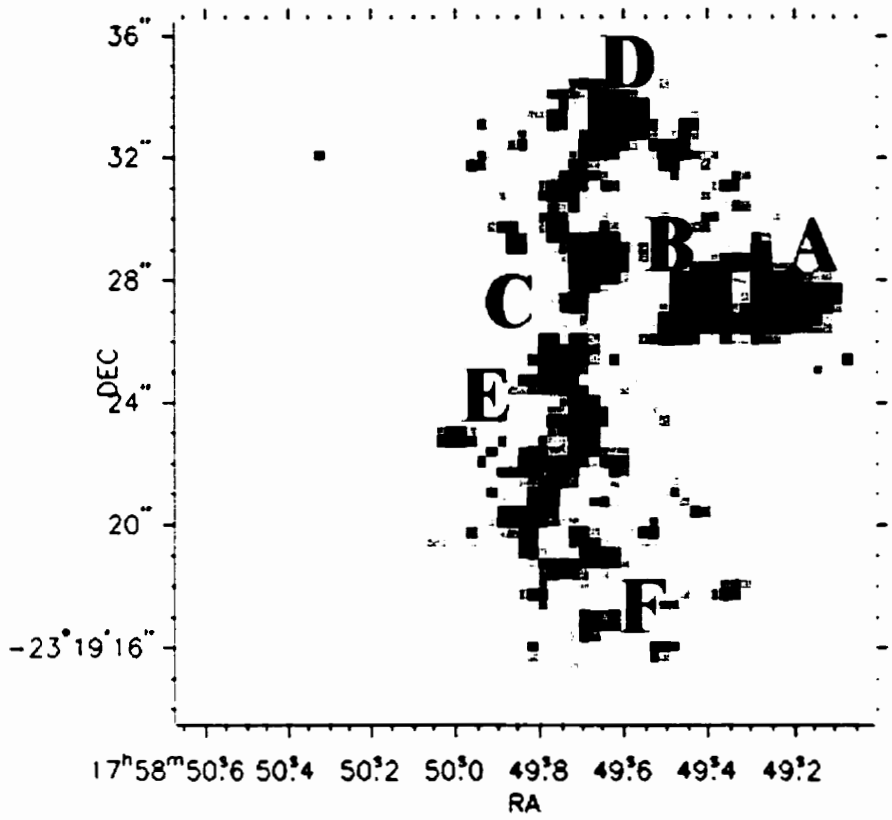

Figure 3.10: Ridge of H_2 emission in W28F-1 field (v=15 km s^{-1})

above selected regions are displayed in Figure 3.12. The fact that the line shapes and strengths vary over sub-arcecond angular distances suggests that the common assumption made in literature of plane–parallel supernova shocks may not be valid. In turn, other shock geometries, like bow shocks for example, could give better results.

All the individual spectra have line-widths ranging from 20 km s^{-1} (region F) to 50 km s^{-1} (regions A and B). Also, v_{LSR} displays a slight shift from region to region. The S(1) 1 - 0 lines are not perfectly symmetric. This could be a sign of internal reddening. The predominance of blue-shifted velocities in the H_2 line-profile may

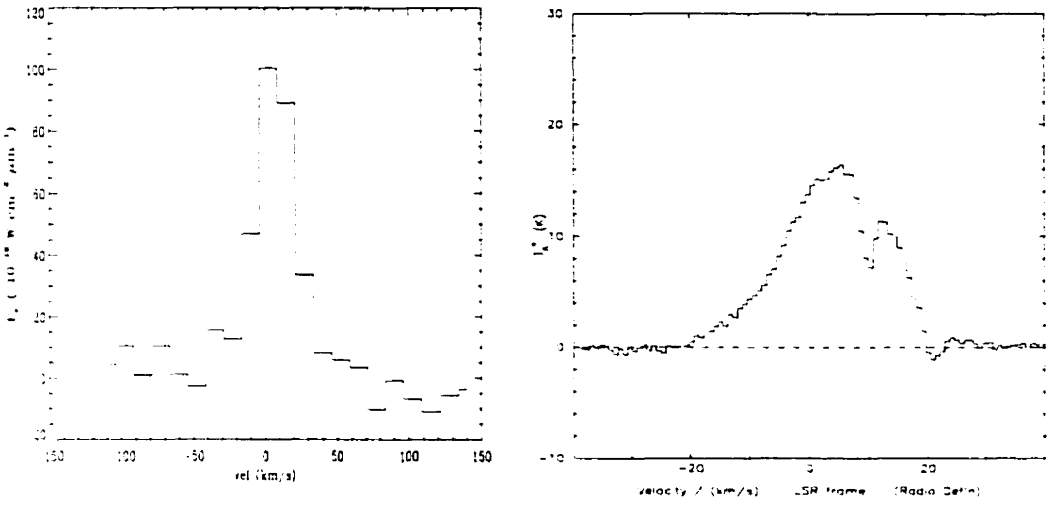

Figure 3.11: H_2 line flux for W28F−1 field (left panel) compared with quiescent CO (right panel) at the same position (10″, -30″).

arise from an expanding dusty emission region in which the red-shifted molecules suffer more extinction than the blue-shifted ones (Nadeau *et al.*, 1982).

The distribution of shocked H_2 varies with velocity, over the entire velocity range (from -46 km s^{-1} to + 44 km s^{-1}). The strongest emission occurs around 6 km s^{-1}. Two distinct emission peaks are seen within - 46 km s^{-1} to +15 km s^{-1}. A strong emission feature is detected in the SW region, ranging from -14 km s^{-1} to +5 km s^{-1}. At 15 km s^{-1}, the "filament" (or H_2 ridge of emission) is clearly seen and it is determined to be displaced by a few arcseconds with respect to the line of OH masers. The fact that the line of masers and the H_2 filament emission have similar configurations but they are separated from one another, can be explained if both types of emission originate in the post-shocked gas, for example the shocked H_2 emission originating from a hot region of gas ($\sim$ 2000 K) and the OH maser emission from a cooler portion of gas ($\sim$ 200 – 400 K). Finally, a distinct H_2 feature

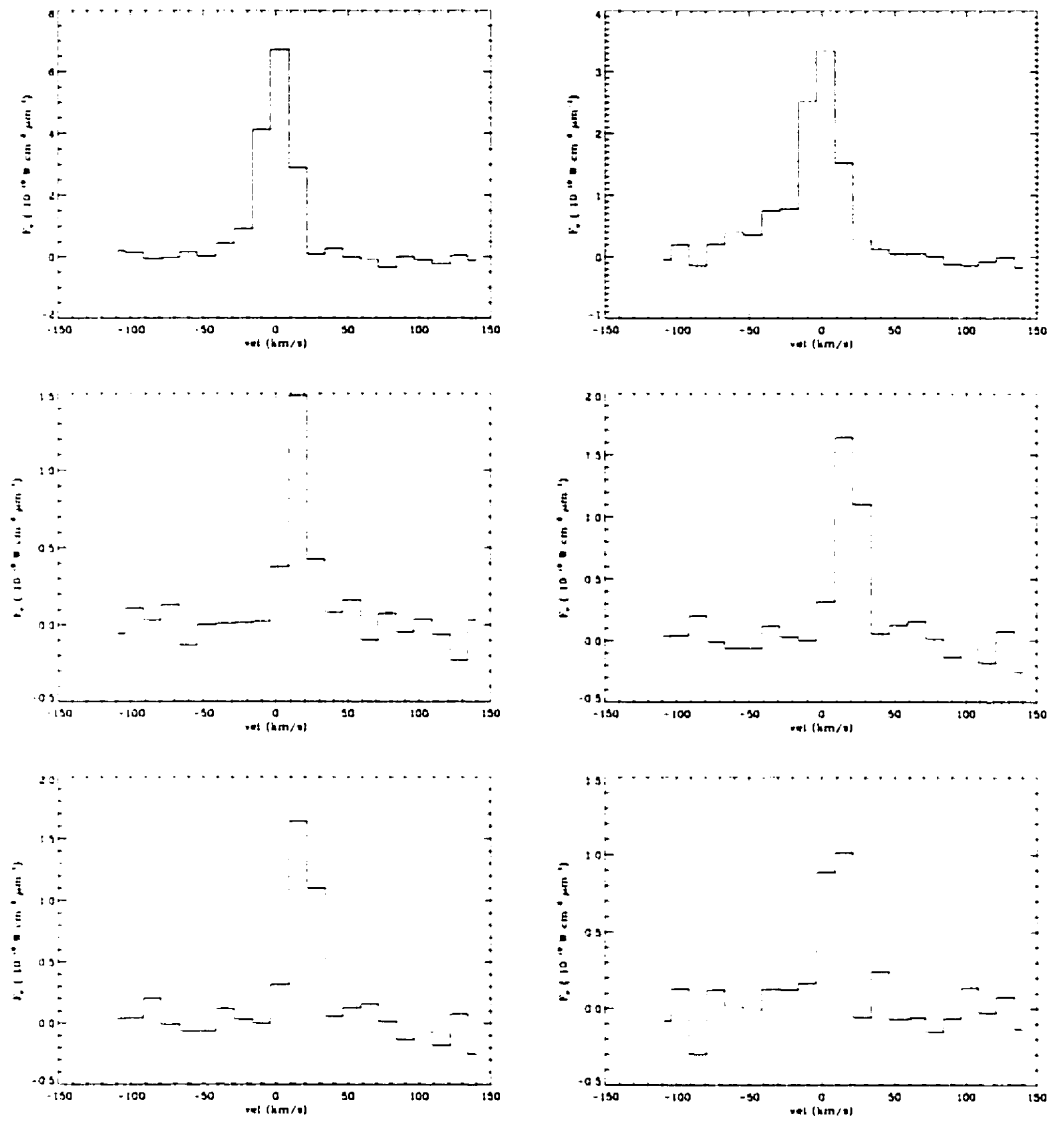

Figure 3.12: W28F-1. Line fluxes in regions (from left top to bottom right): A, B, C, D, E, F.

is observed in the NW, at the edge of the emission line, extending in velocity from 24 km s^{-1} to 34 km s^{-1}.

The velocity of masers in W28F (between 9.11 to 15.24 km s^{-1}) agree within a

few km s^{-1} with v_{LSR} of CO and other molecular species (12 km s^{-1}), or shocked H_2 (6.5 km s^{-1}).

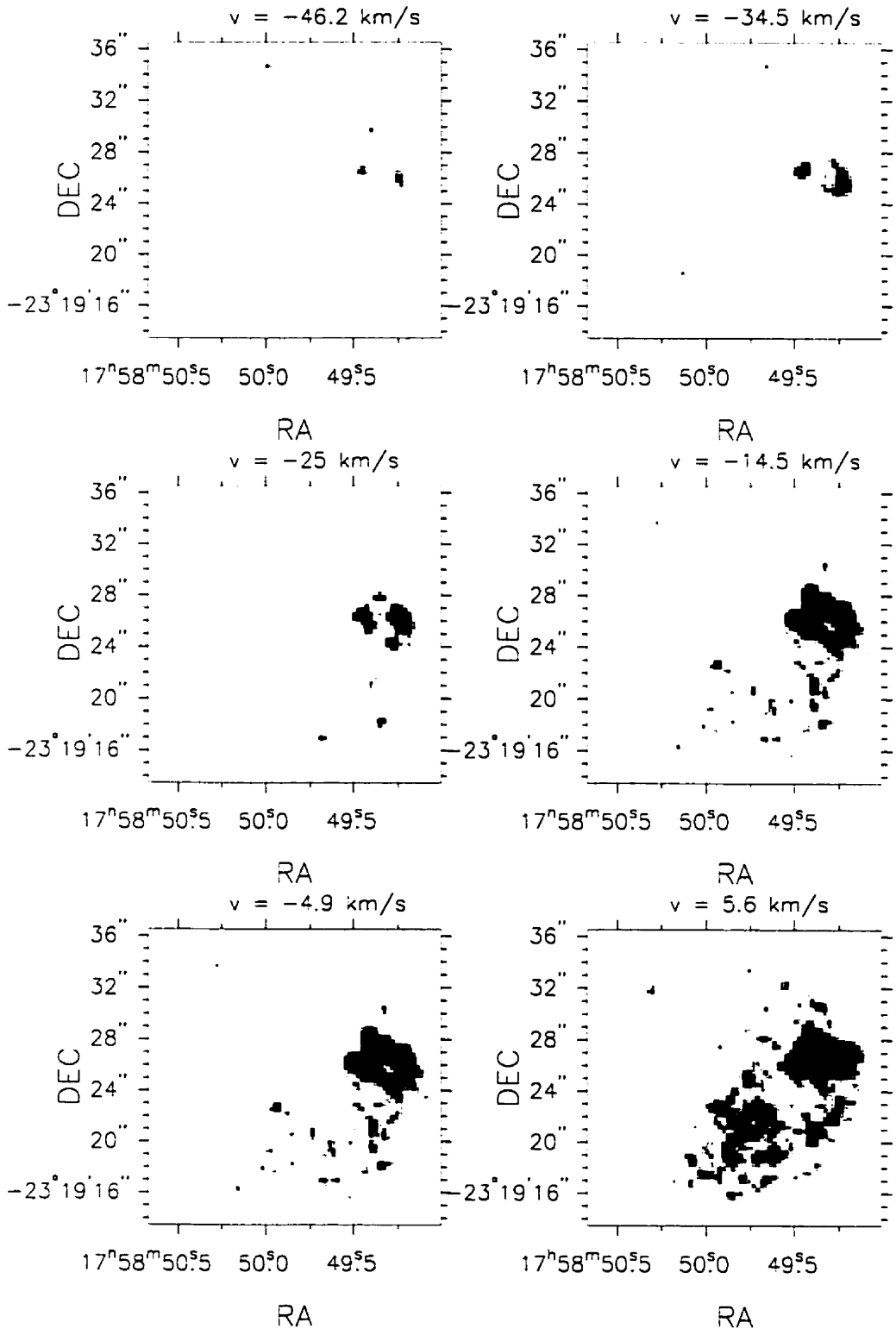

Figure 3.13: Morphology of the H_2 shocked gas for different velocity channels in W28F-1 region (continued).

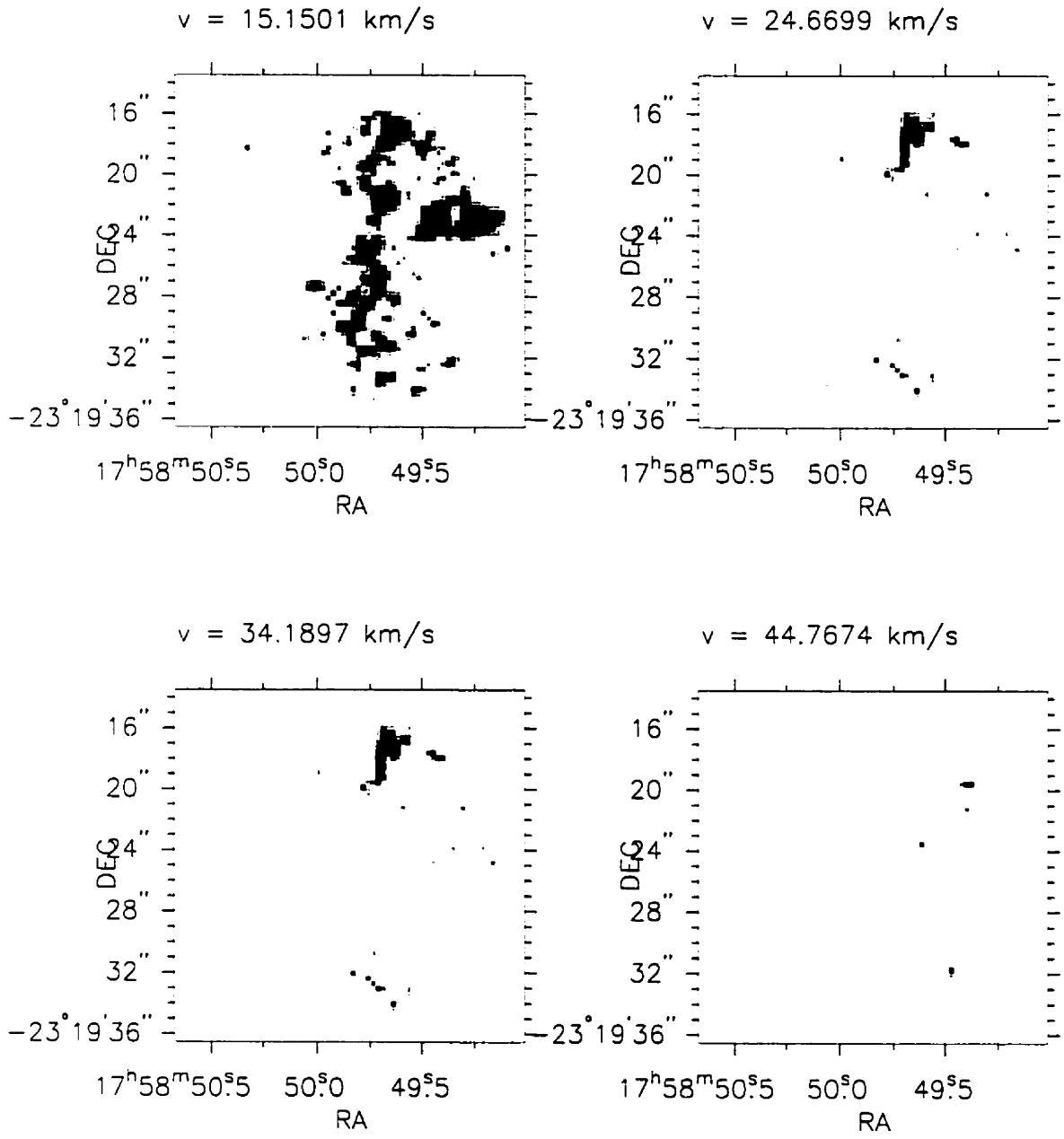

Figure 3.14: Morphology of the H_2 shocked gas for different velocity channels in W28F-1 region (continued).

W28F-2 Region.

The W28F-2 region is centered on the coordinates: $\alpha(1950) = 17^h\ 58^m\ 48^s.52$, $\delta(1950)$ = -23° 18′ 40″.00, with the same BEAR field radius, of 11.5″. The peak emission of H_2 is detected at v_{LSR} (H_2) = 9.87 km s^{-1}, with a velocity resolution of 12 km s^{-1}. A total emission in the 23″ field is shown in Figure 3.15.

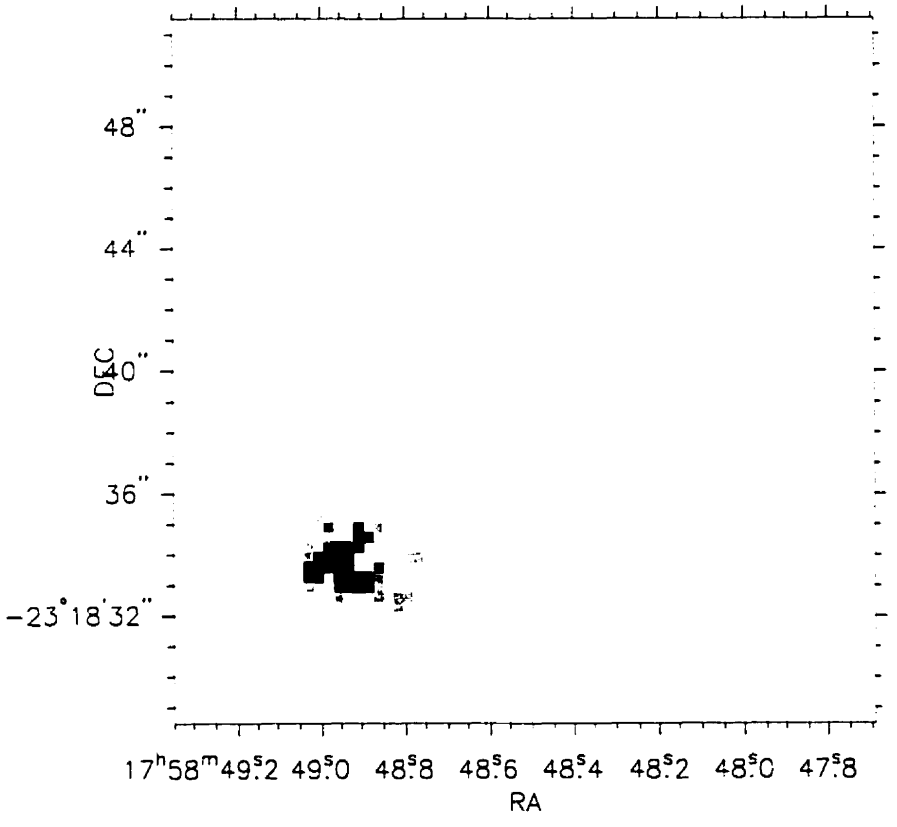

Figure 3.15: Shocked H_2. Total emission in "W28F-2" BEAR field.

In the same manner as for the W28F−1 region, a comparison with the CO line emission from the same location (offset (-10″, 15″) in the W28F map of CO) has been done (see Figure 3.16).

The line flux over the entire 23″ field is $F_{H_2} \sim 1 \times 10^{-3}$ erg cm^{-2} s^{-1} sr^{-1}.

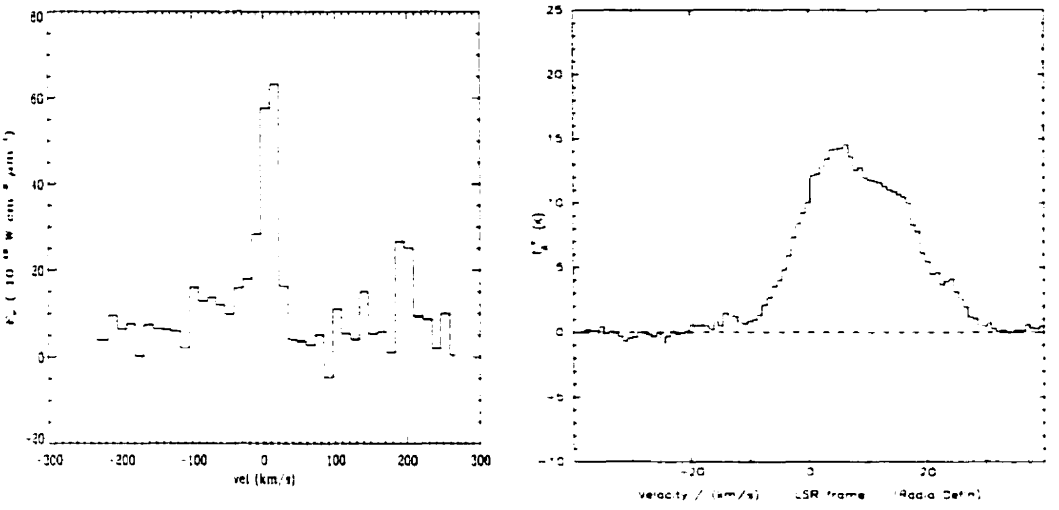

Figure 3.16: H_2 Line flux for W28F-2 field compared with quiescent CO at the same position (-10″, 15″).

The morphology of the H_2 gas has also been inspected. The bright emission to the south-east (in Figure 3.17) is a continuum emission, coming from a field star, and positioned at $\alpha(1950) = 17^h\ 58^m\ 49^s$; $\delta(1950) = -23^\circ\ 18'\ 46''$. There is a faint 2.12 μm emission extending in the velocity range -4 km s^{-1} to +24 km s^{-1}. The emission is located in the center and in the northwestern part of the field. There is also sign of shocked gas around the field star (but probably, these two features are uncorrelated if the star is not at the same distance as the shocked gas). Therefore, the shocked emission of H_2 in this region could probably belong to the supernova remnant.

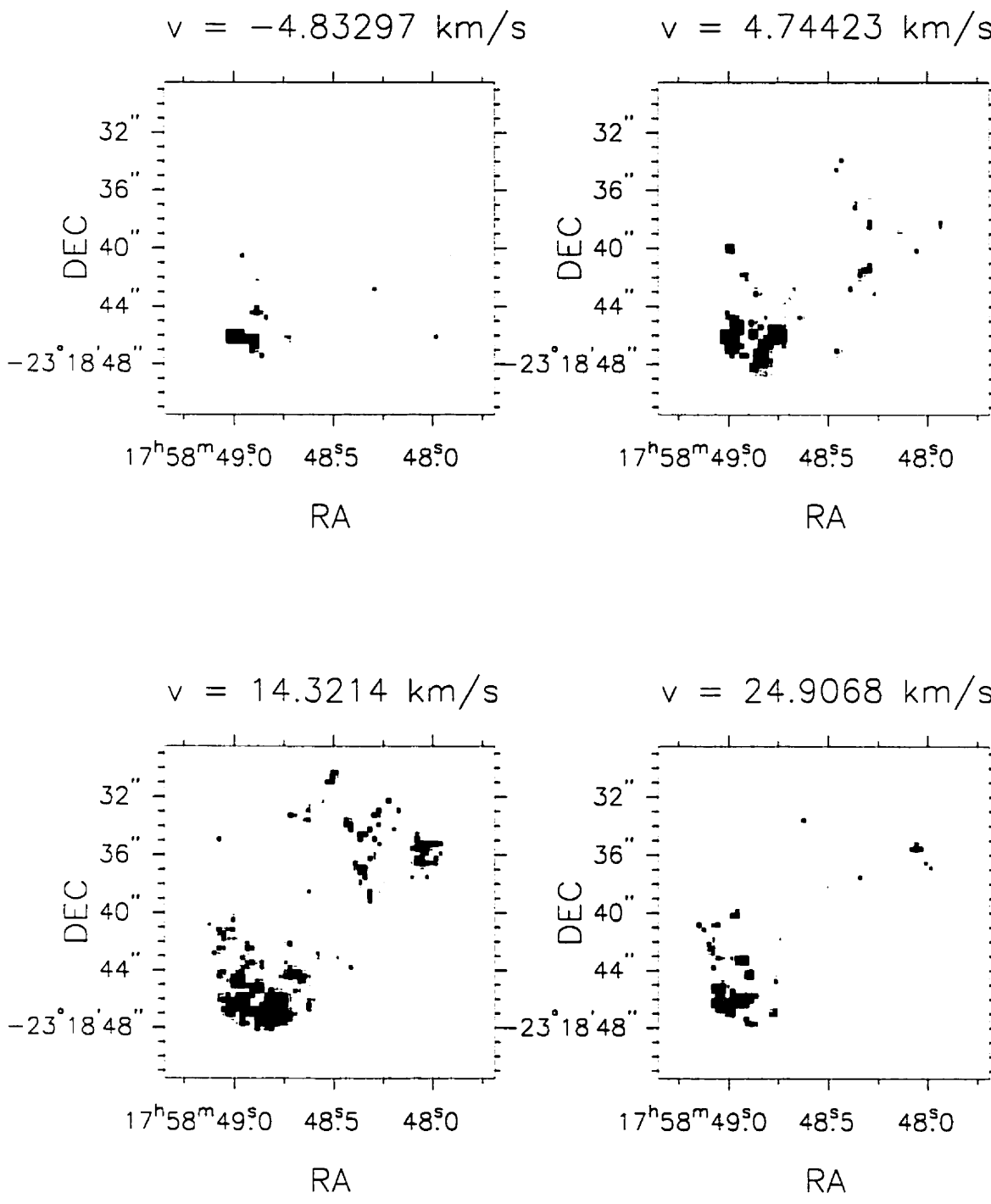

Figure 3.17: Morphology of the H_2 shocked gas for different velocity channels in W28F-2 region.

Chapter 4

The W44 Supernova Remnant

4.1 W44. Introduction

W44 (also G34.7-0.4, G34.6-0.5, 3C392) is a supernova remnant situated in the galactic plane at a distance of about 2.5 kpc (Shelton *et al.*, 1999). The celestial coordinates are: $\alpha(1950) = 18^h\ 53^m\ 30^s$, $\delta(1950) = +01^\circ\ 18'\ 00''$ (SIMBAD database) and the radius $\sim$ 11 - 13 pc. The age of the remnant is approximately 20.000 years, consistent with the age of the associated pulsar, PSR B1853+01 (Wolszczan *et al.*, 1991).

In radio continuum maps (Giacani *et al.*, 1997), W44 appears as an elongated shell remnant, with the angular size of $25' \times 35'$. On the eastern side the radio emission is brighter, with filamentary structure contained within a sharp boundary.

ROSAT X-ray observations (Rho *et al.*, 1994) show thermal emission centrally concentrated, and dim outer edges extending in the north, south and west, as far

as the radio continuum shell. The X-ray emitting region might also extend to the eastern edge, where it could be absorbed by a foreground molecular cloud (which extends from $\alpha(1950) = 18^h\ 53^m\ 40^s$ to $18^h\ 54^m\ 55^s$, $\delta(1950) = +01°\ 10'$ to $+01°\ 20'$) (Wootten, 1977). Rho *et al.* (1994) found temperatures for the X-ray emitting gas in the range of 3.9 to 7.6 $\times$ 10^6 K and column densities for the intervening absorbers from 1.6 to 2.1 $\times$ 10^{22} cm^{-2}.

Giacani *et al.* (1997) have observed Hα and [SII] emission. The optical emission is within the boundaries of the radio shell, with filaments that correlate very well with radio continuum filaments. On the other hand, the optical and X-ray correlation is poor. This implies that there is not so much dense gas in the interior of the remnant (as would be the case if Hα is emitted by relatively dense clouds evaporating in the interior of the remnant). Thus, this non-correlation could be an evidence against the model of W44 interacting with a molecular cloud (Shelton *et al.*, 1999).

Koo & Heiles (1995) have mapped W44 at 21 cm, resolved its velocity structure, and found HI emission up to $\sim$ 210 km s^{-1}. After subtracting the systemic velocity of the molecular cloud ($\sim$ 43 km s^{-1}), they estimated that the surrounding shell is expanding with a velocity of 150 $\pm$ 15 km s^{-1}. As for the near side of the remnant, Koo & Heiles (1995) didn't find any emission with v_{LSR} < - 70 km s^{-1}. Based on their position-velocity diagrams, they also concluded that the HI is distributed interior to the radio continuum shell. The mean HI column density was estimated to be $\sim$ 3 $\times$ 10^{19} cm^{-2}.

ISO observations (Reach and Rho, 1996) detected continuum dust emission, consistent with dust heated by the diffuse interstellar radiation and dominated by pre-shock and unrelated clouds. Reach and Rho (1998) also made ISO spectroscopic

observations of H_2O, OH, CO in far infrared, within a region centered on an OH maser ($\alpha(1950) = 18^h\ 56^m\ 28^s.4$; $\delta(1950) = 01°\ 29'\ 59''$), with the Long Wavelength Spectrometer (beam-size $\sim$ 80 ").

(1720 MHz) OH masers in W44 were detected by Claussen *et al.*(1997). The maser emission was interpreted as being collisionally excited by the supernova shock passing through a molecular cloud.

Reach and Rho (1996) observed bright $[OI]$ (63 μm) emission, enhanced on the edge of the remnant, and higher in the center of the remnant. The [OI] peak surface brightness is 10^{-3} erg cm^{-2} s^{-1} sr^{-1} and remnant's total luminosity in this line, 1000 $L_\odot$. Reach and Rho (1996) interpreted the [OI] emission also as shock excited and as evidence that W44 is interacting with a molecular cloud.

Although [OI] line emission and OH maser emission were both interpreted to be caused by the interaction of the supernova remnant with an adjacent molecular cloud, an analytical model of Shelton *et al.*(1999) it's used to argue that W44 could be understood within a context that doesn't require such interaction. The required ingredients to the model are a relatively dense ambient environment (about 6 cm^{-3}), a significant density gradient, shell corrugation caused by the irregularities in the ambient medium and a significant amount of thermal conduction in the hot interior.

4.2 W44 Observing Fields

Figure 4.1 illustrates the observed E and F regions, with CO mapping and near-infrared (BEAR) observations (circles). The small triangles identify the OH masers in the field. For this plot, we used the SIMBAD database, with an identification

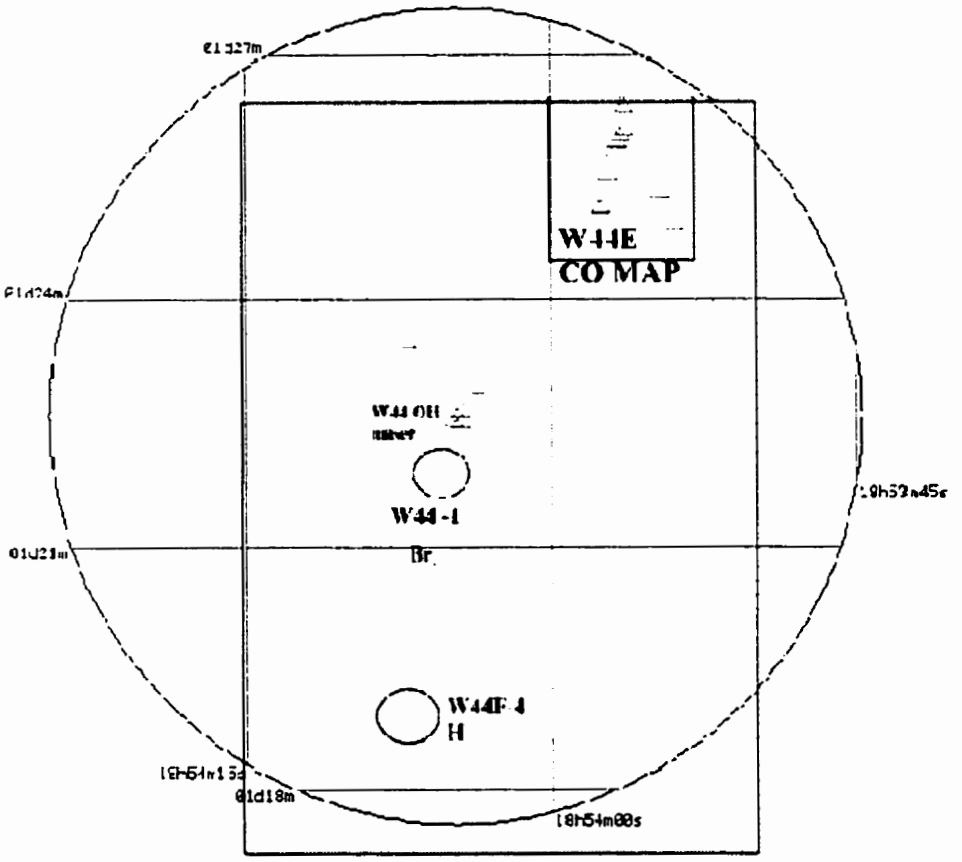

Figure 4.1: W44 (1720 MHz)OH masers

of objects centered on the W44 OH F maser ($\alpha(1950) = 18^h\ 54^m\ 04^s.7$; $\delta(1950) = 01°\ 22'\ 35''$) and within a radius of 5 arcmin. The velocity dispersion of the maser features is typically less than a few km s^{-1} and the mean maser velocity is equal to the systemic velocity of the remnant (Claussen *et al.*, 1997).

There are no OH masers located in the near-IR (BEAR) fields. This in turn, gives us the possibility of studying the shocked gas which is not directly connected

with the masers.

Magnetic field measurements of masers in W44F region (Claussen *et al.*, 1997) give line of sight values of B_{los} = -0.12 ± 0.03mG, for W44 24 maser and B_{los} = -0.30 ± 0.07 mG, for the W44 23 maser.

W44E Region.

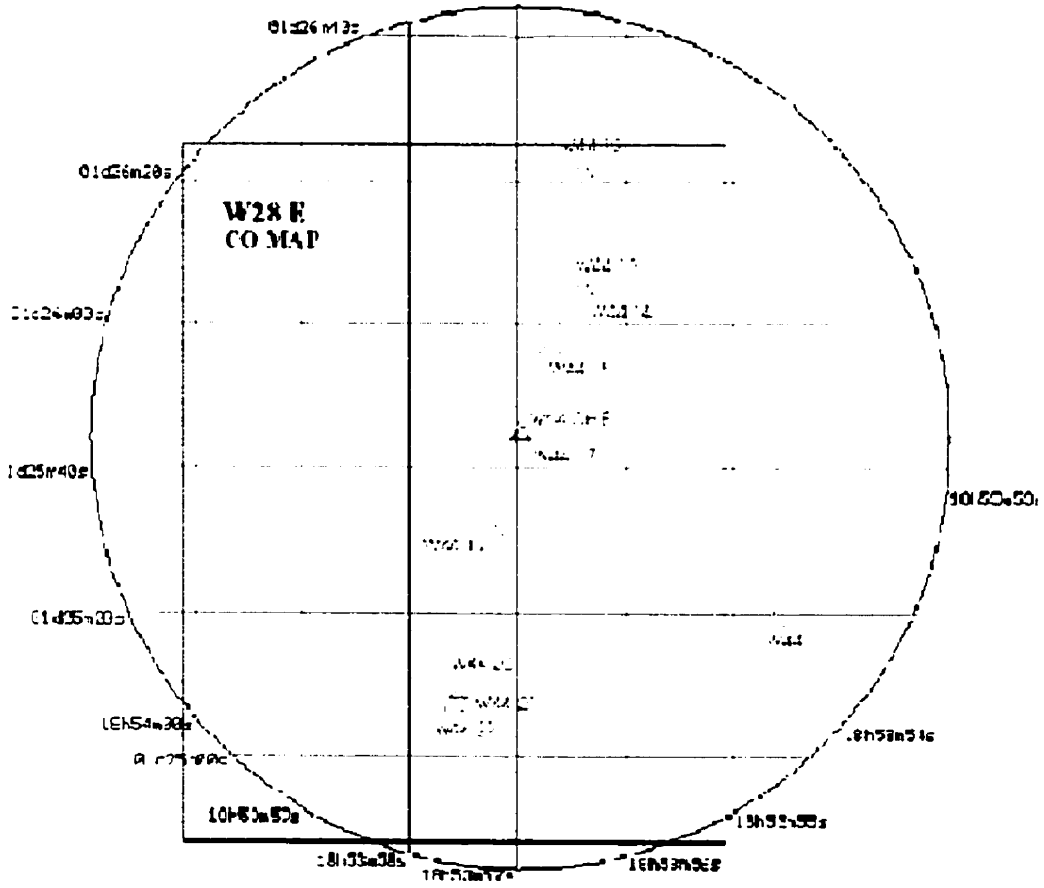

Figure 4.2: W44E (1720 MHz)OH masers

Figure 4.2 shows a circular grid, centered on W44 OH E maser ($\alpha(1950) = 18^h\ 53^m\ 57^s.0$, $\delta(1950) = 01°\ 25'\ 4''$), with a radius of 1 arcmin. Our CO map in the W44E

region is shown superimposed on this grid as a rectangle scaled to the appropriate units. A clear line of (1720 MHz)OH masers is observed, extending from N to S (see Appendix B for the identification of masers in the observed field). More interestingly, this line of masers coincides with a filamentary CO emission (compare for example Figure 4.2 with Figure 4.4).

We do not have any near-IR observations in the W44E field.

The magnetic field measurements of masers in W44E region are: B_{los} = -0.23 ± 0.09 mG, for W44 20 and B_{los} = -0.28 ± 0.09 mG, for W44 11 maser.

4.3 W44 - Results for CO Gas

The ^{12}CO J=3 → 2 emission map in the W44 (E + F regions) is centered on $\alpha(1950) = 18^h\ 54^m\ 04^s.66$, $\delta(1950) = 01°\ 22'\ 35''$ and extends in α offsets from 155″ to -220″ . and in δ offsets, from 225″ to -350″ (see Figure 4.3). The shock generated by the supernova explosion that occurred ~ 10^3 years ago encountered the nearby molecular gas at the eastern edge of the remnant. The molecular ridge corresponds to a location where the interaction between the blast wave of the supernova and the ambient molecular gas is strong. A similar feature can be seen in X-ray, radio or optical measurements as well (Giacani *et al.*, 1997; Frail *et al.*, 1996a; Kassim, 1992; Seward, 1990).

The horizontal stripes seen in Figure 4.3 are not true emission, but noise generated by the raster scanning technique. Our ^{12}CO J=3 → 2 data in the W44 region were affected by a spectral absorption feature (probably an off-source emission), very close to the CO emission peak, at ~ 40 km s^{-1} (see, for example the last panel in

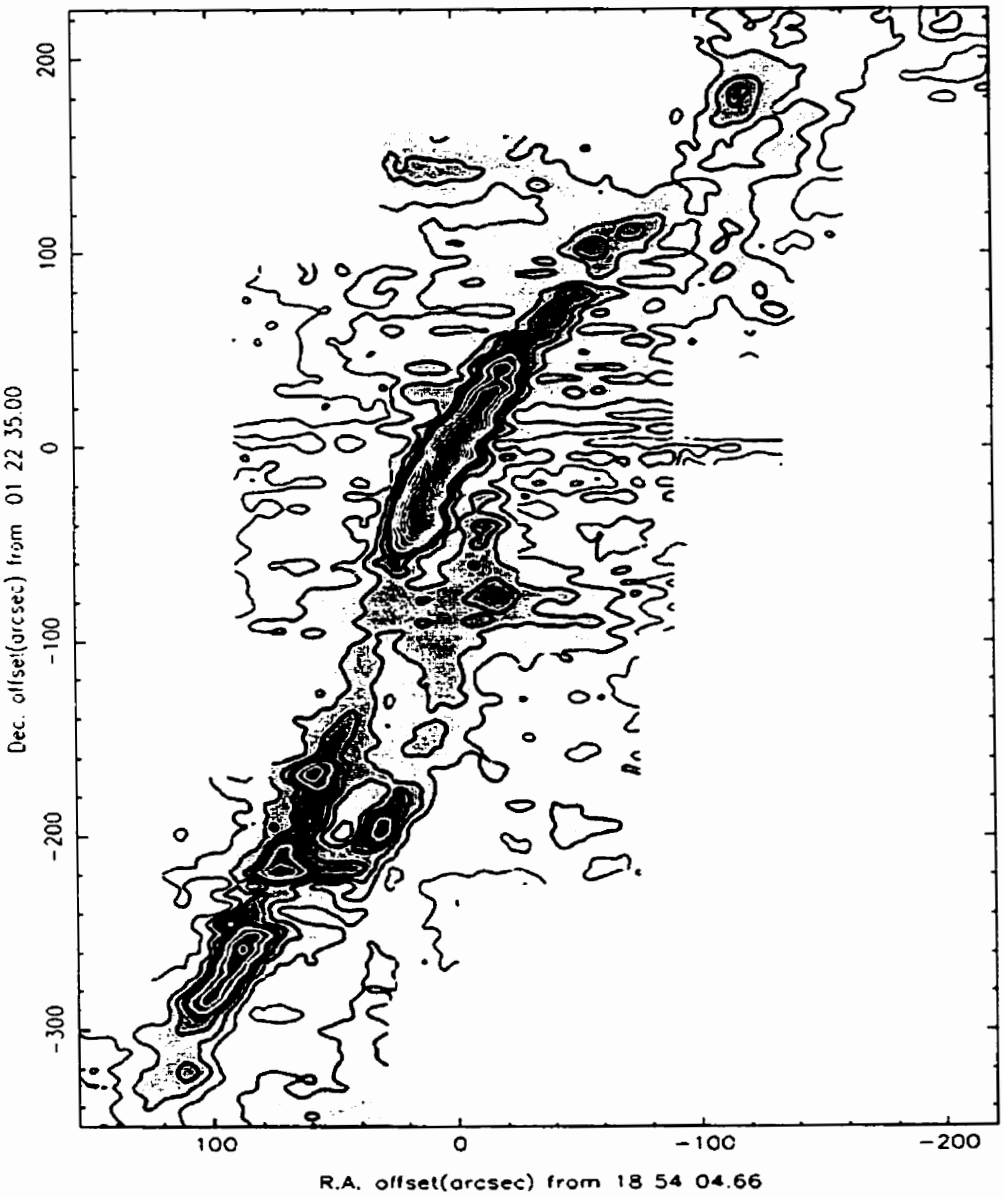

Figure 4.3: W44 - E and F regions. Map of integrated intensity of ^{12}CO J=3 → 2 Emission.

Figure 4.7). Since we don't have a good estimate of the missing line shape, we restrain our calculations to the observable emission, which respresents mainly the gas

in the blue wing.

4.3.1 W44E Region

A ^{12}CO J=3 $\rightarrow$ 2 emission map has been taken for the W44E region, centered on coordinates $\alpha(1950) = 18^h\ 53^m\ 56^s.98$, $\delta(1950) = 01°\ 25'\ 45''$. The map extends in α offsets from 35″ to -35″ and δ offsets from 60″ to -60″ . We have also a ^{13}CO J=3 $\rightarrow$ 2 spectral detection for the offset (0″, 0″).

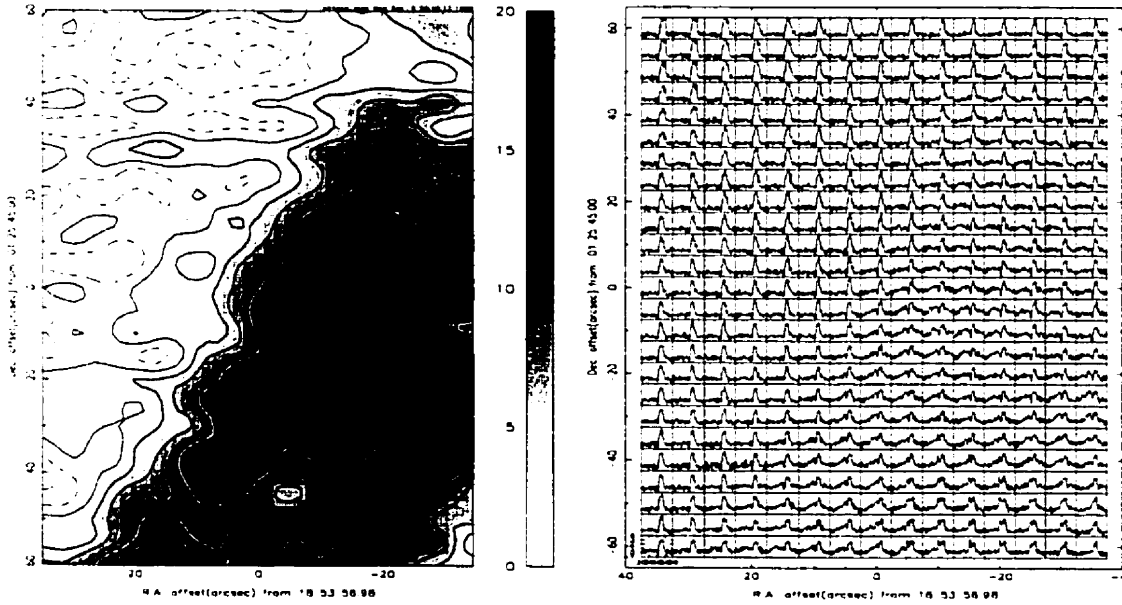

Figure 4.4: W44E Integrated intensity in the blue-shifted wing (20-40 km s^{-1}) and grid spectra of ^{12}CO J=3 $\rightarrow$ 2 Emission in the velocity range: 20 -60 km s^{-1}.

Because there is an absorption feature at $\sim$ 45 km s^{-1}, the peak of emission cannot be detected. However, the emission is clearly seen in the blue-shifted wing (v $< v_{LSR}$ = 45 km s^{-1}). Figure 4.4 shows the integrated intensity of ^{12}CO J=3 $\rightarrow$ 2 emission within the velocity interval 20 to 40 km s^{-1} (blue wing). The grid spectra

plot corresponds to the same region, but spectra are shown in the velocity interval 20 - 60 km s^{-1}.

As mentioned before, the CO emission displays an interesting similarity with the line of OH masers (See Fig 4.2 and Appendix B for the identification of masers in this region). We have analyzed several offsets close to maser locations and as well on the location of a few CO clumps and we have calculated the corresponding integrated line intensities (Table 4.1).

Table 4.1: W44E: Line parameters for ^{12}CO J=3 → 2.

Offset (″, ″)	T_A^* (K)	Δv_{FHWM} (km/s)	$\int T\Delta v$ (K km/s)
(-15, 40)	3.63	12	32.09
(-15, 10)	3.09	20	28.29
(-10, 0)	2.97	28	41.87
(-10, -15)	2.94	26	41.33
(0, -20)	3.02	20	41.20
(5, -40)	2.64	17	32.05
(0, -50)	2.89	15	32.81
(-30, 0)	2.76	18	32.08
(-35, -25)	2.50	20	34.06

The blue wing, which contains most of the emitting gas, displays a clump of gas at the offset (-10.0″, 0.0″). The clump is also seen in the red wing emission, the line width at this clump exceeds 40 km s^{-1} providing strong evidence for a shock. Following the same procedure outlined in section 3.3 and Appendix A, we calculated the physical parameters of the clump (mass, excitation temperature, column density) for the total emission (including the wings). The results are shown in Table 4.2.

The energetics of the clump can be estimated as for W28, by comparing the gravitational energy with other competing forms of energy (thermal, turbulent, magnetic).

Table 4.2: W44E - Clump parameters

offset (″, ″)	$N_{^{12}CO}$ ($\times 10^{17}$ cm^{-2})	M_{clump} ($M_\odot$)	T_{ex} (^{12}CO) (K)	Angular size (″)	Radius ($\times 10^{15} m$)
(-10, 0)	8.04	4.68	12.81	7.5	2.8

The gravitational energy has a magnitude of the order of 10^{43} erg, greater than the thermal energy ($\sim 10^{42}$ erg). In contrast, the turbulent energy exceeds by three orders of magnitude the gravitational energy ($E_{turb} \sim 10^{46}$ erg), meaning that the gas turbulent motions play an important role and will not permit the collapse of the clump.

Table 4.3: W44E - Energy balance.

offset (″, ″)	$\mid E_{grav} \mid$ ($\times 10^{43}$ erg)	E_{th} ($\times 10^{42}$ erg)	E_{turb} ($\times 10^{46}$ erg)
(-10, 0)	1.23	6.15	3.6

The magnetic field in the (-10″, 0″) clump could be implied from the measurement of the magnetic field in the neighbouring masers, W44 11 (B_{los} = -0.28 mG) and W28 20 (B_{los} = -0.23 mG) (Claussen *et al.*, 1997). The total median magnetic field would be then $\sim$ 0.4 mG and thus the magnetic energy for a clump of size 4.68 $\times$ 10^{15} m is $E_{mag} \sim 10^{46}$ erg. Again, the magnetic energy largely exceeds the gravitational energy by three orders of magnitude, and if the magnetic field has no preferential direction, the magnetic energy will further prevent the collapse.

4.3.2 W44F Region

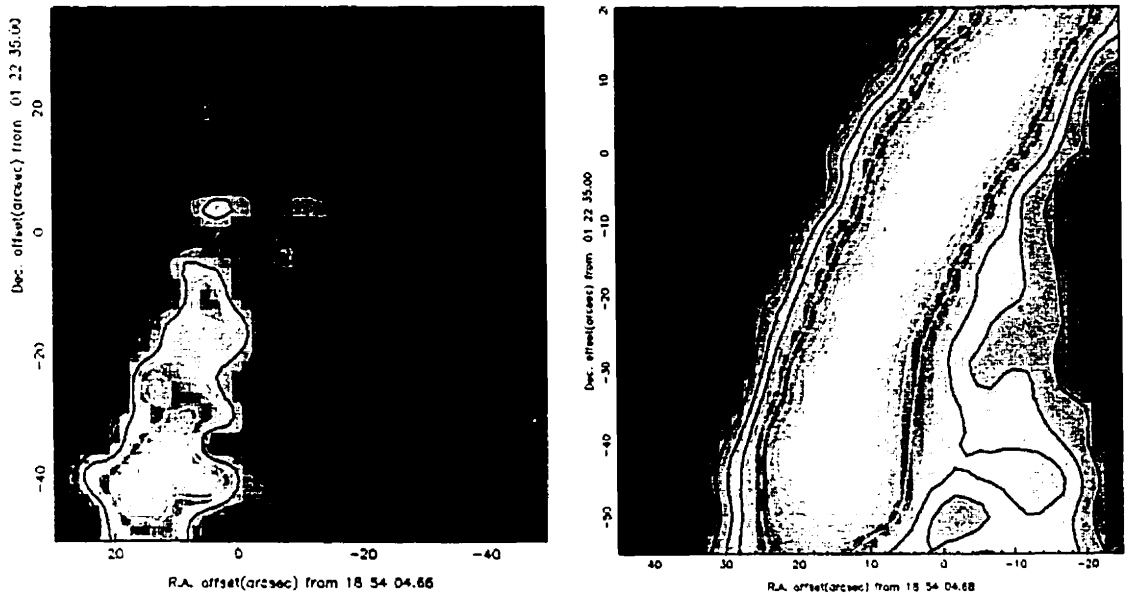

Figure 4.5: W44F. Integrated intensity maps of ^{13}CO J=3 $\rightarrow$ 2 (left panel) and ^{12}CO J=3 $\rightarrow$ 2 emission (right panel).

Figure 4.5 shows the maps of integrated intensity for ^{12}CO J=3 $\rightarrow$ 2 and ^{13}CO J=3 $\rightarrow$ 2 transitions, in the W44F region. In W44F, the gas is distributed within a filament, with interconnected clumpy features. We identify two clumps, one at the offset (15″, -40″), which is also the brightest peak on the map, the other at (0″, 0″). Figure 4.6 contains the corresponding grid spectra for the ^{12}CO J=3 $\rightarrow$ 2 emission in W44F. Using the LTE assumption and the a distance of 2.5 kpc to the remnant, we have calculated the physical parameters of the two clumps. The excitation temperatures have values of $\sim$ 20 K and column densities of the gas, N_{H_2} $\sim$ 10^{21} cm^{-2}. The results are shown in Tables 4.4 and 4.5.

The different energies that can play a role in the stability of the clumps have been

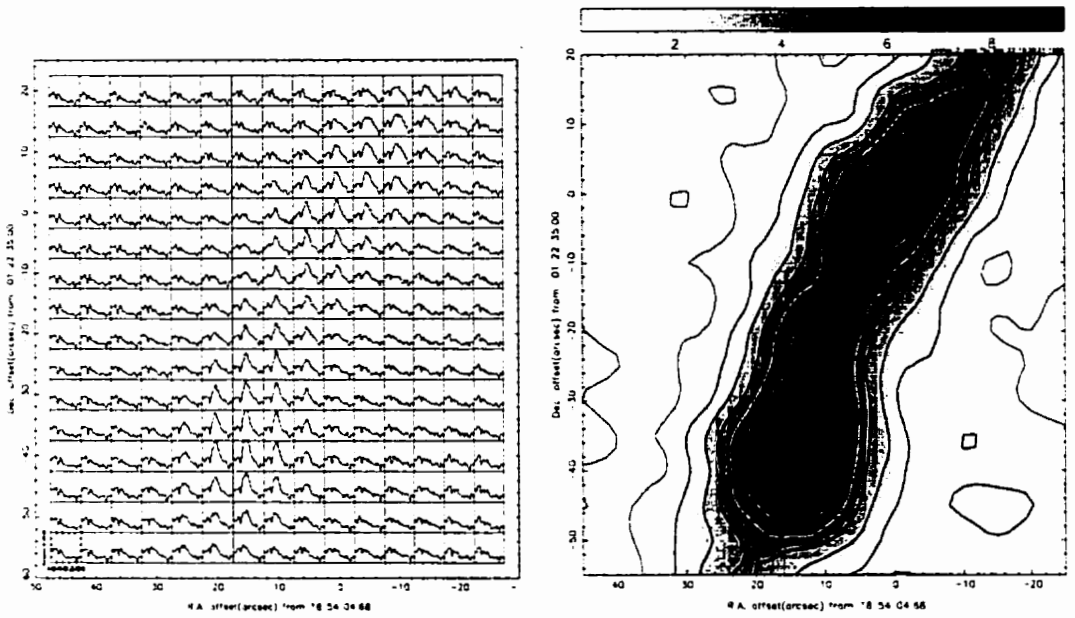

Figure 4.6: W44F. Grid spectra of ^{12}CO J=3 → 2 emission and the two clumps of gas at (15″, -40″) and (0″, 0″)

Table 4.4: W44F - Line parameters.

Offset (″, ″)	T_A^* (^{12}CO) (K)	$\tau_{^{13}CO}$	T_{exc} (^{12}CO) (K)	$N_{^{12}CO}$ ($\times 10^{17}$ cm^{-2})	Common Δv (km s^{-1})
(15, -40)	9	0.1551	23.4	5.57	39 - 50
(0, 0)	7.5	0.0814	20.7	2.63	42 - 55

Table 4.5: W44F - Radii and masses of the clumps.

Offset (″, ″)	Angular size (″)	Radius ($\times 10^{15} m$)	Mass ($M_\odot$)
(15, -40)	5	1.87	1.4
(0, 0)	5	1.87	0.7

calculated. The turbulent energy is $\sim 10^{44}$ erg, which is $\gg$ than the gravitational energy of $\sim 10^{42}$ erg. The conclusion is similar to that for the W28 remnant: the clumps will not have enough gravitational support for collapse.

Table 4.6: W44F -Energy balance

Offset ($''$, $''$)	$\mid E_{grav} \mid$ (10^{42} erg)	E_{th} (10^{42} erg)	E_{turb} (10^{44} erg)
(15, -40)	1.65	3.36	2.24
(0, 0)	0.414	1.48	1.12

There is no direct measurement of the magnetic field for the (15$''$, -40$''$) offset. For (0$''$, 0$''$) the magnetic field could be implied from the neighboring maser, W44 24: B_{los}= -0.12mG. With a mean value 2× B_{los} and for a radius of 1.87 × 10^{15} m, the magnetic energy is $E_{mag} \sim 10^{44}$ erg. The magnetic energy exceeds the gravitational energy by two orders of magnitude and so, on the assumption that the magnetic field has no particular orientation, magnetic energy will prevent the clump from collapsing.

4.4 W44F - Results for Other Molecules

Several species have been investigated for their emission at the offset (20$''$, -180$''$), with respect to the center of the CO map. The new additional information from these detections is that the high dense gas which is traced by these molecules is seen to be shocked.

CH_3OH ($J = 5 \rightarrow 4$) has not been detected, probably its emission being very

Table 4.7: W44F: Line parameters for other molecules. Offset (20″, -180″).

Molecule	Transition	Frequency (GHz)	T_A^* (K)	Δv_{FHWM} (km/s)	$\int T\Delta v$ (K km/s)
CH_3OH	$J = 5 \rightarrow 4$	241.806	-	-	-
HCN	$J = 4 \rightarrow 3$	354.505	0.255	25	5.53
HNC	$J = 4 \rightarrow 3$	362.630	0.045	20	0.54
^{12}CO	$J = 3 \rightarrow 2$	345.795	9.221	30	168.28
^{13}CO	$J = 3 \rightarrow 2$	330.587	1.018	5	8.42

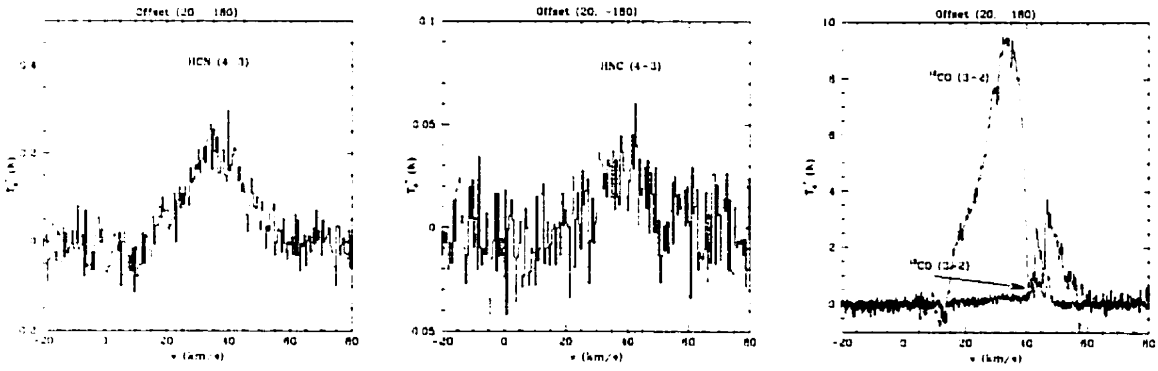

Figure 4.7: W44F. Spectra of several molecules at offset (20″, -180″).

weak, under the noise level (0.05 K). HCN ($J = 4 \rightarrow 3$) emission has been observed, with a relatively broad width, $\sim$ 35 km s^{-1} (FHWM). Very faint HNC ($J = 4 \rightarrow 3$) emission is detected, but still broad, $\sim$ 25 km s^{-1} (FHWM). For comparison, both ^{12}CO J=3 $\rightarrow$ 2 and ^{13}CO J=3 $\rightarrow$ 2 emission were shown together with the other molecular transitions. The absorption feature at 45 km s^{-1} is less evident for species other than CO, but it seems to appear in the HNC spectrum, too.

4.5 W44F -Results for Shocked H_2

Near infrared observations have been obtained for two fields in the W44F region. The BEAR field is 23″ in diameter. For locations of BEAR fields within the CO emission maps, see Figure 4.2.

W44F-1 Region

The W44F-1 region is centered on the coordinates $\alpha(1950) = 18^h\ 54^m\ 05^s.7$, $\delta(1950) = 01°\ 21'\ 50''.00$. We used the K′ filter for observation, with a frequency band: 4308.54 to 5026.63 cm^{-1} (1.98 to 2.32 μm), and a velocity resolution of 12.54 km s^{-1}. The frequency range allowed us to search for both v=1-0 S(1) and Brγ transitions.

Neither H_2 v=1-0 S(1) nor Brγ emission could be detected in the W44F-1 field, meaning that they were either masked by the OH absorption from the Earth atmosphere, either below the noise level ($< 10^{-18}$ W cm^{-2} μ m^{-1}) or absent. We have therefore derived only the upper limits for the H_2 and Brγ line fluxes :

$F_{H_2} \leq 1 \times 10^{-4}$ erg cm^{-2} s^{-1} sr^{-1}, and

$F_{Br_\gamma} \leq 1 \times 10^{-4}$ erg cm^{-2} s^{-1} sr^{-1}.

W44F-4 Region

W44F-4 region is centered on $\alpha(1950) = 18^h\ 54^m\ 06^s.40$, $\delta(1950) = 01°\ 19'\ 29''.00$. The observations have been made with the narrow band filter, centered on v=1-0 S(1) emission and within the frequency range 4657.57 to 4783.45 cm^{-1} (or equivalent in wavelength, from 2.09 to 2.14 μ m).

H_2 emission detected in W44F-4 is weak, but it may well be caused by extinction (Figure 4.8). The strong self-absorption at 45 km s^{-1} implies a large gas (and dust) column density in this line of sight. The emission is faint and patchy, distributed

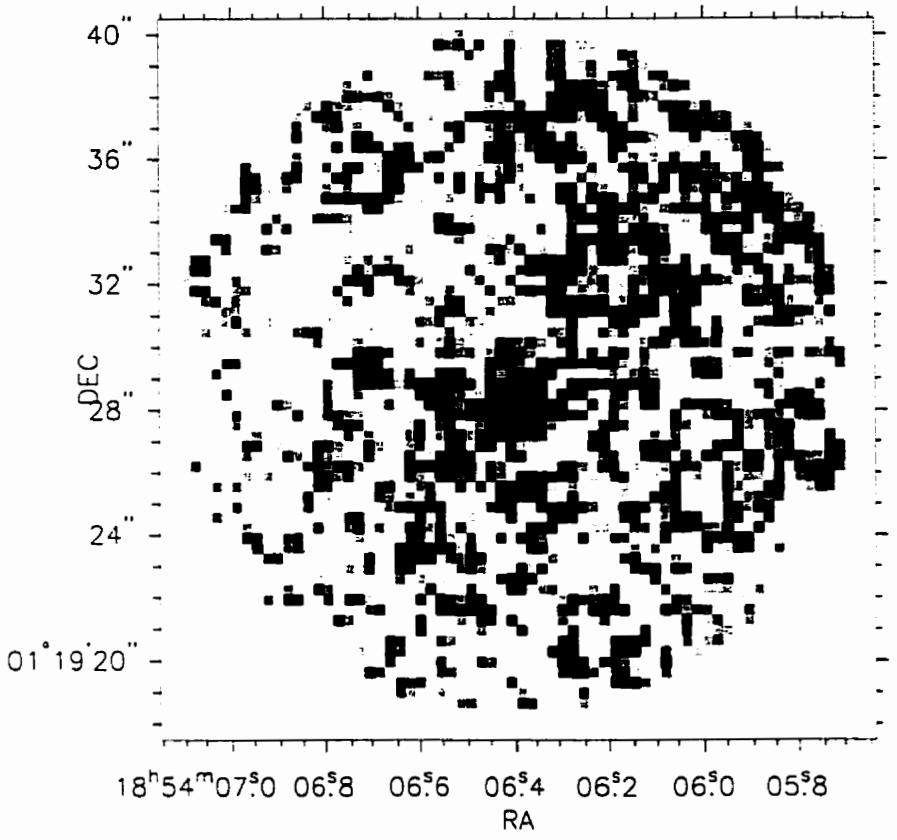

Figure 4.8: Shocked H_2 gas in W44F-4 region, within the BEAR field (23″).

over the entire W44F–4 field, extending in velocity from 33 km s^{-1} to 47 km s^{-1}. There is a continuum emission, identified with a field star, detected in the north-east, at $\alpha(1950) = 18^h\ 54^m\ 06^s.7$; $\delta(1950) = 01°\ 19'\ 36''$.

Figure 4.9 shows a comparison between the H_2 v=1-0 S(1) line and the ^{12}CO J=3 $\rightarrow$ 2 transition at the corresponding offset. The H_2 emission line has a width of $\sim$ 40 km s^{-1} (FHWM), and the CO line has $\sim$ 20 km s^1 (FWHM). We note however that the latter is affected from the self-absorption, around 45 km s^{-1}, making it hard to asses the true shape of the line. There is also a close correspondence between the v_{LSR} of CO (45 km s^{-1}) and H_2 (40.2 $\pm$ 6.2 km s^{-1}) on one side, and the velocities

of masers, on the other side (ranging from 43.67 to 46.91 km s^{-1}). The line flux for the entire field (23″), uncorrected for extinction, is $F_{H_2} \sim 2.5 \times 10^{-3}$ erg cm^{-2} s^{-1} sr^{-1}.

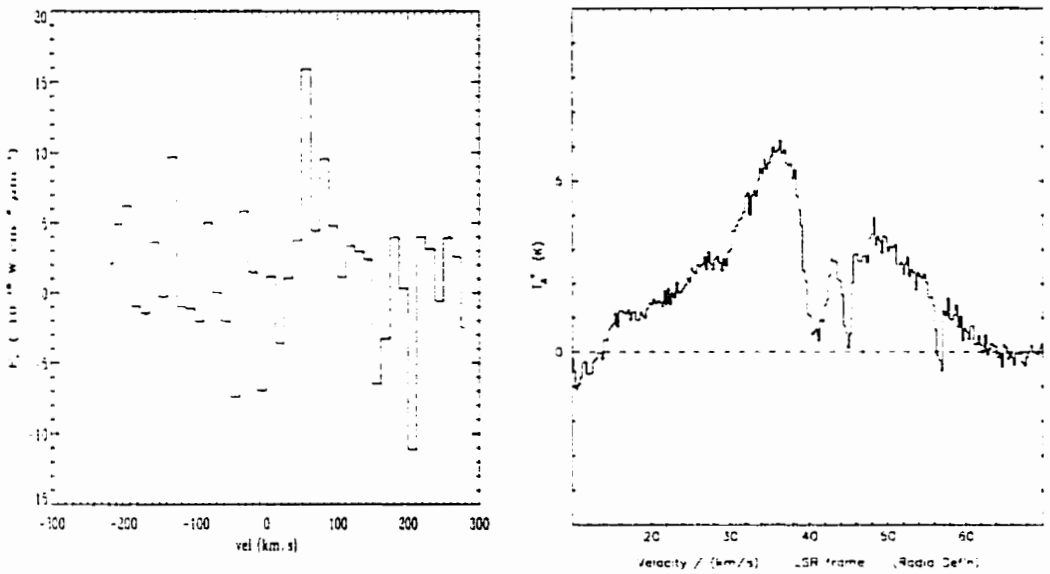

Figure 4.9: H_2 line flux for W44F-4 field (left panel) compared with CO (right panel) at the same position - offset (30″, -195″).

Chapter 5

The 3C391 Supernova Remnant

5.1 3C391. Introduction

3C391 (known also as G31.9+0.0) is another supernova remnant that is likely to be interacting with a molecular cloud, based on the apparent break-out morphology at radio and X-ray wavelengths (Reynolds & Moffet, 1993; Rho & Petre, 1996) and on the detection of OH maser emission (Frail *et al.*, 1996). The remnant is located at $\alpha(1950) = 18^h\ 46^m\ 50^s$ and $\delta(1950) =$ -00° 59′ 00″. The distance is 8.5 kpc, based on H I absorption studies (Caswell *et al.*, 1971; Radhakrishnan *et al.*, 1972), and the angular size 5 arcmin × 7 arcmin. The age of the 3C391 remnant is estimated to be $\sim 10^3$ to 10^4 yr, depending on assumptions made about the environment. A pulsar search was done by Gorham *et al.*, 1996.

The remnant has not been detected at optical wavelengths. Reynolds and Moffet (1993) attribute this to the large absorption along the line of sight, but it should be

noted that the absorption is not significant for [OI] observations (Reach and Rho, 1996)

ROSAT PSPC observations reveal centrally concentrated X-ray emission inside the radio shell (Rho and Petre, 1996). There is a positional asymmetry in both radio and X-ray emission, the northwestern part having a strong radio shell and weak central X-ray emission, while in contrast, the southeastern part displays a strong X-ray emission and weak radio emission. The interpretation of this behavior is one of a "break-out" morphology (Rho and Petre, 1996). It is quite common for shell-type remnants to display one-sided brightness enhancements (which are thought to be caused by encountering density gradients in the interstellar medium) (Caswell, 1987), but break-out morphologies are less common. The break-outs are supposed to occur when the expanding remnant is encountering a steep gradient in the gas density, such as one expected at the edge of a molecular cloud (Tenorio-Tagle *et al.*, 1985; Arthur and Falle, 1991).

Radio continuum and X-ray emission suggest indeed that the remnant's evolution is taking place near a strong density gradient in the surrounding medium. The X-ray emission from 3C391 extends slightly outside the radio shell in SW direction. It peaks in the interior and has a thermal spectrum (Rho & Petre, 1996), characteristic of the "mixed-morphology" remnants (a class of supernova remnants whose nature has been linked to interaction with a strongly inhomogeneous pre-shock ISM) (Rho & Petre, 1998).

For a thermal model, in which PSPC (Rho and Petre, 1995) and IPC (Wang and Steward, 1984) data were used, the best fit yields $N_H = 1.8\ ^{+1.0}_{-0.2} \times 10^{22}\mathrm{cm}^{-2}$ and $\mathrm{kT} = 1.13^{+0.7}_{-0.6}$ keV. According to Wilner *et al.* (1998), the apparent discrepancy

between column density of H I derived from 21 cm observations (Caswell *et al.*) and from X-ray observations (Wang and Seward, 1984; Rho and Petre, 1996) could be explained if the shell part of the remnant lies behind a greater depth of molecular hydrogen than the "break-out" region.

Spectral index and polarization studies were performed by Moffet and Reynolds (1994). The value of the spectral index was found to be 0.55.

CO J= 1 $\rightarrow$ 0 observations bring additional evidence that the remnant is located near the edge of a molecular cloud (Wilner *et al.*, 1998). Also, the CO morphology shows a clear similarity with the "break-out" morphology of the remnant, the CO intensity dropping steeply while the radio continuum intensity is rising steeply across the inner edge of the remnant (Wilner *et al.*, 1998). Therefore, the presence of the molecular cloud could then explain the X-ray morphology, which is weak where the radio shell is bright. Reach and Rho (1999) have identified the molecular cloud as being located at $(l, b, v) = (32.00, 0.00, 98)$, $(\sigma_l, \sigma_b, \sigma_v) = (0.22, 0.09, 3.0)$, with its virial mass estimated to be of the order of $\sim 10^5$ $M_\odot$. Also, CO data support the hypothesis of a progenitor star exploding within a dense molecular cloud and of a shock wave presently believed to be coming out trough the cloud boundary.

CO J = 1 $\rightarrow$ 0 data imply a value for the hydrogen column density of $N_{H_2} \sim 0.8 \times 10^{22}$ cm^{-2} for an integrated intensity of 10 K km s^{-1}, observed at the remnant's center (Wilner *et al.*, 1998). The average volume density is $\sim$ 300 cm^{-3}, a typical value for molecular clouds. No broad line-widths were detected in the CO J= 1$\rightarrow$0 maps, as would have been expected for a shocked region. Although CO J= 1$\rightarrow$0 emission does not reveal any extreme kinematic disturbances, these can be clearly seen in CO J = 3$\rightarrow$ 2 data reported in this present study (see the following sections).

OH emission is present near the remnant as diffuse emission and as masers (compact emission) as well (Frail *et al.*, 1996). The two features detected, which are believed to be (1720 MHz) OH masers, are located in regions where the remnant appears to have broken out into an area of lower ambient density (locations: $\alpha(1950)$ = 18^h 46^m $47^s.63$; $\delta(1950)$ = -01° 01′ 00″.6 and $\alpha(1950)$ = 18^h 47^m $02^s.20$; $\delta(1950)$ = -00° 59′ 01″.0), respectively. The maser velocities, 104.9 and 110.2 km s^{-1} (Frail *et al.* 1996), seem to agree well with systemic velocities implied from CO J =1→0 data, namely 103.9 and 108.2 km s^{-1}, respectively (Wilner *et al.* 1998), and our CO J =3→2 data (105 km s^{-1} for the first maser). Also, the velocities of (1720 MHz) OH features agree well with the H I absorption velocity determined for 3C391 by Radhakrishnan *et al.* (1972).

In addition to the two compact features, a faint, extended OH emission was also detected along the bright NW continuum edge of 3C391 (Frail *et al.*, 1996). This gas is seen in the velocity interval extending from 95.3 km s^{-1} to 98.5 km s^{-1}, and being displaced from masers by about 10 km s^{-1}. Its brightness temperature (< 15 K) and line-width (2–3 km s^{-1}) suggest that it is probably thermal (Frail *et al.*, 1996).

The [OI] (63 μm) line has been detected and the line luminosity inferred for the whole supernova remnant is $\sim 10^3$ $L_\odot$ = 4 × 10^{36} erg s^{-1}. This value is in very good agreement with the shock model of the line. Bright lines, 1.4 × 10^{-3} erg cm^{-2} sr^{-1}, were detected at several positions near the edge of the supernova remnant and less bright in the interior (Reach and Rho, 1996). The [OI] enhancement at the edges of the remnant suggests that the emission is originating from the shocked gas. Also, the continuum brightness is well correlated with the [OI] line brightness (Reach and Rho, 1996).

Based on the comparison of their data with theoretical models that predict the [OI] line brightness, Reach and Rho (1996) suggest a pre-shock density > 10^3 cm^{-3} and ram pressures of the order of 10^{-7} dyne cm^{-2}, as predicted for supernova blast waves interacting with a molecular cloud. Although the spectral resolution for the [OI] observations was poor, Reach and Rho (1996) were able to find a velocity shift of the line of about 400 km s^{-1} between the two places where they made the detection. This velocity difference is similar to the velocity shifts from newly formed radiative shock fronts, which are faster than the shocks in molecular clumps.

5.2 3C391:mol Region. Previous molecular studies

Recent high resolution data have located a dense, shocked molecular clump associated with one of the (1720 MHz) OH masers (located at $\alpha(1950) = 18^h\ 46^m\ 47^s.63$; $\delta(1950)$ = -01° 01′ 00″.6). The infrared observations (Reach and Rho, 1998) imply that the clump has higher density ($n_0 \sim 10^4$ - 10^5 cm^{-3}) than those present in W44 and W28, and similar to IC443. Because "3C391:mol" contains a shock-excited maser and shows a peak in [OI] 63 μm emission, it is believed that this is a region where the SN blast-wave had a significant impact on the molecular gas. Viewing the proximity of the maser and presumably the existence of shocks, it has been suggested that this region could be a possible site for triggered star formation.

ISO observations have been done, using the Long-Wavelength Spectrometer (LWS), with an aperture of 80″ (Reach and Rho, 1996) in "3C391:BML" (or "3C391:mol") region. This region was centered on $\alpha(1950) = 18^h\ 46^m\ 47^s.1$, $\delta(1950)$ = -01° 00′

51″(epoch 1950). The authors reported the first detection of far-infrared H_2O, OH, and CO lines in supernova remnants. There is a strong indication that those lines were detected from shock-excited gas in the remnant (valid for W28 and W44, too).

The warm H_2O in 3C391:mol is believed to be produced by shock-enhanced chemistry. The observed excitation of H_2O and OH ($T_{upper} < 400$ K) (Reach and Rho, 1998) implies that the temperature is not high enough to overcome the barrier of OH conversion into H_2O. However, more H_2O than OH is observed, which means that at some point the gas was hot enough to sustain the conversion. The fact that still high enough OH abundance is observed (only 15 times less than that of H_2O) is at odds with C-shock models, in which almost all of OH is converted in H_2O. However, this might be explained if by some mean the H_2O abundance was underestimated (beam dilution), or if the observed lines of OH and H_2O come in fact from different types of shocks, from regions of different pre-shock densities (Reach and Rho, 1998). Wardle *et al.*(1998) suggested an alternative model in which H_2O is dissociated by the soft X-rays emitted from within the interior of the remnant, producing OH in small regions ($\sim 10^{15}$ cm) where $T_K \sim 100 - 200$ K. This also explains why the OH emission is seen coming from relatively narrow regions in the remnants.

Shocked-accelerated species, such as CS, CO, HCO^+ have been detected (Reach and Rho, 1998), together with bright ionic lines of [O III] and [N III], which are expected only from dissociative shocks. The authors conclude that it must be a range of dissociative shocks in their beam.

Using IRAM 30m telescope, Reach and Rho (1999) have extended their search in the same region of the remnant ('3C391:mol'), for other molecules: ^{12}CO (J =2→1), HCO^+ (J =1→0), CS (J =2→1), CS (J =3→2), CS (J = 5→4). The investigated

region is centered on $\alpha(1950) = 18^h\ 46^m\ 50^s$, $\delta(1950) = -01°\ 00'\ 00''$ (epoch 1950). The narrow lines ($\sim$ 2 km s^{-1}) for the quiescent gas have been interpreted by the authors as signatures of pre-shocked gas. The broad lines ($\sim$ 20 km s^{-1}) in the shocked region are believed to originate in the post-shocked gas, either smoothly accelerated or dissociated and reformed behind the shock.

The shape of the spectral lines changes abruptly in the shocked clump. LTE analysis of ^{12}CO (J =2→1) gives a brightness temperature: $T_k > 50$ K. Thus the shocked clump is significantly more hotter and denser than the densest clumps in the parent cloud. The pressure inferred from CO models is twice as much as the pressure in the blast wave. The authors advance two possible explanations. One explanation suggests that a blast wave hits a high density structure, as the molecular cloud, and the shock splits into reflected and transmitted shocks. In this way, the pressure is enhanced several times in a plane-parallel, uniform density model. However, if we assume that 3C391 remnant is adiabatic, this model can yield pressures much higher than observed. The second explanation suggests that the pressure could increase through gravitational binding of the clumps after compression by the shock. If true, this could be evidence for triggered star formation.

The search for signs of triggered star formation was also one of our main aims in this study, for which we have made use of molecular line and near-infrared observations (see the following sections), concentrating on this specific region ("3C391:mol").

Models of shocks with velocities ranging between 10 - 50 km s^{-1} and for a pre-shock density of 10^4 - 10^5 can yield the observed line brightness of ^{12}CO (J =2→1). This range of shock velocities is near the transition between dissociative (J) and non-dissociative (C) shocks.

For the following analysis, we preserved the same notations as Reach and Rho (1996). The "3C391:mol" region analyzed in this present study has the same center as the "3C391:BML" / "3C391:mol" region from Reach and Rho (1996). However, the resolutions of the present observations are superior: the LWS beam-size was 80″ the JCMT beam-size (for CO spectral data) was 13″ and the BEAR observations have subarcsecond resolution over a 23″ diameter field.

5.3 3C391:mol Observing Fields.

Figure 5.1. extending 1 arcmin, shows a superposition of JCMT and CFHT (BEAR) observations that we used in this study, in connection with the position of the OH maser. The ^{12}CO J=3 $\rightarrow$ 2 and ^{13}CO J=3 $\rightarrow$ 2 maps are drawn corresponding to their location and size, and are shown as rectangles (see Chapter 2 for details of observations). The near-IR (BEAR) field, shown as a circle 23″ in diameter, is centered on a (1720 MHz)OH maser, with coordinates: $\alpha(1950) = 18^h\ 46^m\ 47^s.63$; $\delta(1950)$ = -01° 01′ 00″.6 (Frail *et al.* 1996).

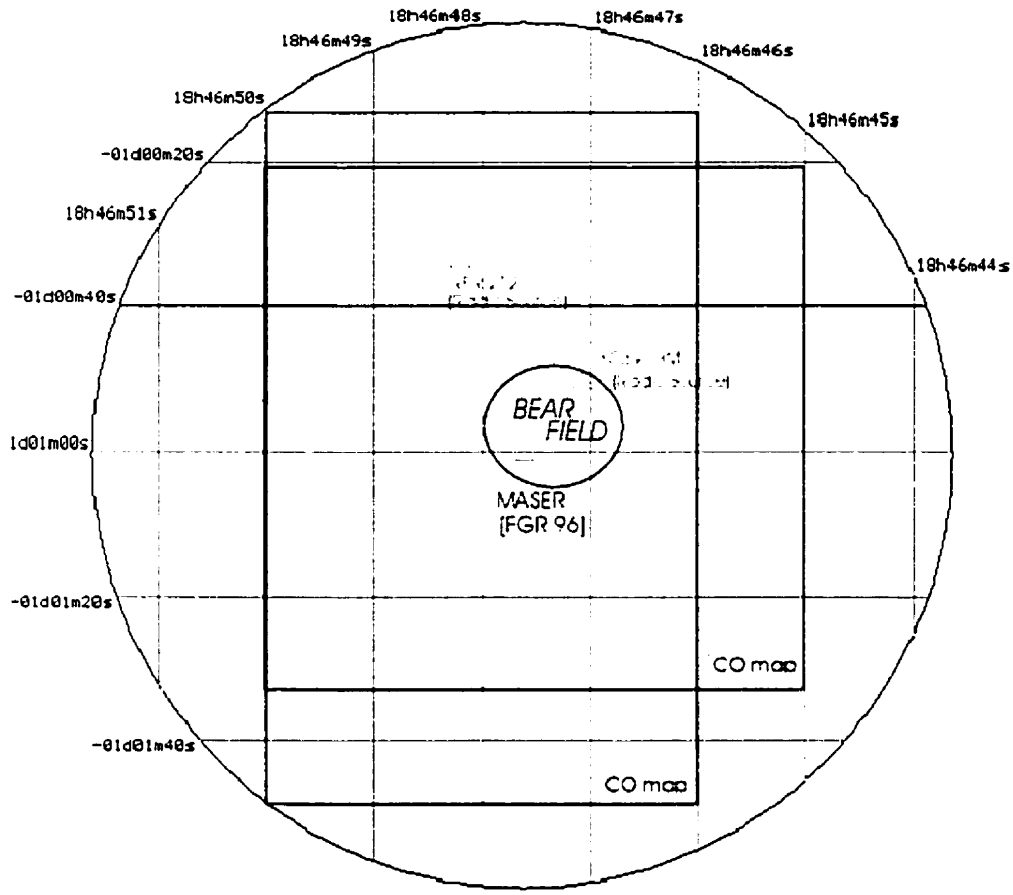

Figure 5.1: (1720 MHz)OH maser in the 3C391-1 region.

5.4 3C391:mol - Results for CO Gas

We obtained a map in ^{12}CO J=3 $\rightarrow$ 2 emission of the 3C391:mol region, centered on coordinates $\alpha(1950) = 18^h\ 46^m\ 47^s.68$, $\delta(1950) = -01°\ 00'\ 59''.98$), therefore coincident with the position of the (1720MHz)OH maser. The map extends in α offsets from 40″ to -40″ and in δ offsets from 40″ to -40″. The ^{13}CO J=3 $\rightarrow$ 2 emission map has the same center and extends in α offsets from 35″ to -25″, and δ offsets from 45″ to -45″.

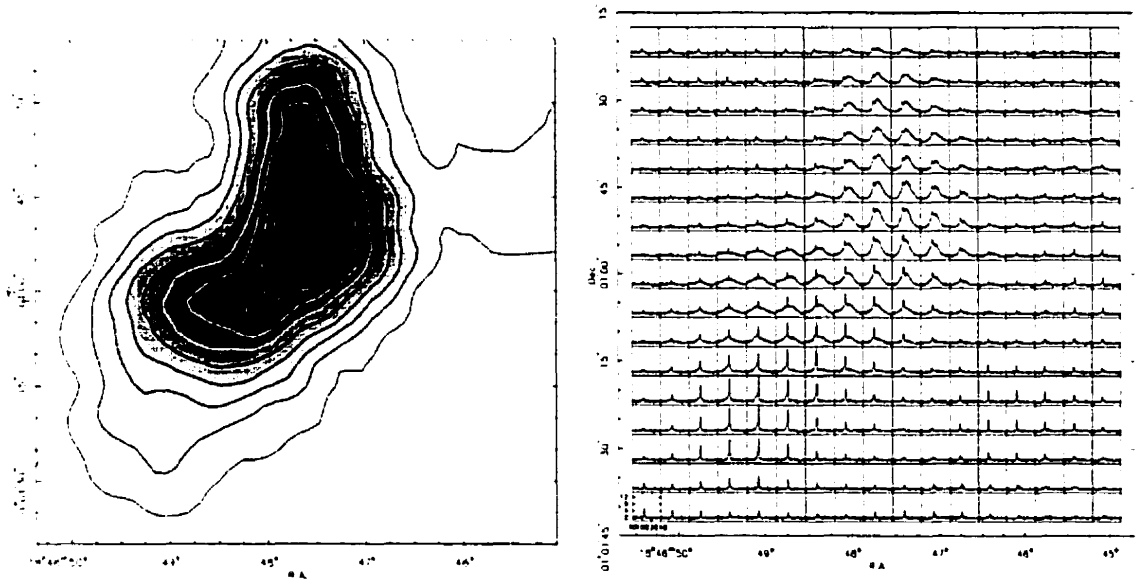

Figure 5.2: 3C391:mol. Grey-map and grid spectra of ^{12}CO J=3 $\rightarrow$ 2 Emission.

Figure 5.2 shows an integrated intensity map of ^{12}CO J=3 $\rightarrow$ 2 emission (left panel) and a grid spectra (right panel), within the velocity interval 80 - 140 km s^{-1}. The 3C391:mol region has one central clump in CO, at offset (-5″, 10″), which corresponds to the position of the intensity maximum in the grey scale map. The broad emission lines ($\sim$ 20 km s^{-1} in FWHM for ^{12}CO J=3 $\rightarrow$ 2) are a clear sign of

shocked gas (see also the last panels on Figures 7.4 and 5.5). It is also noteworthy that the CO clump is coincident with the position of the OH maser shown in Figure 5.1.

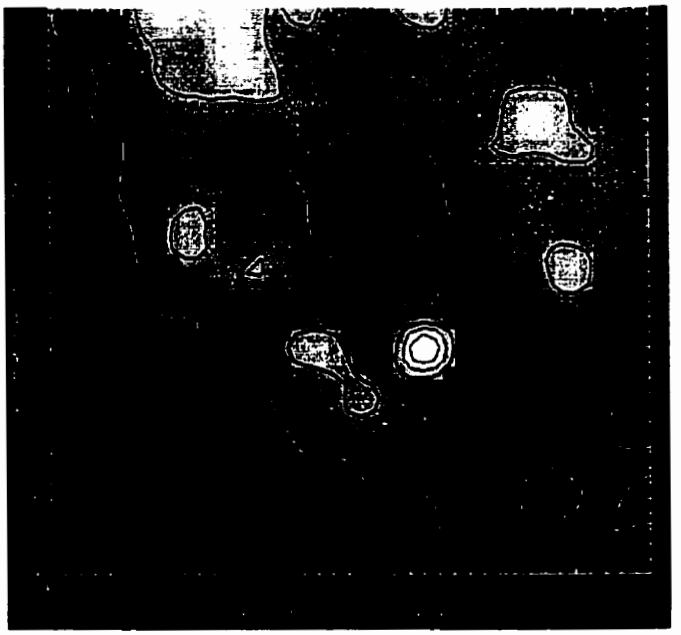

Figure 5.3: Separate feature extending in velocity from 78 to 81 km s^{-1}

We have used the LTE analysis (derived in Appendix A) for the broad line region in the ^{12}CO J=3 $\rightarrow$ 2 emission. The measured antenna temperature as well as the results for the optical depth, excitation temperature and column density of ^{12}CO corresponding to the (-5″, 10″) offset are shown in Table 5.1.

Table 5.1: 3C391:mol - Line parameters.

Field	Offset (″, ″)	T_A^* (^{12}CO) (K)	$\tau_{^{13}CO}$	T_{ex} (^{12}CO) (K)	$N_{^{12}CO}$ ($\times 10^{17}$ cm^{-2})
3C391:mol	(-5, 10)	11.4	0.025	33.8	2.53

Table 5.2: Radius and mass for the 3C391:mol clump.

Offset (", ")	Angular size (")	Radius ($\times 10^{15} m$)	Mass ($M_\odot$)
(-5, 10)	7.5	9.53	17

Knowing the relative abundance of ^{12}CO with respect to H_2, $N_{H_2} \simeq 10^4 \cdot N_{^{12}CO}$, the column density of H_2 is of the order $\sim 10^{21}$ cm^{-2}. The mass of the clump has been calculated in the assumption that 3C391 is at a distance of 8.5 kpc. ^{12}CO J=3 $\rightarrow$ 2 emission is broader in velocity extent that the ^{13}CO J=3 $\rightarrow$ 2 emission. The optically thick region (where both emissions are present) is in this case 95 - 125 km s^{-1}.

The energetics of the clump have been investigated in order to determine the gravitational stability of the clump. Contributing energies are, as before, the gravitational energy and the thermal, turbulent and magnetic energies. The results are shown in Table 5.3.

Table 5.3: 3C391:mol - Energy balance.

Offset (", ")	E_{grav} ($\times 10^{43} erg$)	E_{th} ($\times 10^{42} erg$)	E_{turb} ($\times 10^{46} erg$)
(-5, 10)	4.79	5.9	3.8

The turbulent motions are much stronger than the gravitational energy ($E_{turb} \sim 10^{46} erg \gg E_{grav} \sim 10^{43} erg$), so the clump could not collapse. By assuming that the magnetic field is randomly orientated, its magnetic energy could further prevent the collapse. As we have seen, the magnetic field could be quite important. Although

there are no direct measurements of $\vec{B}$ in 3C391, we can estimate the magnetic strength around the OH maser to be $\sim$ 0.1 mG, comparable with the other magnetic strengths around masers in the other two supernova remnants (W28 and W44). The magnetic energy, calculated for the a 5.93 $\times$ 10^{15} m clump could be as high as $\sim$ 10^{46} erg, three orders of magnitude greater than the gravitational energy.

5.5 3C391:mol - Results for Other Molecules

Observations of different molecular species which trace the high-density gas ($n_0 \sim 10^6$ cm^{-3}), have been done in the frequency range 218 - 363 GHz, for the offsets: (-5″, 10″) and (25″, -25″), with respect to the center of the CO map.

Different line parameters have been calculated, and the broadness of the lines has been investigated. The results are summarized in Figures 5.4 and 5.5 and Tables 5.4 and 5.5.

Offset (-5″, 10″):

Table 5.4: 3C391:mol - Line parameters for other molecules. Offset (-5″, 10″).

Molecule	Transition	Frequency (GHz)	T_A^* (K)	Δv_{FHWM} (km/s)	$\int T \Delta v$ (K km/s)
H_2CO	$3_{03} - 2_{02}$	218.222	-	-	-
CH_3OH	$J = 5 \rightarrow 4$	241.806	-	-	-
CS	$J = 7 \rightarrow 6$	342.883	0.25	15	2.41
HCN	$J = 4 \rightarrow 3$	354.505	0.5	23	8.04
HCO^+	$J = 4 \rightarrow 3$	356.734	0.8	18	10.41
HNC	$J = 4 \rightarrow 3$	362.630	0.07	11	0.49
^{12}CO	$J = 3 \rightarrow 2$	345.795	11.6	15	267.01
^{13}CO	$J = 3 \rightarrow 2$	330.587	1.02	2	5.62

CS, HCO^+, HNC transitions are detected, displaying broad lines, $\Delta v_{FHWM} \sim 11$ km s^{-1} - 23 km s^{-1}. CH_3OH and H_2CO are not detected, or are probably below the noise limit ($\sim$ 0.05 K).

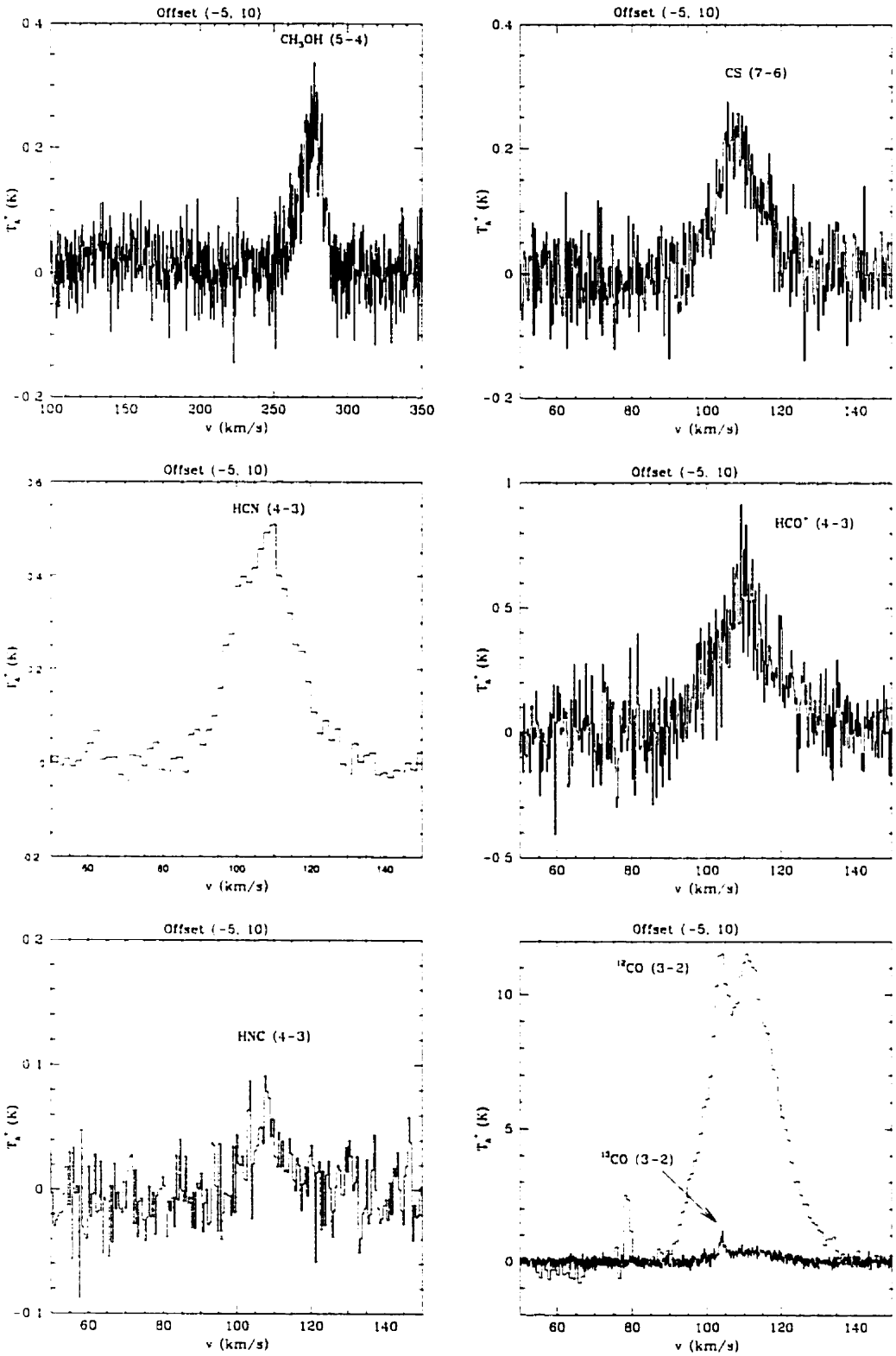

Figure 5.4: 3C391:mol. Spectra of several molecules at offset (-5″, 10″).

Offset (25", -25"):

Table 5.5: 3C391:mol - Line parameters for other molecules. Offset (25", -25").

Molecule	Transition	Frequency (GHz)	T_A^* (K)	Δv_{FHWM} (km/s)	$\int T\Delta v$ (K km/s)
HCO^+	$J = 4 \rightarrow 3$	356.734	0.8	2	1.53
HCN	$J = 4 \rightarrow 3$	354.505	-	-	-
CS	$J = 7 \rightarrow 6$	342.883	-	-	-
^{12}CO	$J = 3 \rightarrow 2$	345.795	13.58	3	48.39
^{13}CO	$J = 3 \rightarrow 2$	330.587	5	2	9.65

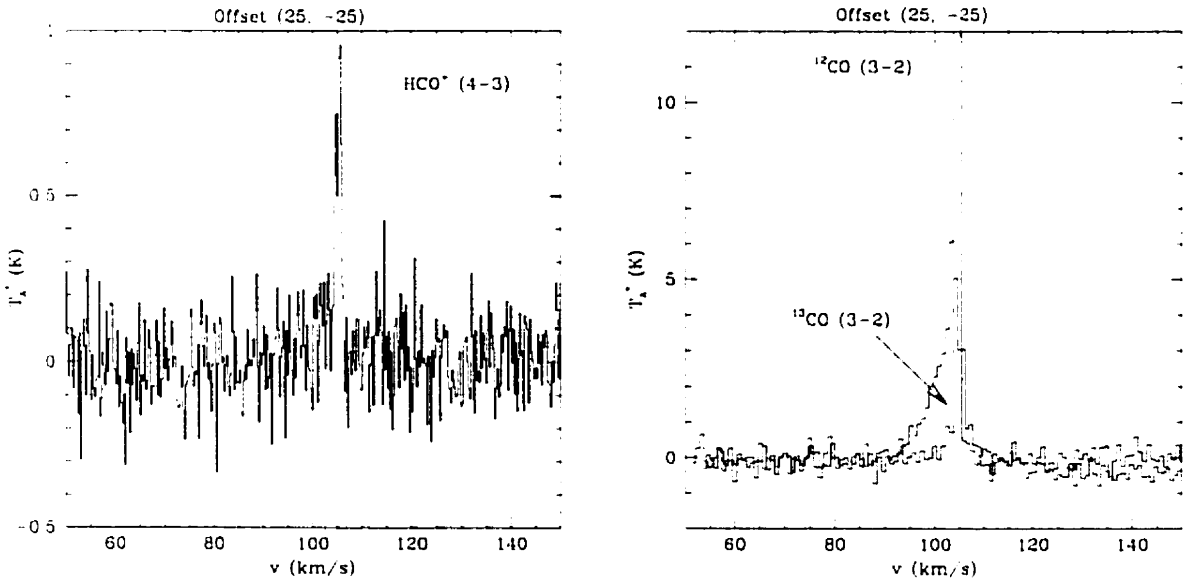

Figure 5.5: 3C391:mol. Spectra of several molecules at offset (25", -25").

At (25", - 25"), strong HCO^+ emission is detected, but the line is narrower than one from offset (- 5", 10"). HCN, CS transitions are not detected. The integrated intensity is calculated in the velocity range common for both transitions: 101 – 106 km s^{-1}.

5.6 3C391:mol - Results for Shocked H_2

Near Infrared observations with BEAR instrument (the BEAR field has a diameter of 23 ″) have been done in the "3C391:mol" region (centered on: $\alpha(1950) = 18^h\ 46^m\ 47^s.4$, $\delta(1950)$ = - 01° 00′ 50″.00), in a search for both H_2 v=1–0 S(1) and Brackett γ emission.

H_2 Emission

For the H_2 shocked gas observations, we used a narrow band filter, centered on the line frequency of v=1-0 S(1) emission, with a frequency range : 4657.57 to 4783.45 cm^{-1} (or equivalent in wavelength, from 2.09 to 2.14 μm).

The H_2 knots are very bright (see Figure 5.6), with peak values of $F_{H_2} \sim 9.2 \times 10^{-3}$ erg cm^{-2} s^{-1} sr^{-1} ($\sim$ 10 times greater than in W28F-1 region). The total H_2 emission has a broad line, $\Delta v_{FHWM} > 50$ km s^{-1}. Figure 5.7 shows for comparison, the shocked H_2 emission line in the entire BEAR field (23 ″) and the corresponding CO emission line, identified in the CO map at the offset (-5″, 10″). The peak of H_2 emission occurs at a similar velocity as the peak CO emission at the same location: v_{LSR} (H_2) = 114.65 km s^{-1} compared v_{LSR} (CO)= 105.0 km s^{-1}. The two rest velocities agree very well, if we take into account the BEAR velocity resolution of 12 km s^{-1}. Moreover, the OH maser in the field has a velocity of 104.9 km s^{-1}.

The flux line intensity at the offset (-5″,10″), uncorrected for extinction is 1 × 10^{-3} erg s^{-1} cm^{-2} sr^{-1}. Four small regions (radius = 1 ″) - labelled here as A, B, C and D - have been chosen from the entire BEAR field, and their individual spectra have been analyzed with the special BEAR data reduction package. Figure 5.8 presents the lines for the four spectra. It can be seen that the emission lines vary in shape and strength, although v_{LSR} doesn't show any major shift.

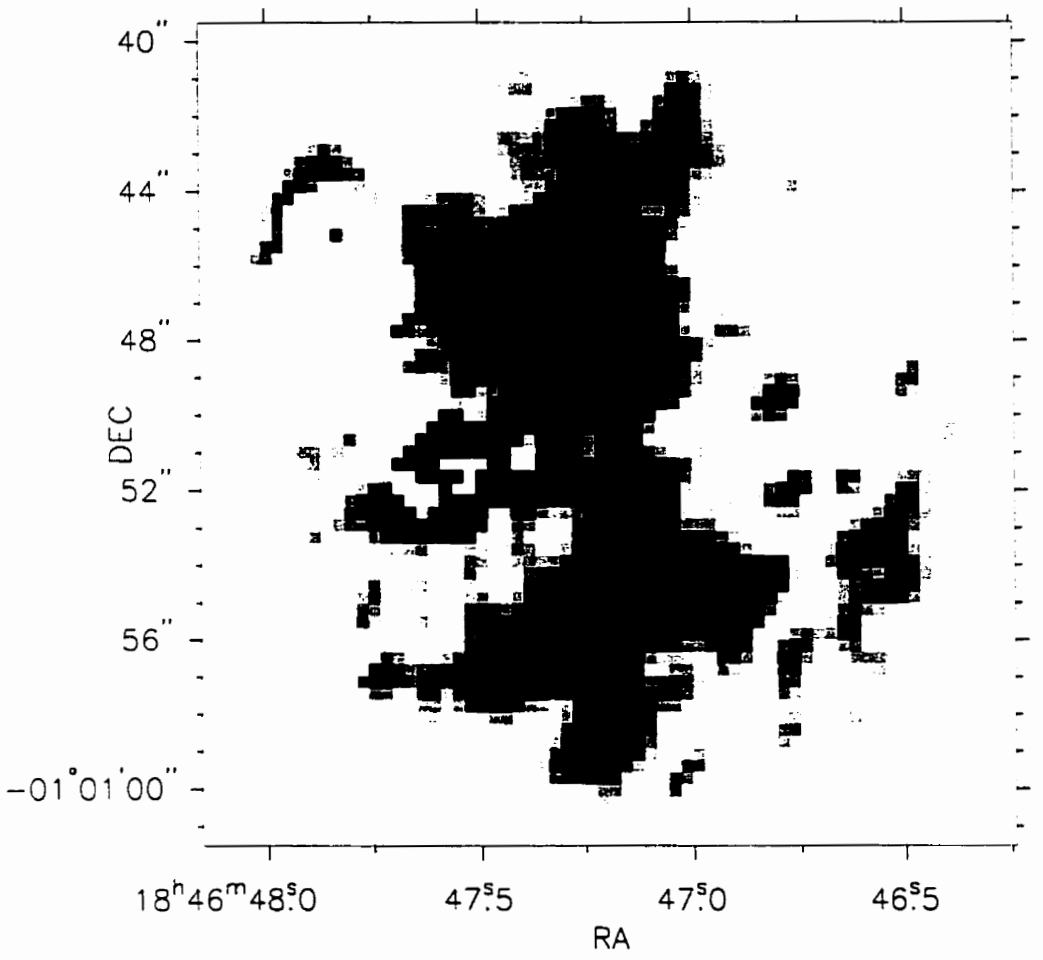

Figure 5.6: Total H_2 shocked emission in 3C391:mol region (within a 23″ beam)

The morphology of the shocked gas has also been investigated. A field star (which appears as continuum emission in the BEAR field) is identified at $\alpha(1950) = 18^h\ 46^m\ 47^s.5$; $\delta(1950)$ = -01° 00′ 50″. A feature that could possibly be a bow shock is seen at $\alpha(1950) = 18^h\ 46^m\ 47^s.8$; $\delta(1950$ = -01° 00′ 57″. Bright H_2 emission extends over the velocity range: 107 - 133 km s^{-1}. The morphology of the gas is changing rapidly with velocity. A central emission is seen extending from north to south, more enhanced in the northern part of the field. At 132 km s^{-1} three distinct features can

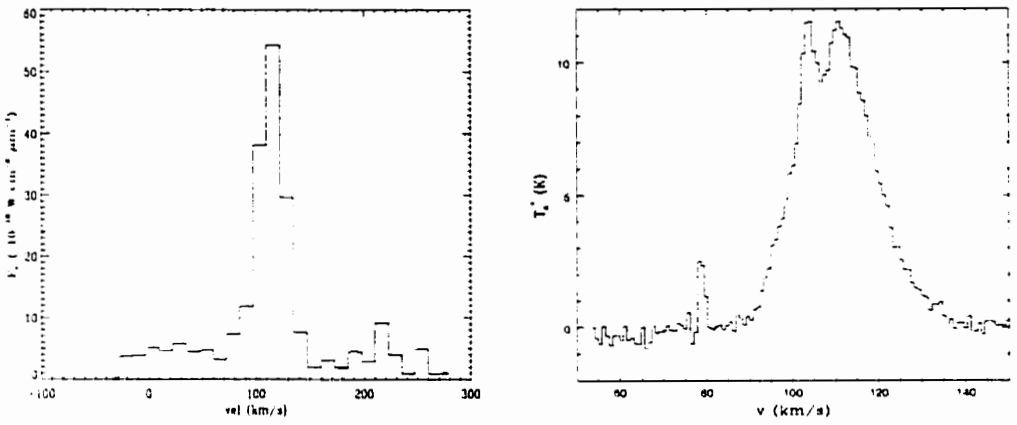

Figure 5.7: H_2 Line flux for 3C391:mol field (left panel) compared with CO spectrum (right panel) at the same position, i.e (-5", 10").

be seen, possibly clumps of shocked gas (see Fig. 5.9).

Brackett γ emission

A search for Brackett γ emission has been done in the same field, with the narrow band filter, centered on 2.16 μm (Brγ line). The frequency range of BEAR measurements was 4540.74 to 4666.87 cm^{-1} (or, equivalent in wavelength, from 2.14 to 2.20 μm).

No Brγ is detected for the BEAR field in the 3C391:mol region. Therefore we can derive only an upper limit for the flux line intensity: $F_{Br\gamma} \leq 10^{-4}$ erg cm^{-2} s^{-1} sr^{-1}.

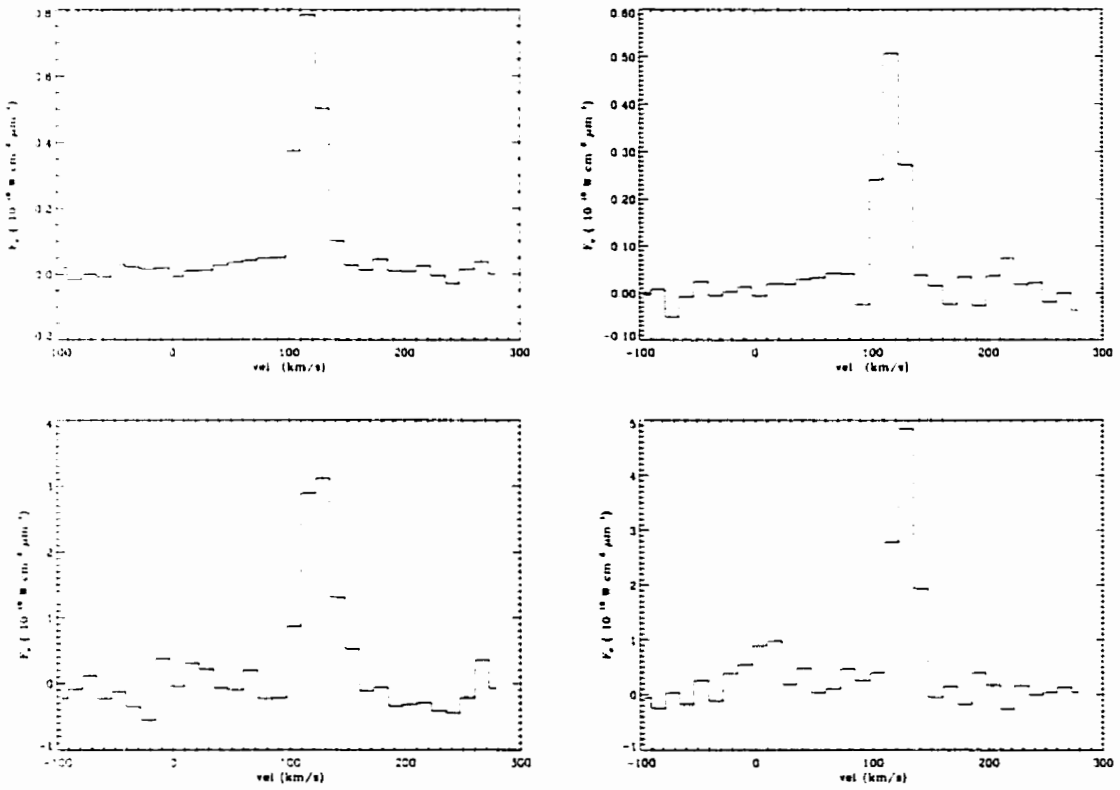

Figure 5.8: 3C391. Line fluxes in regions (from left top to bottom right): A, B, C, D.

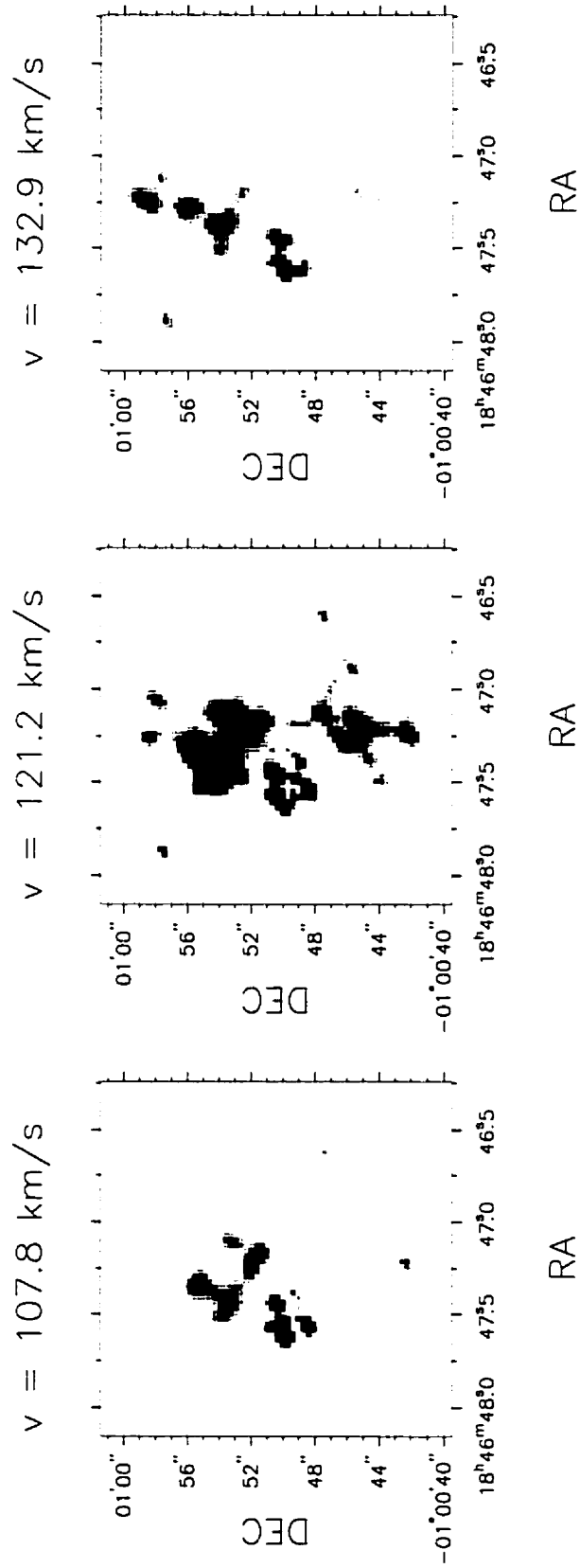

Figure 5.9: Morphology of the H_2 shocked gas for different velocity channels in 3C391:mol

Chapter 6

Discussion and Conclusions

We have studied a few particular examples of interaction between supernova remnants and their environmental molecular clouds, with the aim of determining the nature of the supernova shocks and the effect that those have on the ambient medium. We analized several clumps of gas located near the regions of evident supernova remnant /molecular cloud interaction and assesed their stability against collapse. The main finding of our work is that in all clumps the gas is so heavily disrupted that the gravitational energy cannot overcome the turbulent motion or magnetic energies. We believe that the present conditions prevent gaseous clumps from collapse, and therefore the conditions for star formation are not met.

6.1 CO Gas and Other Molecules.

The CO J= 3 $\rightarrow$ 2 maps near regions of supernova remnant/ molecular cloud interaction have revealed a multitude of molecular clumps. The clumps are clearly shocked,

since the CO emission lines are extremely broad ($\sim$ 20–40 km s^{-1} in FWHM). More interestingly, some of the CO clumps coincide with previous detected (1720 MHz)OH masers, the latter being themselves a sign of shocks.

Additionally, we found kinematic evidence of shocks from spectral lines of other molecular species. Emission from several molecular species has been detected in the three SNRs, including HCO^+ (J = 4 $\rightarrow$ 3), SiO (J = 8 $\rightarrow$ 7), H_2CO [3_{03} - 2_{02}] and [3_{22} - 2_{21}], HCN (J = 4 $\rightarrow$ 3), HNC (J = 4 $\rightarrow$ 3), CS (J = 7 $\rightarrow$ 6). The interest in studying those species is that, unlike CO gas, they trace the high density gas (n_0 $\sim$ 10^6 cm^{-3}). Their lines are faint but broad ($\sim$ 15–25 km s^{-1} FWHM), bringing evidence that the high density gas within the molecular cloud is also shocked.

It was also found that the maser velocities agree within a few km s^{-1} with v_{LSR} of CO and other observed molecular species, suggesting that indeed the masers are spatially close to the molecular gas.

The CO 3 $\rightarrow$ 2 emission is concentrated in thin filamentary and clumpy structures lying just behind the leading edge of the SNR shock. Assuming LTE (Local Thermal Equilibrium), we have been able to determine the physical parameters of the gas in some of the observed regions within the three supernova remnants. In the W28 supernova remnant, five clumps of gas have been identified, in both ^{12}CO J=3 $\rightarrow$ 2 and ^{13}CO J=3 $\rightarrow$ 2 emission. The excitation temperatures are about 30 K. We have investigated the main contributing types of energies, in order to determine the gravitational stability of the clumps. Both thermal and gravitational energies are of the order of $\sim$ 10^{43} erg. The turbulent energy in W28, implied from the width of the emission lines, is $\sim$ 10^{46} erg, exceeding by three orders of magnitude the gravitational energy. Under these circumstances, the clumps cannot be gravitationally

supported and certainly the collapse is avoided. In the same time, the magnetic energy is believed to be important in the cloud energetics. Although there are no direct measurements of the magnetic fields within the five molecular clumps, the neighboring masers show significant magnetic field strengths ($\sim$ 0.4 mG). Assuming a similar value for the $\vec{B}$ in the molecular gas of the clumps, the magnetic energy would be of the order of $\sim 10^{46}$ erg. This magnetic energy exceeds the gravitational energy by three orders of magnitude, and in the assumption that the magnetic field is randomly oriented, it could further prevent the clumps from collapsing.

In the W44 remnant, a self-absorption feature very close to the peak emission ($\sim$ 45 km s^{-1}) made it difficult to estimate the physical parameters for the entire line. However, since the blue wing contained much of the shocked gas, we have calculated the line parameters only for this region of the spectrum. The excitation temperatures are $\sim$ 20 K and the masses of the clumps are 1.4 and 0.7 $M_{\odot}$. Turbulent and magnetic energies are found to be of the order of $\sim 10^{44}$ erg, which are much greater than the gravitational energy of $\sim 10^{42}$ erg. There is again, no evidence for clump collapse.

Within the 3C391:mol region in the 3C391 remnant we have found only one shocked clump. Again, it coincides with a (1720 MHz) OH maser and their rest velocities agree within 1 km s^{-1}. The excitation temperature is 33.8 K and the mass of the clump is 17 $M_{\odot}$. A study of the energy balance in the clump reveals that here, too, the turbulent energy is much larger than the gravitational energy ($E_{turb} \sim 10^{46}$ erg $\gg E_{grav} \sim 10^{43}$ erg). Based on this, we suggest that the clump in 3C391:mol too will be prevented from collapse.

The fact that in all three systems analized here the clumps are extremely turbu-

lent, leads us to the conclusion that the triggering of star formation is not possible, at least at the present time. It is however possible that such a process will take place in the future, when the free-fall timescale will become much shorter than the characteristic timescale of the turbulence.

6.2 Vibrationally excited H_2.

We have presented the first observations of high resolution, vibrationally excited v=1-0 S(1) H_2 emission (at 2.12 μm) in W28, W44 and 3C391.The H_2 1-0 S(1) emission arises from the shock front and traces the hot, recently shocked material, in contrast with the CO emission, which comes mainly from cooler pre- or post-shock gas. The H_2 lines are resolved in velocity and have line widths of $\sim$ 40 km s^{-1}, similar to those of CO lines. This indicates that the shock speed is quite high. The v_{LSR} of the vibrationally excited H_2 emission agrees well (within a few km s^{-1}) with the velocities of OH masers in the field and with the v_{LSR} of CO.

An interesting result is that the morphology of the shocked H_2 emission follows closely the distribution of OH masers in the field. For example in W28F, we have found a clumpy and filamentary H_2 distribution which follows almost identically the thin line of the previously observed (1720 MHz) OH masers (Frail *et al.*, 1996).

The H_2 emission shows a high degree of small scale clumpiness, similar to H_2 emission in the IC443 supernova remnant. We notice the contrast with the extremely smooth Hα emission observed with HST in the Cygnus Loop (Blair *et al.*, 1999). This is puzzling, because both emissions originate from the hot gas behind the shock and yet, their morphologies are extremely different.

The line shapes and strengths seem to vary over sub-arcsecond angular distances, meaning that the applicability of plane-parallel shocks could be put in doubt and other geometries (*e.g.* mini-bow shocks around clumps) will need to be in the future examined.

The line fluxes of v=1–0 S(1) emission line are typically of the order of $\sim 1.6\times10^{-3}$ erg cm^{-2} s^{-1} sr^{-1}, with the exception of "W44F–1" field, where the H_2 emission was not detected. For this region, we determined an upper limit of $F_{H_2} \leq 10^{-4}$ erg cm^{-2} s^{-1} sr^{-1}. The brightest H_2 emission was detected for the shocked clump in 3C391, $F_{H_2} \sim 9.2 \times 10^{-3}$ erg cm^{-2} s^{-1} sr^{-1}.

We carried out two observations for the Brackett γ emission line, one with the broad K′ filter in "W28F–1" field, the other with a narrow band filter centered on 2.16 μm, in the shocked clump from 3C391. In both observations, the Br_γ line was not detected. Nonetheless, we determined an upper limit for its emission, as: $F_{Br_\gamma} \leq 10^{-4}$ erg cm^{-2} s^{-1} sr^{-1}.

6.3 Shock Models. Comparison with Simulations.

Theoretical models of shocks (Draine *et al.*, 1983; Hollenbach and McKee, 1989) predict that the [OI] line would be produced either in fast ($v_s > 50$ km s^{-1}) dissociative shocks or in slow ($v_s \leq 10$ km s^{-1}) non-dissociative shocks, while the vibration-rotation transitions of H_2 and high–J rotational transitions of CO and H_2O would be produced by moderate ($v_s \sim 40$ km s^{-1}) non-dissociative shocks.

One interest is to compare the observed line intensities of H_2 1 – 0 S(1) transition and the upper limits for the Br_γ emission with existent models of shocks (Hollenbach

and McKee, 1989; Chernhoff, Hollenbach and McKee, 1982; Draine et al, 1983). For the following discussion, we have preserved the original notation of the cited models. Several representative classes are considered: class "A" is a fast dissociative J shock ($v_s \geq 30$ km s^{-1}), classes "B"and "C" represent slow, non-dissociative or partially dissociative J shocks ($v_s \leq 25$ km s^{-1}), class "D" is a slow C shock with low peak temperatures ($T \leq 300$ K) so that neutral-neutral reactions with activation energies are suppressed ($v_s \leq 15$ km s^{-1}), and finally, classes "E", "F" and "G" are moderate to fast C shocks with peak temperatures $T \sim 1000$ -3000 K , near the dissociation limit for H_2 ($v_s \sim 25$ - 40 km s^{-1}).

Table 6.1: Observed versus Model Shock Line Intensities.Theoretical models are from Burton *et al.*, 1990).Observed [OI] emissions for W44 and 3C391 are from Reach and Rho (1996).

	Line Intensity ($erg\ s^{-1}\ cm^{-2}\ sr^{-1}$)		
	H_2 v=1-0 S(1)	Br_γ	[OI] (63 μm)
Models			
A (Fast J)	3.6×10^{-5}	4.0×10^{-5}	3.0×10^{-3}
B (Slow J)	5.3×10^{-4}	$< 1 \times 10^{-10}$	2.1×10^{-7}
C (Slow J)	6.9×10^{-4}	1.2×10^{-14}	2.9×10^{-3}
D (Slow C)	$< 1 \times 10^{-10}$	$< 1 \times 10^{-10}$	2.2×10^{-3}
E (Fast C)	3.6×10^{-3}	$< 1 \times 10^{-10}$	8.2×10^{-5}
F (Fast C)	3.6×10^{-3}	$< 1 \times 10^{-10}$	$\sim 2 \times 10^{-3}$
G (Fast C)	3×10^{-3}	$< 1 \times 10^{-10}$	3×10^{-3}
Observed Flux			
W28F-1 region	1.6×10^{-3}		
W28F-2 region	1×10^{-3}		
3C391:mol	9.2×10^{-3}	$< \times 10^{-4}$	1.4×10^{-3}
W44F-1 region	$< \times 10^{-4}$	$< \times 10^{-4}$	0.3×10^{-3}
W44F-4 region	2.5×10^{-3}		0.3×10^{-3}

Table 6.1 shows a comparison between flux line intensities, predicted by the shock models and our observed values. Also displayed are the observed values for the [OI] flux, whenever they could have been found in the literature. We note that all models predict very low fluxes of Brackett γ emission and therefore, within our limit of detection, we cannot distinguish in this respect among the different types of shocks. However, we can use the contraints predicted for the H_2 v=1-0 S(1) and [OI] lines. It can be seen that class " B" (slow, non-dissociative J shocks) cannot fit the observed [OI] lines, producing a much weaker [OI] line than the observations. Also, classes "A" and " B" (the fast and slow J-type shocks) predict much lower H_2 line intensities ($\sim 10^{-5}$ - 10^{-4} erg cm^{-2} s^{-1} sr^{-1}) than those we observed in the three supernova remnants ($\sim 10^{-3}$ erg cm^{-2} s^{-1} sr^{-1}). A slow C shock (class "D"), although it might explain the observed [OI] emission ($\sim 10^{-3}$ erg cm^{-2} s^{-1} sr^{-1}), it cannot explain the observed v=1-0 S(1) H_2 emission, yielding an extremely low line intensity ($\sim 10^{-10}$ erg cm^{-2} s^{-1} sr^{-1}). Therefore, we can rule out fast J and slow C shocks.

Class "C", a slow partially dissociative J-shock could explain only the H_2 and [OI] lines from the W44F-1 region and not the others. Fast C-shocks (classes "F" and "G") seem to be the most suitable theoretical models that can fit both H_2 and [OI] lines.

We conclude that in those three particular cases of supernova remnant/molecular cloud interaction, the most suitable shock model would be either the fast "C" or the slow "J" -type. This seems to be the case at least for the small regions of the remnants where we have shocked H_2 data. Of course, more data is needed for a complete understanding of the nature of the shocks in these supernova remnants.

Bibliography

[1] Arikawa, Y., Tatematsu, K., Sekimoto, Y and Takahashi, T. 1999, *Star Formation Newsletter*, **No. 82**

[2] Arthur, S. J. and Falle, S. A. E. G. 1991, MNRAS, **251**, 93

[3] Blair, W. P., Sankrit, R., Raymond, J. C., Long, K. S., 1999 AJ, **118**, 942

[4] Burton, M. G., Hollenbach, D. J., Haas, M. R., Erickson, E. F. 1990, ApJ, **355**, 197

[5] Caswell, J. L. *et al.* 1987, in IAU Colloquium 101, *Supernova Remnants and the Interstellar Medium*, edited R. S. Roger and T. L. Landecker (Cambridge University Press, Cambridge), p. 269

[6] Caswell, J. L. *et al.* 1971, A&A, **12**, 271

[7] Chernhoff, D. F., Hollenbach, D. J., McKee, C. F. 1982, ApJ, **259**, 97

[8] Chevalier, R. A. 1977, ApJ, **213**, 52

[9] Clark, D. H., Caswell, J. L. 1976, MNRAS, **174**, 267

[10] Claussen, M. J. *et al.* 1997, ApJ, **489**, 143

[11] Claussen, M. J. Goss, W. M., Frail, D. A., Desai, K. 1999a, ApJ, **522**, 349

[12] Claussen, M. J. Goss, W. M., Frail, D. A., Seta, M. 1999b, AJ, **117**, 1387

[13] Draine, B. T. 1980, ApJ, **241**, 1021

[14] Draine, B. T., Roberge, W. G. & Dalgarno, A. 1983, ApJ, **264**, 485

[15] Elitzur, M. 1976, ApJ, **203**, 124

[16] Elmegreen, B. G., 1977, in Conference Proceedings of the *Massive Molecular Clouds Workshop* , Gregynog, Wales

[17] Elmegreen, B. G., Lada, C. J. 1977, ApJ, **214**, 725

[18] Esposito, J. A., Hunter, S. D, Kanbach, G. Sreekumar, P. 1996, ApJ, **461**, 820

[19] Frail, D. A., Goss, W. M. & Slysh, V. I. 1994, ApJ, **424**, L111

[20] Frail, D. A., Giacani, E. B., Goss, W. M., Dubner, G. 1996a ApJ, **464**, L165

[21] Frail, D. A., Goss, W. M., Reynoso,, E. M., Green, A. J. & Otrupcek, R. 1996b, AJ, **111**, 1651

[22] Frail, D. A. and Mitchell, G. F. 1998, ApJ, **508**, 690

[23] Giacani, E. B *et al.* 1997, apJ, **113**, 1379

[24] Gorham *et al.* 1996, ApJ, **458**, 257

[25] Green, A. J. *et al.* 1975, A&A, **44**, 187

[26] Green, A. J., Frail, D. A., Goss, W. M. & Otrupcek, R. 1997, AJ, **114**, 2058

[27] Goudis, C. 1976, Ap&SS, **45**, 133

[28] Hartl, H. *et al.* 1983, ApJL, **23**, 193

[29] Hollenbach, D. J. and McKee, C. F. 1989, ApJ, **342**, 306

[30] Hollenbach, D. J. 1997, in IAU Symp. 182, *Herbig-Haro Flows and the Birth of Low Mass Stars*, ed. B. Reipurth & C. Bertout (Dordrect: Kluwer), 181

[31] Huang, Y.-L. and Thaddeus, P. 1985, ApJL, **295**, 13

[32] Huang, Y.-L. and Thaddeus, P. 1986, ApJ, **309**, 804

[33] Kaspi, V. M. *et al.* 1993, ApJL, **409**, 57

[34] Kassim, N. E. 1992, AJ, **103**, 943

[35] Kaufman, M. J., Neufeld, D. A 1996a, ApJ, **456**, 250

[36] Kaufman, M. J., Neufeld, D. A 1996b, ApJ, **456**, 611

[37] Klein, R., McKee, C. F. and Collela, P. 1994, ApJ, **420**, 213

[38] Koo, B. C. & Heiles, C. 1995, ApJ, **442**, 679

[39] Langer, W. D. & Penzias, A. A. 1990, ApJ, **357**, 477

[40] Lockett, P., Gauthier, E., Elitzur, M. 1999, ApJ, **511**, 235

[41] Long *et al.* 1991, ApJ, **373**, 567

[42] Lozinskaya, T. A. 1974, SvA, **17**, 603

[43] Maillard, J. P. 1998, private communication

[44] Matsui, Y. and Long, K. S., 1985, in *The Crab Nebula and related supernova remnants*: Proceedings of the Workshop, Fairfax, VA, October 11, 12, 1984 (A86-41101 19-90). Cambridge and New York, Cambridge University Press, p. 211-216; Discussion, p. 217.

[45] McKee, C. F., Chernoff, D. F. & Hollenbach, D. J. 1984, in *Galactic and Extragalactic Infrared Spectroscopy* ed. M.F. Kessler & J.P. Phillips (Dordrecht: Reidel), 103

[46] Milne, D. K. 1979, AuJPh, **32**, 83

[47] Moffett, D. A. & Reynolds, S. P. 1994, ApJ, **425**, 668

[48] Mac Low M., McKee, C. F., Klein, R. I., Stone, J. M., Norman M. 1994, ApJ, **433**, 757

[49] Nadeau, D., Geballe, T. R., Neugerbauer, G. 1982, ApJ, **253**, 154

[50] O'Brien, I. & Drury, L. O. 1996, MNRAS, **280**, 550

[51] Odenwald, S. F. *et al.* 1984, ApJ, **279**, 162

[52] Padman, R. 1992, *SPECX V6.3 User's Manual* (Cambridge: Cavendish Laboratory)

[53] Pastchenko, M. I. & Slysh, V. I. 1974, A&A, **35**, 153

[54] Radhakrishnan *et al.* 1975, ApJS, **24**, 49

[55] Reach, W. M. & Rho, J. 1996, A&A, **315**, L277

[56] Reach, W. M. & Rho, J. 1998, ApJL, **507**, 93

[57] Reach, W. M. & Rho, J. 1999, ApJ, **511**, 836

[58] Reynolds, S. P. & Moffett, D. A. 1993, AJ, **105**, 2226

[59] Rho, J. *et al.* 1994, ApJ, **430**, 757

[60] Rho, J. & Petre, R. 1996, ApJ, **467**, 698

[61] Rho, J. & Petre, R. 1998, ApJ, **503**, L167

[62] Seward, F. D. 1990, ApJS, **73**, 781

[63] Shull, M. J. & Beckwith, S. 1982, Ann. Rev. Astron. Astrophys., **20**, 163

[64] Shelton, R. L. *et al.* 1999, ApJ, **524**, 192

[65] Shull, J. M., *et al.* 1989, ApJ, **346**, 860

[66] Smith, M. D. & Mac Low, M. M. astroph/9703171

[67] Tenorio-Tagle, G. *et al.* 1985, A&A, **145**, 70

[68] Wagner, A. F. & Graff, M. M. 1987, ApJ, **317**, 423

[69] Wang, Z. R. and Seward, F. D. 1984, ApJ, **279**, 705

[70] Wardle, M. 1998, M.N.R.A.S, **298**, 507

[71] Wardle, M., Yusef-Zadeh, F., Geballe, T.R 1998, astro-ph/9804146

[72] Wilner, D. J., Reynolds, S. P. and Moffet, D. A. 1998, AJ, **115**, 247

[73] Wolszczan, A., Cordes, j. M. and Dewey, R. J. 1991, ApJ, **372**, L99

[74] Wootten A. 1977, ApJ, **216**, 440

[75] Wootten A. 1981, ApJ, **245**, 105

Appendix A

Derivation of Physical Parameters

A.1 Optically Thick Equations

The radiation temperature, T_R is given by the relation

$$T_R = \frac{T^*_A}{\eta_b f} \tag{A.1}$$

where η_b is the beam efficiency (for our observations has a value 0.79) and the filling factor f $\sim$ 1.

From Langer & Penzias (1990) we can estimate the ^{12}CO /^{13}CO abundance ratio of $\frac{N_{12CO}}{N_{13CO}} \approx 60.$ and therefore an integrated intensity ratio:

$$\frac{I_{12}}{I_{13}} \cong \frac{1 - e^{-\tau_{12}}}{1 - e^{-\tau_{13}}} = \frac{1 - e^{-60 \times \tau_{13}}}{1 - e^{-\tau_{13}}}, \tag{A.2}$$

assuming the same T_{exc} and approximately the same frequency for the two transitions.

The excitation temperature, T_{exc}, can be found from:

$$T_{exc} = \frac{h\nu/k}{ln[(1 - e^{-\tau})h\nu/kT_R + 1]}. \quad (A.3)$$

The total column density of the molecular gas can be obtained from the integral of the optical depth over the line profile. Under LTE (Local Thermal Equilibrium) conditions, the total column density N is obtained from:

$$N = \frac{3k}{8\pi^3 B\mu^2} \times \frac{e^{hBJ_l(J_l+1)/kT_{ex}}}{J_l + 1} \times \frac{(T_{exc} + hB/3k)}{1 - e^{-h\nu_{ul}/kT_{exc}}} \times \int \tau(v)dv, \quad (A.4)$$

where B is the rotational moment and μ is the electric dipole moment of the molecule, and we assumed that all population levels are characterized by a single excitation temperature T_{exc}. For ^{13}CO molecule, $B = 5.75 \times 10^{10}$ Hz, and $\mu = 0.110$ Debye. Moreover, for the J=3 $\rightarrow$ 2 transition, equation A.4 takes the simplified form:

$$N_{C^{12}O} = 0.809 \times 10^{14} \times (T^{12}_{exc} + 0.92) \times e^{\frac{16.59}{T^{12}_{exc}}} \times \frac{1}{1 - e^{-\frac{16.59}{T^{12}_{exc}}}} \times \int \tau_{12}(v)dv \quad (A.5)$$

where N is expressed in cm^{-2} and v is in $km{\cdot}s^{-1}$.

The mass of the H_2 gas is given by:

$$M_{H_2} = \frac{N_{H_2} \times (2 \times m_H) \times A}{1.98 \times 10^{33}} M_\odot, \quad (A.6)$$

where N_{H_2} is the total H_2 column density, A is the beam area and m_H is the mass of the hydrogen atom. For an angular size r ($''$) and distance d to the source (in kpc), the clump area is given by:

$$A = \pi R^2 = \pi(\frac{r('')}{206265} \times d \times 10^3 \times 3.0856 \times 10^{18})^2(cm^2). \quad (A.7)$$

where R is the radius of the clump.

How accurate the mass of the clump is calculate will depend strongly on the uncertainty in the distance determination. We should note that the distances to the three supernova remnants of this study are not precisely determined, sometimes within uncertainties of one kpc, depending on the method of measurement. Therefore, the estimation of the mass of the clumps in our systems could be affected.

Furthermore, if we are taking into account the fractional helium abundance, the total mass of the clump within the beam is:

$$M = 1.4 \times M_{H_2}. \tag{A.8}$$

Appendix B

OH Masers in W28, W44 and 3C391

The identification of masers has been done using interactively the SIMBAD database, with information based on the reported maser detection by Claussen *et al.* (1997). We have selected only the maser emission coincident with our CO maps. The coordinates, LSR velocities and the magnetic field strength are from Claussen *et al.* (1997). It is noteworthy the similarity between maser LSR velocities (shown in Tables B.1 - B.4 on the fifth column) and the systemic velocities of the remnants (12 km s^{-1} for W28, 45 km s^{-1} for W44,105 km s^{-1} for 3C391). Also, the magnetic field strengths determined from Zeeman splitting measurements are significant, with values of about 0.2 milliGauss. Besides the OH maser emission, the tables contain also compact radio emission data.

Table B.1: Identified masers within the W28F region

Identifier	Object Type	RA (h m s)	DEC (° ′ ″)	v_{LSR} (km/s)	$B_{\|\|}$ (milliGauss)
W28 OH F	Maser	17 58 49.2	-23 19 00		
W28 40	Maser	17 58 50.08	-23 19 17.0	9.11	
W28 41	Maser	17 58 50.20	-23 19 20.2	10.06	
W28 15	Maser	17 58 48.04	-23 18 40.2	12.29	
W28 20	Maser	17 58 48.47	-23 18 33.9	9.70	
W28 39	Maser	17 58 50.07	-23 19 25.7	11.66	
W28 21	Maser	17 58 48.49	-23 18 32.5	10.29	0.25 ± 0.04
W28 16	Maser	17 58 48.22	-23 18 33.0	12.29	
W28 19	Maser	17 58 48.45	-23 18 30.0	11.23	
W28 37	Maser	17 58 50.04	-23 19 29.8	10.39	
W28 38	Maser	17 58 50.06	-23 19 31.7	-	
W28 14	Maser	17 58 48.00	-23 18 21.6	15.24	
W28 33	Maser	17 58 49.17	-23 18 09.6	9.75	
W28 34	Maser	17 58 49.17	-23 18 08.1	11.40	0.11 ± 0.03
W28 18	Maser	17 58 48.24	-23 18 08.5	13.89	
W28 29	Maser	17 58 48.94	-23 18 06.7	12.74	
W28 17	Maser	17 58 48.23	-23 18 07.9	12.29	
W28 32	Maser	17 58 49.17	-23 18 02.3	10.40	

Table B.2: Identified masers within the W28E region

Identifier	Object Type	RA (h m s)	DEC (° ′ ″)	v_{LSR} (km/s)	$B_{\|\|}$ (milliGauss)
W28 33	Maser	17 58 49.17	-23 18 09.6	9.75	
W28 34	Maser	17 58 49.17	-23 18 08.1	11.40	0.11 ± 0.03
W28 29	Maser	17 58 48.94	-23 18 06.7	12.74	
W28 32	Maser	17 58 49.17	-23 18 02.3	10.40	
W28 30	Maser	17 58 49.05	-23 17 57.8	11.72	0.11 ± 0.03
W28 31	Maser	17 58 49.06	-23 17 57.5	11.97	0.10 ± 0.02
W28 18	Maser	17 58 48.24	-23 18 08.5	13.89	
W28 17	Maser	17 58 48.23	-23 18 07.9	12.29	
W28 26	Maser	17 58 48.68	-23 17 53.6	11.23	
W28 28	Maser	17 58 48.92	-23 17 51.1	10.70	
W28 14	Maser	17 58 48.00	-23 18 21.6	15.24	
W28 27	Maser	17 58 48.71	-23 17 48.5	12.82	0.45 ± 0.25
W28 19	Maser	17 58 48.45	-23 18 30.0	11.23	
W28 23	Maser	17 58 48.64	-23 17 46.5	15.94	0.18 ± 0.08
W28 21	Maser	17 58 48.49	-23 18 32.5	10.29	0.25 ± 0.04
W28 22	Maser	17 58 48.57	-23 17 44.8	15.18	
W28 20	Maser	17 58 48.47	-23 18 33.9	9.70	
W28 24	Maser	17 58 48.65	-23 17 44.4	13.29	0.31 ± 0.03
W28 25	Maser	17 58 48.68	-23 17 44.0	14.41	
W28 16	Maser	17 58 48.22	-23 18 33.0	12.29	0.34 ± 0.08
W28 15	Maser	17 58 48.04	-23 18 40.2	12.29	
W28 OH F	Maser	17 58 49.2	-23 19 00		
W28 35	Maser	17 58 49.38	-23 17 12.2	11.89	
W28 36	Maser	17 58 49.48	-23 17 10.3	11.47	0.09 ± 0.03

Table B.3: Identified masers within the W44E region

Identifier	Object Type	RA (h m s)	DEC (° ′ ″)	v_{LSR} (km/s)	$B_{\|\|}$ (milliGauss)
W44 17	Maser	18 53 56.97	+01 25 44.2	44.47	
W44 OH E	Maser	18 53 57.0	+01 25 45		
W44 15	Maser	18 53 56.70	+01 25 56.7	45.00	
W44 19	Maser	18 53 57.20	+01 25 31.5	45.00	
W44 14	Maser	18 53 56.53	+01 26 00.8	45.53	
W44 13	Maser	18 53 56.39	+01 26 05.0	45.00	
W44 20	Maser	18 53 57.54	+01 25 09.0	44.28	-0.23 ±0.09
W44 21	Maser	18 53 57.55	+01 25 07.9	43.67	
W44 12	Maser	18 53 56.39	+01 26 21.5	45.00	
W44 22	Maser	18 53 57.57	+01 25 06.9	43.94	
W44 11	Maser	18 53 54.60	+01 25 19.2	44.09	-0.28 ± 0.09

Table B.4: Identified masers within the W44F region

Identifier	Object Type	RA (h m s)	DEC (° ′ ″)	v_{LSR} (km/s)	$B_{\|\|}$ (milliGauss)
W44 OH F	Maser	18 54 04.7	+01 22 35		
W44 24	Maser	18 54 04.49	+01 22 37.5	46.91	-0.12 ± 0.03
W44 25	Maser	18 54 04.86	+01 22 31.5	46.06	
W44 23	Maser	18 54 04.44	+01 22 30.2	46.81	-0.30 ± 0.07
W 44B	Radio Source	18 54 04	+01 22.9		

Table B.5: Identified masers and radio sources within the 3C391-1 region.

Identifier	Object Type	RA (h m s)	DEC (° ′ ″)
184647.69-010100.6	Maser	18 46 47.63	-01 01 00.6
NAME 3C 391 BML	Radio Source	18 46 47.1	-01 00 51
RRF 212	Radio Source	18 46 48.2	-01 00 34

Appendix C

Line Frequency Identification

For the identification of the line frequencies, we made use of the on-line version of Jet Propulsion Laboratory's Catalogue, http://spec.jpl.nasa.gov. Table C.1 shows the frequencies of the molecular transitions used in our study.

Table C.1: Identification of line frequencies detected with receivers A and B of JCMT.

Molecule	Transition	Frequency (GHz)
H_2CO	$3_{03} - 2_{02}$	218.22221920
H_2CO	$3_{22} - 2_{21}$	218.4756320
CH_3OH	$J = 5 \rightarrow 4$	241.8065070
^{13}CO	$J = 3 \rightarrow 2$	330.5879601
CS	$J = 7 \rightarrow 6$	342.8830000
^{12}CO	$J = 3 \rightarrow 2$	345.7959899
SiO	$J = 8 \rightarrow 7$	347.3306310
HCN	$J = 4 \rightarrow 3$	354.5054759
HCO^+	$J = 4 \rightarrow 3$	356.7342880
HNC	$J = 4 \rightarrow 3$	362.6303030

Table C.2 contains all the frequencies of interest within the range of K′ filter and the narrow band filter (centered on 2.12 μm), both used in our near infrared observations made with the BEAR instrument on CFHT (Canada-France-Hawaii Telescope).

The most interesting frequency is of shock excited H_2 at 4712.9 cm^{-1}, which was detected in all three supernova remnants. Another frequency of interest is that of Br_γ emission (4616.6 cm^{-1}), which was not detected in our observations, implying a low level of ionization. All the other transitions were either too weak to be detected or concealed by the absorption lines of the Earth atmosphere.

Table C.2: Possible infrared line detections in the K′ band

Molecule	Transition	Frequency (cm^{-1})	Wavelength (μm)
H_2	2 - 1 S(1)	4449.0	2.24769
H_2	1 - 0 S(0)	4497.8	2.22330
He II	10 - 7	4568.1	2.18909
H	7 - 4 (Br_γ)	4616.6	2.16609
H_2	2 - 1 S(2)	4642.0	2.15424
H_2	1 - 0 S(1)	4712.9	2.12183
He I	$4^3S - 3^3P^0$	4733.4	2.11264
H_2	2 -1 S(3)	4822.5	2.07361
He I	$2^1P^0 - 2^1S$	4857.5	2.05867
He II	15 -8	4907.1	2.03786
H_2	1 - 0 S(2)	4917.0	2.03376

Note: He II frequencies are from Garcia and Mack (1965), He I frequencies from Moore (1948), H_2 frequencies from Fink, Wiggins and Rank (1965).